Computational Models in Engineering

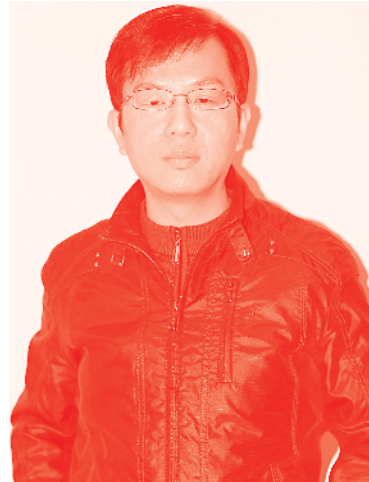*Edited by Konstantin Volkov*

Computational Models in Engineering

Edited by Konstantin Volkov

IntechOpen

Supporting open minds since 2005

Notice
Statements and opinions expressed in the chapters are these of the individual contributors and not necessarily those of the editors or publisher. No responsibility is accepted for the accuracy of information contained in the published chapters. The publisher assumes no responsibility for any damage or injury to persons or property arising out of the use of any materials, instructions, methods or ideas contained in the book.

We are IntechOpen,
the world's leading publisher of
Open Access books
Built by scientists, for scientists

4,700+
Open access books available

120,000+
International authors and editors

135M+
Downloads

151
Countries delivered to

Our authors are among the
Top 1%
most cited scientists

12.2%
Contributors from top 500 universities

Interested in publishing with us?
Contact book.department@intechopen.com

Numbers displayed above are based on latest data collected.
For more information visit www.intechopen.com

Meet the editor

Dr. Volkov is a senior lecturer in thermofluids at the Kingston University (London, UK). He holds a PhD in fluid mechanics. After completion of his PhD, Dr Volkov worked at the Baltic State Technical University (Russia), University of Central Lancashire (UK), and University of Surrey (UK). His areas of expertise cover multidisciplinary areas: from design and optimization of energy systems to fundamental problems focused on modelling and simulation of turbulent multi-phase flows. He is a Chartered Engineer and member of the Institute of Physics, Institution of Mechanical Engineers, Combustion Institute, and Higher Education Academy. He is the author of more than 120 scientific papers and a member of editorial boards and scientific committees of a number of journals and conferences.

Contents

Preface

In many fields, modelling and simulation are integral and therefore essential to business and research. Modelling and simulation provide the capability to enter fields that are either inaccessible to traditional experimentation or where carrying out traditional empirical inquiries is prohibitively expensive. The role of modelling and simulation in engineering and various applications such as computational fluid dynamics, finite element analysis, and others has been underestimated for a long time. However, with a growing complexity of application scenarios as well as numerical algorithms and hardware architectures, the need for sophisticated methods from numerical analysis and computer science has become more important. The growth in computing power has revolutionized the use of realistic mathematical models in science and engineering, and numerical analysis is required to implement these detailed models of the world.

A computer simulation is the execution of a model, represented by a computer program that gives information about the system being investigated. The simulation approach of analyzing a model is opposed to the analytical approach, where the method of analyzing the system is purely theoretical. As this approach is more reliable, the simulation approach gives more flexibility and convenience. Modelling and simulation offer people the chance to develop an understanding of their problem domain by building a simulation of the problem space in which they are interested.

The modelling and simulation identify more key stages in a successful simulation cycle: implementation, exploration and visualization, validation, and embedding.

The book provides and discusses different examples from engineering, as well as where and how numerical methods contribute to more efficient simulation environments. There are 7 chapters in the book, covering different aspects of modelling and simulation in engineering and technology.

In Chapter 1, a three-dimensional simulation technology for physical processes in concentric hydraulic brakes with a throttling-groove partly filled hydraulic cylinder is considered. The technology is based on the numerical solution of a system of Navier-Stokes equations. Free surface tracking is provided by the volume of fluid method. The results of hydraulic brake simulations in the counter-recoil regime are reported and compared to experimental data. The performance of the hydraulic brake is studied as a function of the fluid mass and firing elevation of the gun.

Chapter 2 addresses the behavior of functionally graded solids under dynamic impact loading within the framework of linear elasticity using the parallel explicit algorithm. Numerical examples are presented that verify the dynamic explicit finite element code and demonstrate the dynamic response of graded materials. A three-point bending beam made of epoxy and glass phases under low velocity impact is studied. Finite element modeling and simulation discussed herein can be a critical tool in helping to understand the physics behind the dynamic events.

Chapter 3 discusses the case studies that revealed premature failures of stiffer elements prior to utilising the full capacity of more deformable elements within the same system. From a design perspective, it is important to understand that the dynamic-load capacity of a ground support system depends not only on the capacity of its reinforcement elements but also, and perhaps most importantly, on their compatibility with other elements of the system and on the strength of the connections. The failure of one component of the support system usually leads to the failure of the system.

Chapter 4 estimates criteria for mathematical descriptions in the form of ordinary differential equations. Adequate mathematical descriptions can increase the objectivity of the results of mathematical modeling for future use. These descriptions make it possible and reasonable to use the results of mathematical modeling to optimize and predict the behavior of physical processes. Interrelations between criteria are considered. The proposed criteria are easily transferred to mathematical descriptions in algebraic form.

In Chapter 5, the power flow model of a power system is built using the relevant network, load, and generation data. Outputs of the power flow model include voltages at different buses, line flows in the network, as well as system losses. These outputs are obtained by solving nodal power balance equations. Since these equations are nonlinear, iterative techniques are commonly used to solve this problem. The chapter will provide an overview of different techniques used to solve the power flow problem.

Chapter 6 shows how different approaches can be adopted to model three emerging semiconductor devices namely, silicon-on-insulator four gate transistor, single photon avalanche diode, and insulator-metal transistor device.

In Chapter 7, the results of numerical simulation of heat transfer on a 5-inch hemispherical concave nose at a Mach number of 2 are reported and compared with the available experimental data. Different turbulence models and different discretization schemes are also examined.

The book promotes open discussion between research institutions, academia, and industry from around the globe on research and development of enabling technologies. The book covers many aspects of theory and practice, which deliver essential contributions and provide their input and support to the cooperative efforts.

Dr. Konstantin Volkov
MEng. MSc. PhD. DSc. CEng. MIMechE. MinstP. FHEA.,
Department of Mechanical and Automotive Engineering,
School of Engineering and the Environment,
Faculty of Science, Engineering and Computing,
Kingston University,
London, United Kingdom

Chapter 1

Technology of 3D Simulation of High-Speed Damping Processes in the Hydraulic Brake Device

Valentin Efremov, Andrey Kozelkov, Sergey Dmitriev, Andrey Kurkin, Vadim Kurulin and Dmitry Utkin

Abstract

This chapter describes a three-dimensional simulation technology for physical processes in concentric hydraulic brakes with a throttling-groove partly filled hydraulic cylinder. The technology is based on the numerical solution of a system of Navier–Stokes equations. Free surface tracking is provided by the volume of fluid (VOF) method. Recoiling parts are simulated by means of moving transformable grids. Numerical solution of the equations is based on the finite-volume discretization on an unstructured grid. Our technology enables simulations of the whole working cycle of the hydraulic brake. Results of hydraulic brake simulations in the counter-recoil regime are reported. The results of the simulations are compared with experimental data obtained on JSC "KBP" test benches. The calculated and the experimental sets of data are compared based on the piston velocity as a function of distance. The performance of the hydraulic brake is studied as a function of the fluid mass and firing elevation of the gun.

Keywords: hydraulic brake, Navier-stokes equations, multi-phase flow, volume of fluid, moving rigid body, turbulent flow

1. Introduction

This chapter describes our three-dimensional simulation technology for physical processes in hydraulic brakes with a throttling-groove partly filled hydraulic cylinder. The technology is based on the numerical solution of a system of Navier-Stokes equations with an additional transport equation to track the working fluid/free volume interface by the volume of fluid (VOF) method [1, 2]. As a solver, we use an iterative algorithm, PISO [1, 3], combined with a SLAE solver based on the algebraic multigrid method [4]. To improve the accuracy of solution, we use interface capturing schemes, HRIC [1, 4], near the interface between the phases. Moving parts are simulated by means of moving deforming meshes [5], the motion of which is represented in the initial equations with the Lagrange-Eulerian approximation [6]. Our technology enables modeling of the whole working cycle of the hydraulic brake.

To demonstrate the performance of our technology, we are considering simulation of a hydraulic brake with a throttling-groove partly filled hydraulic cylinder. The simulation outputs are compared with experimental data obtained on the

test benches at JSC "KBP." The calculated and the experimental sets of data are compared based on the piston velocity as a function of displacement. The performance of the hydraulic brake is studied as a function of the fluid mass and hydraulic brake angle.

2. Problem definition

The hydraulic brake serves to absorb the energy of moving parts. Its structure consists of a case with a grooved inner surface, a ring piston mounted directly on the outer surface of the barrel and having holes matching the guide rods with stranded counter-recoil springs uniformly distributed around the barrel in the hydraulic brake chamber, and front and rear packings with circular-cross-section rubber O-rings to seal the hydraulic brake chamber filled with hydraulic fluid (**Figure 1**).

The hydraulic brake starts to react as soon as there is no more free space in the recoil chamber (space between the piston and the rear packing); the fluid is sprinkled through the gaps from the recoil chamber to the counter-recoil chamber (space between the piston and the front packing) at a growing rate and stops the moving parts.

Recoil of the moving parts is countered by the energy stored by the counter-recoil springs while braking. In the counter-recoil phase, the fluid from the counter-recoil chamber is sprinkled through the gaps into the recoil chamber providing the

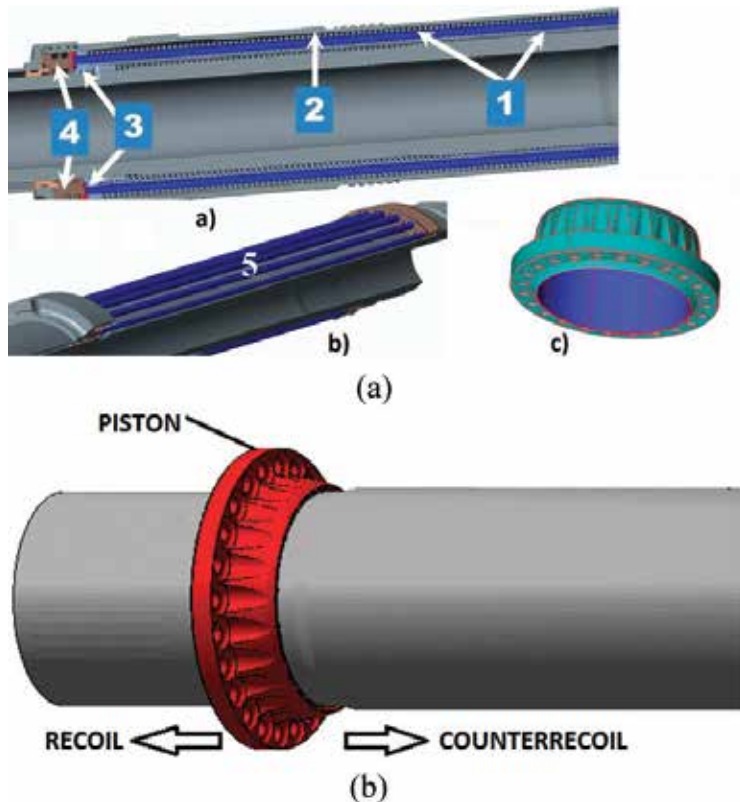**Figure 1.**
(a) General layout of the hydraulic brake: (a) general layout (1—hydraulic fluid cylinder with guides and springs, 2—case, 3—piston, 4—packings); (b) general layout without case (5—guides); and (c) piston; (b) schematic of operation.

required counter-recoil braking law. Both for recoil and for counter recoil, the areas of fluid flow in the hydraulic brake are generated by the gaps between the piston and the grooved case surface defining the law of motion, and between the piston holes and the guide rods.

Numerical simulation of the hydraulic brake includes the following physical processes: turbulent flow of fluid encountering sudden contractions, expansions, and axisymmetric gaps; multi-phase flow with different equations of state (it is reasonable to use constant-density approximation for fluid and perfect gas law for air); and flow with moving solids.

The scope of this work included the development of a mathematical model and numerical method to simulate these physical processes.

3. Mathematical model and numerical scheme

Simulation of hydraulic brake operation involves multi-phase flow simulation with two phases. Each phase can have its individual equation of state. Let us assume that the flow is isothermal within one operation cycle and that the phases have the same field of velocity. These assumptions allow us to construct our numerical model using the VOF method [1, 7]. Considering the assumptions above, let us describe the flow of matter by a system of equations, comprised of the mass and momentum equations and the volume fraction transfer equation:

$$
\begin{cases}
\dfrac{\partial \rho}{\partial t} + \dfrac{\partial}{\partial x_i}(\rho u_i) = 0, \\[2ex]
\dfrac{\partial \rho u_i}{\partial t} + \dfrac{\partial}{\partial x_i}\left(\rho u_i u_j\right) = -\dfrac{\partial p}{\partial x_i} + \dfrac{\partial}{\partial x_i}\tau_{ij} + \rho g_i, \\[2ex]
\dfrac{\partial \rho_\xi \alpha_\xi}{\partial t} + \dfrac{\partial}{\partial x_i}\left(u_i \rho_\xi \alpha_\xi\right) = 0,
\end{cases}
\tag{1}
$$

where t is the time, $u_i = \{u_1, u_2, u_3\} = \{u, v, w\}$ is the velocity, x_i is the spatial vector component, τ_{ij} is the viscous stress tensor, g_i is the gravity acceleration vector, ξ is the phase index, α_ξ is the volume fraction of the ξ-th phase, and ρ is the resulting density defined as an average over all the phases:

$$
\rho = \sum_{\xi=1}^{N} \rho_\xi \alpha_\xi
\tag{2}
$$

where N is the number of phases.

The volume fraction transfer equation is written in terms of the transfer of the quantity α_ξ:

$$
\frac{\partial \alpha_\xi}{\partial t} + \frac{\partial}{\partial x_i}\left(u_i \alpha_\xi\right) = -\frac{\alpha_\xi}{\rho_\xi}\left(\frac{\partial \rho_\xi}{\partial t} + u_i \frac{\partial \rho_\xi}{\partial x_i}\right)
\tag{3}
$$

Summing Eq. (3) over all the phases and considering the equality $\sum_\xi \alpha_\xi = 1$, we obtain the following mass equation with respect to the velocity divergence:

$$
\frac{\partial u_i}{\partial x_i} = -\sum_\xi \frac{\alpha_\xi}{\rho_\xi}\left(\frac{\partial \rho_\xi}{\partial t} + u_i \frac{\partial \rho_\xi}{\partial x_i}\right) = -\sum_\xi \frac{\alpha_\xi}{\rho_\xi}\frac{d\rho_\xi}{dt}
\tag{4}
$$

The momentum equation is written in a half-divergent form. This stabilizes the iterative procedure of numerical solution of this equation [3, 4]:

$$\rho \frac{\partial u_i}{\partial t} + \frac{\partial}{\partial x_j}\left(\rho u_i u_j\right) - u_i \frac{\partial}{\partial x_j}\left(\rho u_j\right) = -\frac{\partial p}{\partial x_i} + \frac{\partial \tau_{ij}}{\partial x_j} + \rho g_i \qquad (5)$$

An important feature of this problem is that we need to consider the motion of moving parts, which travel to a distance exceeding the half length of the hydraulic brake during computation. To incorporate their motion, we decided to use a topology-preserving mesh deformation method. To prevent unnecessary cell deformations, the mesh nodes located at fixed elements (case and guide rods) follow the moving piston preserving their geometry. The mesh deformation was implemented by the IDW method [5].

To allow for the mesh motion in Eq. (1), we have rewritten the equations of volume fraction transfer and momentum of the phases in a moving frame of coordinate in accordance with the known law [6]:

$$\frac{d^* \varphi}{dt} = \frac{\partial \varphi}{\partial t} + v_i \frac{\partial \varphi}{\partial x_i} \qquad (6)$$

where $\frac{d^* \varphi}{dt}$ is the substantial derivative φ with respect to the moving frame of reference and v_i is the mesh displacement velocity vector. Using Eq. (3), the volume fraction transfer equation can be written as:

$$\frac{d^* \alpha_\xi}{dt} + \left(u_i - v_i\right)\frac{\partial \alpha_\xi}{\partial x_i} + \alpha_\xi \frac{\partial u_i}{\partial x_i} = -\frac{\alpha_\xi}{\rho_\xi}\left[\frac{d^* \rho_\xi}{dt} + \left(u_i - v_i\right)\frac{\partial \rho_\xi}{\partial x_i}\right] \qquad (7)$$

Here $\frac{d^* \alpha_\xi}{dt}$ denotes the substantial derivative on the moving mesh. The momentum equation is also defined with respect to the moving frame of reference considering Eq. (3):

$$\rho \frac{d^* u_i}{dt} + \frac{\partial}{\partial x_j}\left(\rho u_i \left(u_j - v_j\right)\right) - u_i \frac{\partial}{\partial x_j}\left(\rho\left(u_j - v_j\right)\right) = -\frac{\partial p}{\partial x_i} + \frac{\partial \tau_{ij}}{\partial x_j} + \rho g_i \qquad (8)$$

The mass equation is defined with respect to the velocity in the moving frame of reference:

$$\frac{\partial(u_i - v_i)}{\partial x_i} = -\sum_\xi \frac{\alpha_\xi}{\rho_\xi}\left[\frac{d^* \rho_\xi}{dt} + \left(u_i - v_i\right)\frac{\partial \rho_\xi}{\partial x_i}\right] \qquad (9)$$

This form of the equations is easy to implement within the framework of finite-volume discretization [8–11]. The chosen way of taking into account the mesh motion is optimal, because it does not require topology reconstruction, though conservative with respect to the major quantities.

The experimental data on the hydraulic brake operation make it possible to estimate the Reynolds number, which equals Re = 10^5–10^6 in the cylindrical gap during recoil of the moving parts. The most reasonable way to include turbulent flow components with such a Reynolds number is to use the RANS approach based on the solution of the Reynolds-averaged system Eq. (2) [8, 9]. The averaged system of equations is closed using the SST turbulence model, which has proven its efficiency in real-life problem simulations [11–13]. In the SST model, the (k-ε) model is formulated in terms of (k-ω) and is focused on resolving small-scale turbulence in the outer flow region. A (k-ω) model intended to describe large-scale turbulence is used in the boundary layer. The combination of these models together is carried out with the help of a function that ensures the proximity of the total model to the (k-ε) model far from the solid walls and to the (k-ω) model in the near-wall flow area.

The resulting system of equations is solved by numerical integration on the finite-volume mesh. The relationship of pressure and velocity while solving Eq. (1) is determined by the SIMPLE algorithm [2]. The SIMPLE algorithm allows to find the pressure field for closure of the continuity equation. Let us write the equation of conservation of momentum at time discretization according to the Euler scheme:

$$\rho \frac{u_i^{n+1} - u_i^j}{\Delta t} + \rho \frac{\partial}{\partial x_j}\left(u_i^{n+1}u_j^n\right) = -\frac{\partial p^{n+1}}{\partial x_i} + \frac{\partial}{\partial x_j}\left(\tau_{ij}^{n+1}\right) \qquad (10)$$

where n is the solution from the previous iteration, and j is the solution from the previous time step. To solve this equation, the pressure and velocity are supposed to have the form:

$$\begin{cases} u_i^{n+1} = u_i^n + u_i^*, \\ p^{n+1} = p^n + \alpha_p(p^{n+1} - p^n) = p^n + \alpha_p \delta p^{n+1}. \end{cases} \qquad (11)$$

Here $0 \leq \alpha_p \leq 1$ is the parameter of relaxation.

Substitution of the first expression in Eq. (11) into Eq. (10) yields a preliminary estimate of the velocity value in the next step from the equation:

$$\rho \frac{u_i^*}{\Delta t} + \rho \frac{\partial}{\partial x_j}\left(u_i^* u_j^n\right) - \frac{\partial}{\partial x_j}\left(\tau_{ij}^*\right) = \rho \frac{u_i^j}{\Delta t} - \frac{\partial p^n}{\partial x_i} \qquad (12)$$

The molecular and turbulent components of the tensor of tangential stress in Eq. (12) are also calculated using u_i^*. In the second stage, the full speed value at the $(n+1)$th iteration is calculated by adjustment using the correction to pressure:

$$u_i^{n+1} = u_i^* - \Delta t \frac{\partial(\delta p^{n+1})}{\partial x_i} \qquad (13)$$

The pressure correction is found from Eq. (13) using the continuity condition for u_i^{n+1}. Taking the derivative of both sides of Eq. (13), we obtain the Poisson equation for pressure:

$$\frac{\partial}{\partial x_i}\left(\frac{\partial(\delta p^{n+1})}{\partial x_i}\right) = \frac{1}{\Delta t}\frac{\partial u_i^*}{\partial x_i} \qquad (14)$$

This iterative procedure allows to obtain fields of velocity and pressure satisfying the system of Eq. (1).

Discretization of the equations is performed by a finite-volume technology. Let us show it on the example of the equation of transfer of a scalar quantity φ:

$$\frac{\partial \rho \varphi}{\partial t} + \frac{\partial}{\partial x_j}\left(\rho \varphi u_j\right) = \frac{\partial}{\partial x_j}\tau_j + Q, \ \tau_j = \mu \frac{\partial \varphi}{\partial x_j} \qquad (15)$$

The time discretization of Eq. (15) can be carried out using one of the known schemes, for example, the Euler scheme, which is used in the work to solve non-stationary problems using the RANS approach:

$$\frac{\rho^{j+1}\varphi^{j+1} - \rho^j\varphi^j}{\Delta t} + \left[\frac{\partial}{\partial x_j}\left(\rho \varphi u_j\right) - \frac{\partial}{\partial x_j}\tau_j - Q\right]^{j+1} = 0 \qquad (16)$$

Here j is the number of the time step.

Let us integrate Eq. (16) over volume and proceed to integration over the area for the convective and diffusion terms:

$$\int\limits_{V_P} \frac{\rho^{j+1}\varphi^{j+1} - \rho^j\varphi^j}{\Delta t} dV + \oint\limits_{S_P} \rho\varphi u_j dS_j - \oint\limits_{S_P} \mu \frac{\partial\varphi}{\partial x_j} dS_j - \int\limits_{V_P} Q dV = 0 \qquad (17)$$

For approximation on a finite-volume grid, the convective term can be written in the form:

$$\oint\limits_{S_P} \rho\varphi u_j dS_j \approx \sum_k \rho_k \varphi_k u_{j,k} S_{j,k} \approx \sum_k \rho_k \varphi_k F_k \qquad (18)$$

where F_k is the volume flow through the face k. The value of φ_k on the face k is determined by the applied convective scheme.

The discrete analog of the diffusion term can be written in the following form:

$$\oint\limits_{S_P} \mu \frac{\partial\varphi}{\partial x_j} dS_j \approx \sum_k \left(\mu \frac{\partial\varphi}{\partial x_j} \right)_k S_{j,k} = \sum_k \mu_k \left(\frac{\partial\varphi}{\partial n_k} \right)_k |S_k| \qquad (19)$$

where n_k is the normal to face k.

The value of $\left(\frac{\partial\varphi}{\partial x_i} \right)_k$ on the face k is found by linear interpolation on the values of the gradient in the cells, which are determined by one of the known methods, for example, the Gauss method:

$$\left(\frac{\partial\varphi}{\partial x_i} \right)_P = \frac{1}{V_P} \sum_k \varphi_k S_{k,i} \qquad (20)$$

Using this discretization, Eq. (15) is replaced by a system of linear algebraic equations written for each calculation cell:

$$A_P \varphi_P + \sum_{k_{\text{int}}} A_{k_{\text{int}}} \varphi_{M_{k_{\text{int}}}} = R_{i,P} \qquad (21)$$

Time discretization of the equations is performed by a three-layer second-order scheme [10]. Discretization of the convective terms in the equation of motion, equation of transfer of turbulent parameters, is performed by the upwind scheme LUD [10], and in the volume fraction transfer equation, by the HRIC scheme [1], which prevents excessive numerical diffusion of the phase interface. The force of gravity was included using a bulk force fitting algorithm [14].

These methods and models have been implemented in the software package LOGOS. LOGOS is a 3D multi-physics code for convective heat and mass transfer, aerodynamic and hydrodynamic simulations on parallel computers [11, 13–18]. LOGOS has been successfully verified and demonstrated with sufficiently high efficiency on a number of various hydrodynamic tests, including propagation of gravity waves on a free surface (tsunami) [2, 14, 18] and industry-specific simulations [11, 15]. Speedup of computations on highly parallel computers is provided by an original implementation of the algebraic multigrid method [11, 19].

4. Numerical simulation of hydraulic brake operation

Let us consider the counter-recoil phase in the operation of the hydraulic brake, when the moving parts together with the piston (see **Figure 1b**) are driven by the

springs from their rightmost position to the leftmost one resisting the hydrodynamic force acting on the fluid side.

To solve the problem numerically, an unstructured hexahedral-dominant mesh was constructed using the pre- and post-processing tools of the LOGOS. The mesh is refined near the piston and in the gaps between the piston and the case, where the flow of fluid is particularly strong. **Figure 2** shows mesh fragments.

When constructing the mesh, we placed the piston in the middle between its rightmost initial and leftmost end positions of counter recoil. This minimizes mesh deformation during computation. The problem was simulated in the unsteady setup; the time step was $5 \times 10^{-4} t_0$, where t_0 is the total time of piston counter-recoil motion. The forces acting on the piston, its velocity and displacement were calculated at the end of each time step after finding the solution of the Navier–Stokes equation.

During computation, the piston together with the moving parts is accelerated by the springs and reaches its maximum velocity during the second half of its travel. The piston then enters the grooved region of the case with a decreasing gap, as a result of which the hydrodynamic resistance grows and slows down the moving parts. The computation ends when the piston is at d_m = 0.01 m from its end position, which is attributed to the maximum admissible mesh deformation in the counter-recoil chamber.

When the piston is moving, in addition to the force exerted by the springs and hydrodynamic resistance, the moving parts are exposed to friction arising in the packings, between the guides and the piston, and inside the stranded springs during their compression or tension. The resultant of the forces exerted by the springs and friction can be expanded into two components. The first does not depend on the velocity of the moving parts and can be easily measured experimentally by pulling the moving parts at a slow rate. The second depends on the velocity of the moving parts and is mostly related to friction in the turns of the stranded springs. Empirical estimates show that the second component of the resultant force can be expressed empirically as

$$F_{mp}^{din} = \eta u M \qquad (22)$$

where u is the velocity, M is the mass of the moving parts, η is an empirical coefficient, which can vary in the range of η = 0–5 s^{-1} for the springs we use.

Computations were conducted with η = 0, 3, 4, and 5. **Figure 3** shows the field of volume fraction of the fluid at different times for η = 0 s^{-1}.

At t = 0.2 t_0, where t_0 is the total time of counter recoil, a wave of fluid rises upstream of the piston. Pressure in the counter-recoil chamber grows. Air is actively bled over through the upper part of the gap. A flow of fluid emerges in the bottom part of the gap. Its rate is 10–15 times slower than the rate of the air flow (**Figure 4**).
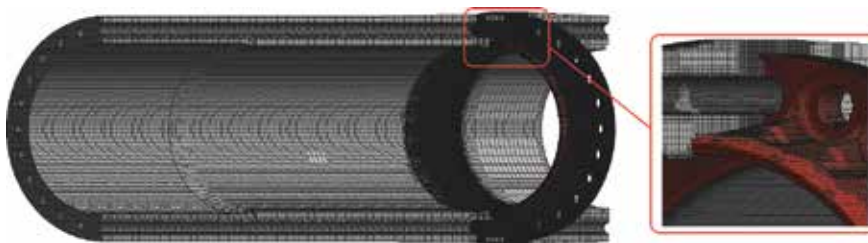
Figure 2.
Mesh fragments.
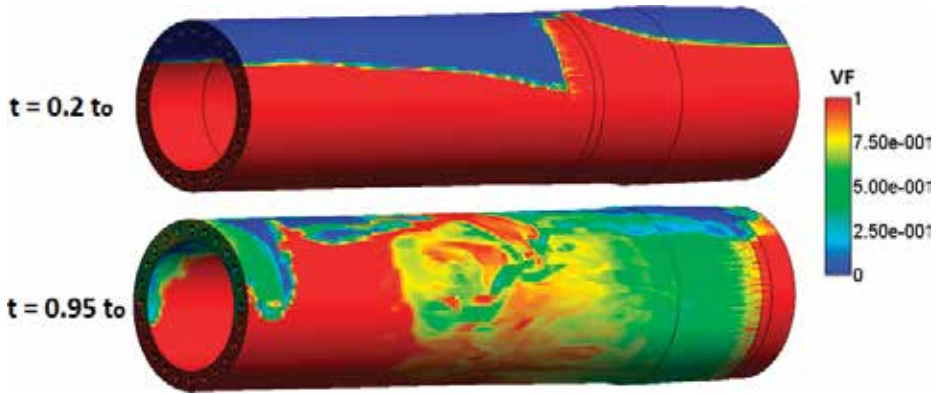
Figure 3.
Field of volume fraction of the fluid at different times.
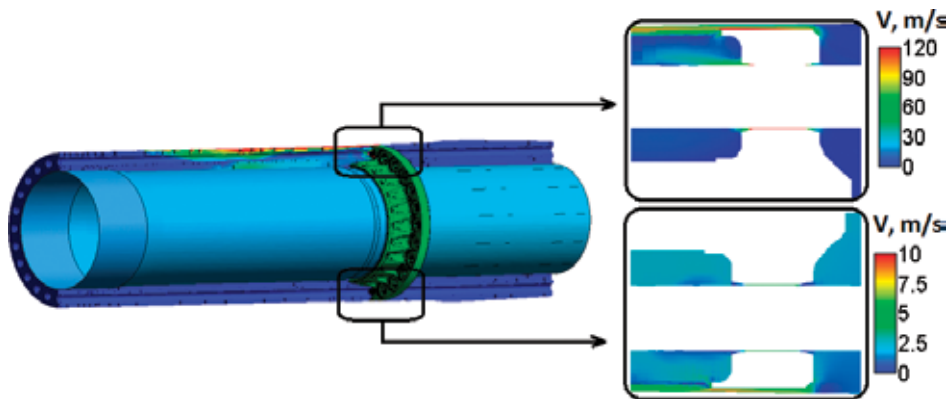
Figure 4.
Field of velocity amplitude (t = 0.2 t_o).

As the piston continues to move, the fluid is sprinkled through the gaps at a growing rate. At $t = 0.95\, t_0$, most of the fluid is already pressed out of the counter-recoil chamber; it forms a nearly homogeneous gas–liquid mixture in the opposite chamber. Pressure in the counter-recoil chamber reaches $P = 150\, P_0$, where $P_0 = 1$ atm is the initial pressure.

Fluid velocity in the gap grows as high as $V = 50$–70 m/s (**Figure 5**). After the fluid has flown over through the gap, the bulk gas content in the mixture increases steeply as a result of a pressure drop. This leads to a further growth of mixture velocity to $V = 90$ m/s (**Figure 5**). This effect is less pronounced in the bottom part of the gap because of the lower gas content in the mixture sprinkled through the gap.

Figure 6 shows a plot of piston velocity as a function of displacement for different values of η.

On the whole, our results match the experimental data both qualitatively and quantitatively. All the simulated cases consistently predict the state of piston acceleration. In the high-velocity phase of piston motion, the parameter η starts to play a significant role. The best agreement with experiment is provided by $\eta = 3$ s^{-1}. This does not mean that the value above is close to the actual one, but is indicative of the fact that our numerical model, input data, and mesh are capable of describing the process of piston motion with required accuracy, if we use this value of η in our computational model.
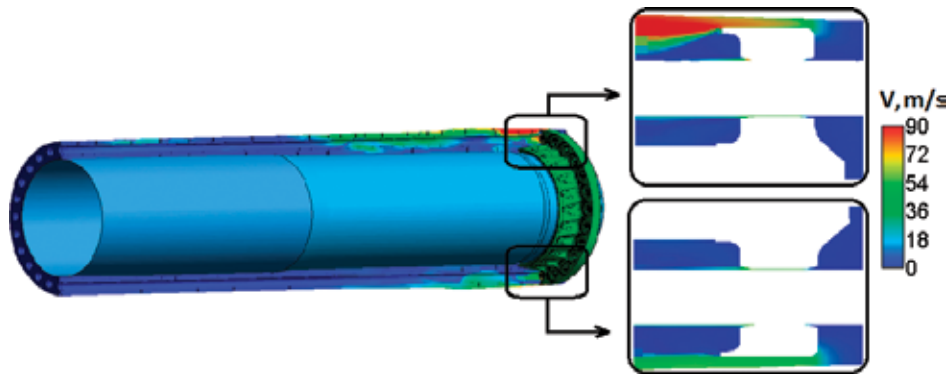
Figure 5.
Field of velocity amplitude (t = 0.95 t_o).
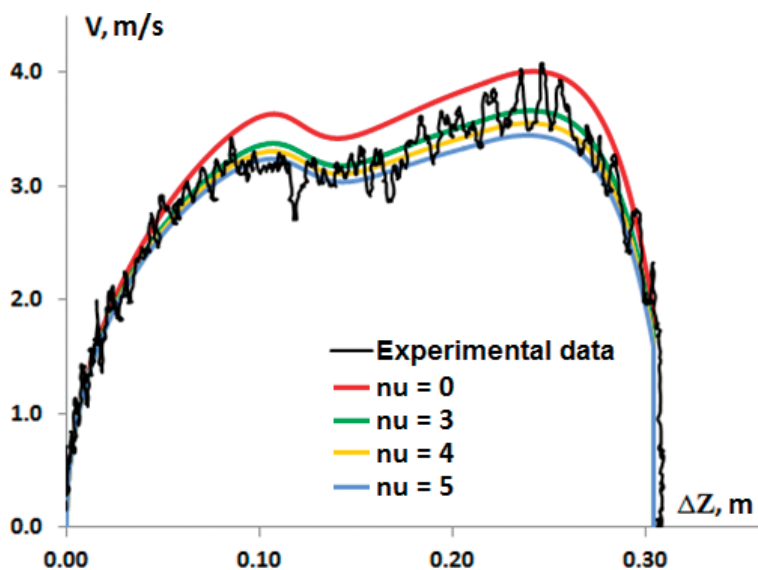
Figure 6.
Piston velocity as a function of displacement.

The counter-recoil phase occurs at zero angle (the hydraulic brake is placed horizontally). Let us consider the dependence of piston motion on the accuracy of horizontal positioning of the hydraulic brake. For this purpose, let us carry out calculations with angles α = 1° and α = −1°. The calculation results are shown in **Figure 7**.

The plots demonstrate that the piston velocity grows with increasing angle. This is quite predictable, because the amount of fluid in the counter-recoil chamber decreases as the angle increases. One should also note that the gravity force acting on the moving parts in the direction opposite to that of their motion at α > 0 or in the direction of their motion at α < 0 has no measurable effect on the result.

The angle of the hydraulic brake also controls the static pressure in the counter-recoil chamber (**Figure 8**). The first pressure maximum is attributed to a decrease in the volume fraction of air in the counter-recoil chamber as the piston moves, and the subsequent drop, to a growth in the gap size between the piston and the grooved case region. As the angle increases, the initial amount of fluid in the counter-recoil chamber decreases, and the maximum shifts toward the range of greater piston
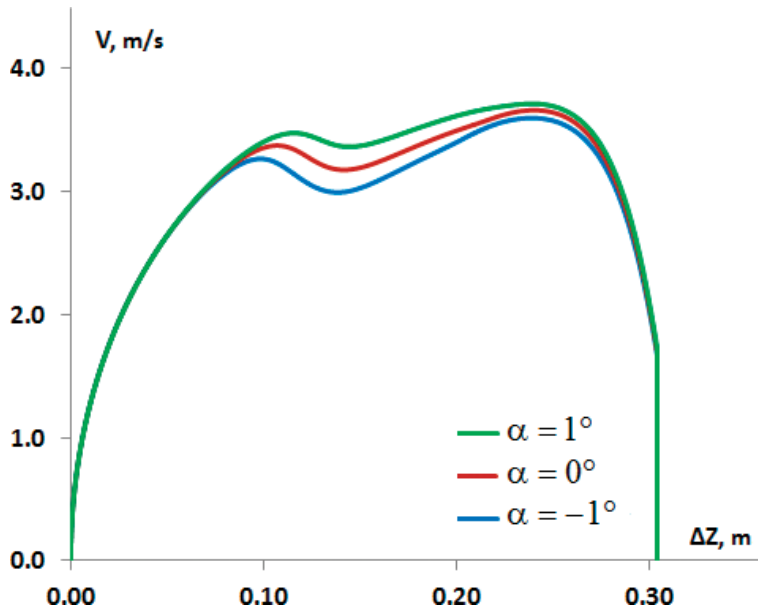
Figure 7.
Piston velocity as a function of piston displacement for different angles.
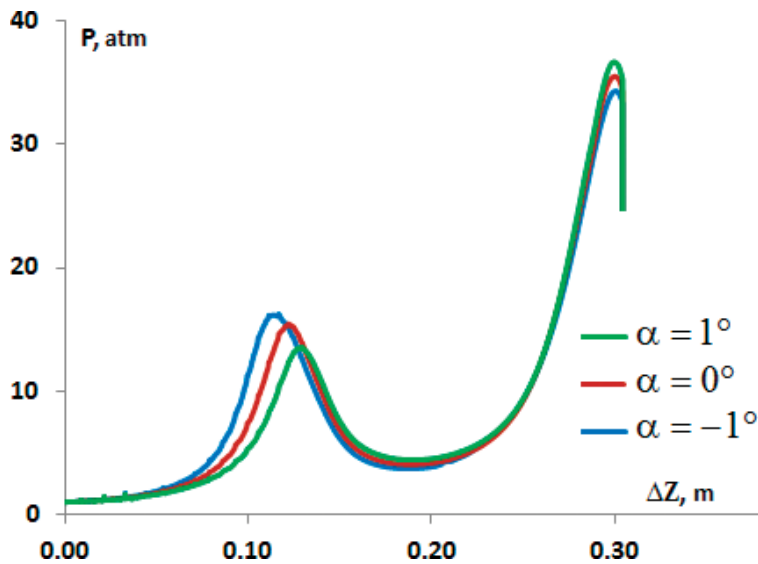
Figure 8.
Static pressure in the counter-recoil chamber as a function of piston displacement.

displacements, which allows the piston to speed up to a higher velocity. This increase in the piston velocity leads to a higher pressure maximum in the region of strong slowdown (the second pressure maximum in **Figure 6**). Thus, an increase in the amount of fluid in the counter-recoil chamber leads to a higher and earlier first pressure maximum and a lower second pressure maximum, which is quite consistent with process physics.

The results of piston motion analysis as a function of initial fluid level in the hydraulic brake ($h = h_0$, $h = h_0 + 0.01$ m, $h = h_0 - 0.01$ m) are shown in **Figure 9**.

The fluid level has a considerable effect on the piston velocity. A 1-cm increase in the level results in a 10% drop in the average piston velocity, which is explained

by a decrease in the force of hydrodynamic resistance acting on the moving parts. Note that the slopes of the velocity plot are indicative of the same trend: as the fluid level in the counter-recoil chamber rises, the first pressure maximum increases and the second one decreases.

An important characteristic of the counter-recoil piston motion is piston velocity V_{extr} at 159 mm to the counter-recoil end (ΔZ = 153 mm), where the shell extractor is located, the performance of which depends on the velocity of the moving parts. Another important characteristic is piston velocity close to the end position V_{end}, which will govern the force exerted by the piston on the packing in the counter-recoil chamber. The values of these characteristics are presented in **Table 1**.

The table demonstrates that a change in the fluid level within 1 cm leads to a 15% change in the velocity V_{extr}. A change in the angle to 1 degree results in a 5% change in the velocity. Note that the level and angle variations have a minor effect on the velocity V_{end}, the oscillations of which do not exceed 2–3%.

The results demonstrate that the governing quantity, which controls the performance of the hydraulic brake, is the initial fluid level in the counter-recoil chamber. An increase in the fluid level results in a lower average piston velocity, smaller V_{extr} and V_{end}, shift and rise in the first pressure maximum, and drop in the second pressure maximum. The process pattern, however, does not depend on the reason
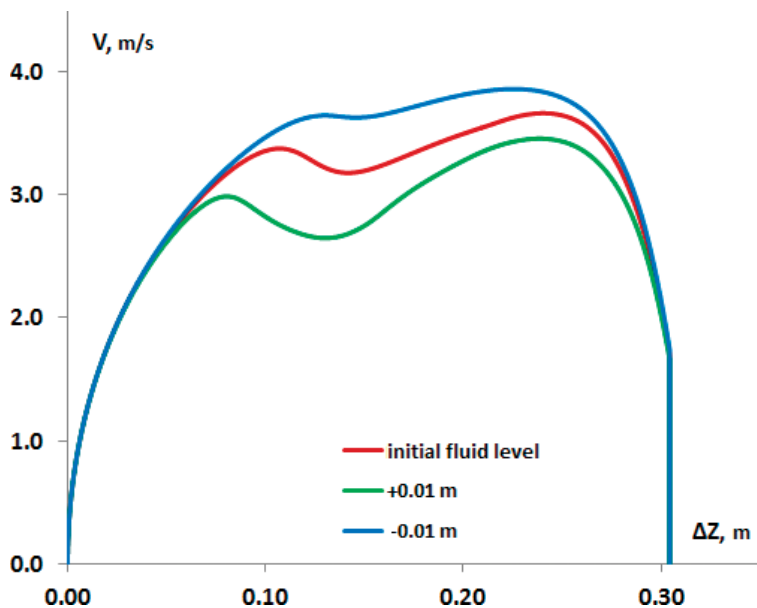
Figure 9.
Piston velocity as a function of displacement for different fluid levels.

No.	α [degree]	$h - h_0$ [sm]	V_{extr} [m/s]	V_{end} [m/s]
1	0.0	−1.0	3.64	1.74
2	0.0	0.0	3.21	1.69
3	0.0	1.0	2.78	1.65
4	−1.0	0.0	3.05	1.66
5	1.0	0.0	3.38	1.72

Table 1.
Piston motion characteristics.

of the rise in the fluid level in the counter-recoil chamber: both general increase in the initial amount of fluid and negative angle of the hydraulic brake result in the same trends.

5. Conclusion

In this chapter, we have presented a three-dimensional numerical modeling technology for physical processes occurring in hydraulic brake devices. The technology is based on the numerical solution of a system of Reynolds-averaged Navier–Stokes equations. To track the free surface, we use the volume of fluid (VOF) method. Moving parts are simulated by means of moving deforming meshes. Numerical solution of the equations is based on the finite-volume discretization, which is used to model the counter-recoil phase in hydraulic brake operation. This technology enables simulations on three-dimensional unstructured meshes. The technology is implemented based on the program package LOGOS, which provides high parallel efficiency of simulations.

The technology has been used to model the counter-recoil phase in hydraulic brake operation. Results of studying the effect of the parameter related to friction, hydraulic brake angle, and initial fluid level are reported. Our numerical experiments have demonstrated that the initial fluid level in the counter-recoil chamber is the governing quantity in hydraulic brake operation. An increase in the fluid level in the counter-recoil chamber as a result of pouring more fluid or placing the hydraulic brake at a negative angle results in the same trend in the change in pressure and its maximums.

Conflict of interest

The authors declare that they have no conflict of interest.

Author details

Valentin Efremov[1], Andrey Kozelkov[2], Sergey Dmitriev[3], Andrey Kurkin[3*],
Vadim Kurulin[2] and Dmitry Utkin[2]

1 Joint-Stock Company "Instrument Design Bureau named after Academician A.G.
Shipunov", Tula, Russia

2 Russian Federal Nuclear Center—All-Russian Research Institute of Experimental
Physics, Sarov, Russia

3 Nizhny Novgorod State Technical University n.a. R.E. Alekseev,
Nizhny Novgorod, Russia

*Address all correspondence to: aakurkin@gmail.com

IntechOpen

References

[1] Ubbink O. Numerical prediction of two fluid systems with sharp interfaces [thesis]. London: Imperial College of Science, University of London; 1997

[2] Kozelkov AS, Kurkin AA, Pelinovsky EN, Tyatyushkina ES, Kurulin VV, Tarasova NV. Landslide-type tsunami modelling based on the Navier-stokes equations. Science of Tsunami Hazards. 2016;**35**:106-144

[3] Yatsevich SV, Kurulin VV, Rubtsova DP. On the Application of the PISO Algorithm to Molecular-Immiscible Fluid Dynamics Problems. VANT, Ser. Matematicheskoe Modelirovanie Fizicheskikh Protsessov. Vol. 1. 2015. pp. 16-29

[4] Khrabry AI, Smirnov EM, Zaytsev DK. Solving the convective transport equation with several high-resolution finite volume schemes. Test computations. In: Proceedings of the 6th International Conference on Computational Fluid Dynamics (ICCFD-6); 12–16 July 2010; Russia. Berlin, Heidelberg: Springer-Verlag; 2011. pp. 535-540

[5] Luke E, Collins E, Blades E. A fast mesh deformation method using explicit interpolation. Journal of Computational Physics. 2012;**231**:586-601. DOI: 10.1016/j.jcp.2011.09.021

[6] Loitsyansky LG. Liquid and Gas Mechanics. Vol. 840. Moscow: Nauka; 1987

[7] Rusche H. Computational fluid dynamics of dispersed two-phase flows at high phase fractions [thesis]. London: Imperial College of Science, University of London; 2002

[8] CAJ F. Computational techniques for fluid dynamics. In: Fundamental and General Techniques. 2nd ed. Vol. 1. Berlin, Heidelberg, New York: Springer-Verlag; 1991. p. 401

[9] Fletcher CAJ. Computational techniques for fluid dynamics. In: Specific Techniques for Different Flow Categories. Vol. 2. Berlin, Heidelberg, New York: Springer-Verlag; 1998. p. 496

[10] Jasak H. Error analysis and estimation for the finite volume method with applications to fluid flows [thesis]. London: Imperial College of Science, University of London; 1996

[11] Kozelkov AS, Kurulin VV, Lashkin SV, Shagaliev RM, Yalozo AV. Investigation of supercomputer capabilities for the scalable numerical simulation of computational fluid dynamics problems in industrial applications. Computational Mathematics and Mathematical Physics. 2016;**56**:1506-1516. DOI: 10.1134/S0965542516080091

[12] Menter FR, Kuntz M, Langtry R. Ten years of experience with the SST turbulent model. In: Hanjalic K, Nagano Y, Tummers M, editors. Turbulence, Heat and Mass Transfer 4. Danbury: Begell House Inc; 2003. pp. 625-632

[13] Kozelkov A, Kurulin V, Emelyanov V, Tyatyushkina E, Volkov K. Comparison of convective flux discretization schemes in detached-eddy simulation of turbulent flows on unstructured meshes. Journal of Scientific Computing. 2016;**67**:176-191. DOI: 10.1007/s10915-015-0075-7

[14] Efremov VR, Kozelkov AS, Kornev AV, Kurkin AA, Kurulin VV, Strelets DY, et al. Method for taking into account gravity in free-surface flow simulation. Computational Mathematics and Mathematical Physics. 2017;**57**:1720-1733. DOI: 10.1134/S0965542517100086

[15] Deryugin YN, Zhuchkov RN, Zelenskiy DK, Kozelkov AS, Sarazov AV, Kudimov NF, et al. Validation results for the LOGOS multifunction software package in solving problems of aerodynamics and gas dynamics for the lift-off and injection of launch vehicles. Mathematical Models and Computer Simulations. 2015;**7**:144-153. DOI: 10.1134/S2070048215020052

[16] Kozelkov AS, Kurkin AA, Legchanov MA, Kurulin VV, Tyatyushkina ES, Tsibereva YA. Investigation of the application of RANS turbulence models to the calculation of nonisotermal low-Prandtl-number flows. Fluid Dynamics. 2015;**50**:501-513. DOI: 10.1134/S0015462815040055

[17] Kozelkov AS, Kurkin AA, Kurulin VV, Lashkin SV, Tarasova NV, Tyatyushkina ES. Numerical modeling of the free rise of an air bubble. Fluid Dynamics. 2016;**51**:709-721. DOI: 10.1134/S0015462816060016

[18] Kozelkov AS, Kurkin AA, Pelinovsky EN, Kurulin VV, Tyatyushkina ES. Numerical modeling of the 2013 meteorite entry in Lake Chebarkul, Russia. Natural Hazards and Earth System Sciences. 2017;**17**:671-683. DOI: 10.5194/nhess-17-671-2017

[19] Volkov KN, Kozelkov AS, Lashkin SV, Tarasova NV, Yalozo AV. A parallel implementation of the algebraic multigrid method for solving problems in dynamics of viscous incompressible fluid. Computational Mathematics and Mathematical Physics. 2017;**57**: 2030-2046. DOI: 10.1134/ S0965542517120119

Chapter 2

Three-Dimensional Finite Element Analysis for Nonhomogeneous Materials Using Parallel Explicit Algorithm

Ganesh Anandakumar and Jeongho Kim

Abstract

This chapter addresses the behavior of functionally graded solids under dynamic impact loading within the framework of linear elasticity using parallel explicit algorithm. Numerical examples are presented that verify the dynamic explicit finite element code and demonstrate the dynamic response of graded materials. A three-point bending beam made of epoxy and glass phases under low-velocity impact is studied. Bending stress history for beam with higher values of material properties at the loading edge is consistently higher than that of the homogeneous beam and the beam with lower values of material properties at the loading edge. Larger bending stresses for the former beam may indicate earlier crack initiation times, which were proven by experiments performed by other researchers. Wave propagation in a 3D bar is also investigated. Poisson's ratio and thickness effects are observed in the dynamic behavior of the bar. Finite element modeling and simulation discussed herein can be a critical tool to help understand physics behind the dynamic events.

Keywords: parallel algorithm, nonhomogeneous materials, dynamic response, wave propagation

1. Introduction

Functionally graded materials (FGMs) are materials characterized by smooth variation in composition, microstructure, and properties. These materials have emerged with the need to enhance material performance and to meet specific functions and applications [1, 2]. The material gradation concept has been utilized in various applications [3–16]. The concept of FGMs has been applied to thermal barrier structures and wear- and corrosion-resistant coatings and also used for joining dissimilar materials [17]. FGMs are subjected to harsh thermal/mechanical/dynamic environments. Thin-walled plates and shells, which are used in reactor vessels, turbines, and other machine parts, are susceptible to buckling failure, large deflections, or excessive stresses induced by thermomechanical loading. Functionally graded coatings on these structural elements may help reduce these failures [18].

The dynamic response of FGMs has been investigated [19]. Reddy and Chin [20] carried out nonlinear transient thermoelastic analysis of FGMs by using plate elements for moderately large rotations. Gong et al. [21] studied the elastic response of

FGM shells subjected to low-velocity impact. Rousseau and Tippur [22–24] studied the dynamic fracture of a three-point bending beam made of epoxy/glass phases under low-velocity impact. Cheng et al. [25] used a peridynamic model to investigate dynamic fracture of FGMs. Lindholm and Doshi [26] looked into a slender bar with free ends and obtained a solution that is synthesized from eigenfunctions by using the principle of virtual work. Karlsson et al. [27] developed a Green's function approach for 1D transient wave propagation in composite materials. Santare et al. [28] used graded finite elements to simulate elastic wave propagation in graded materials. Chakraborty and Gopalakrishnan [18] developed a spectral element to study wave propagation behavior in FGM beams subjected to high-frequency impact loads.

The development of parallel computers and improvements in computer hardware has been of significant importance [29]. A dynamic event has a key characteristic that the incident pulse duration is very small in the order of microseconds that makes the frequency content of pulse very high (in the order of kHz). Thus, all the higher-order modes participate in the dynamic response, and the finite element mesh must be very fine enough to capture the small wavelengths [18]. This makes the system size enormously large. But in an explicit analysis, storage of large matrices is avoided with the added advantage of not requiring to solve linear algebraic equations [29]. Explicit methods are also conditionally stable, and so the time step size must be below a critical value that is dependent on the size of the smallest finite element [30]. Due to mesh size constraint, extremely small time steps (0.01–100 μs) are needed to solve explicit problems. This can be overcome by parallel computing. Krysl and Belytschko [30] investigated to parallelize an existing object-oriented code written in C where a Parallel Virtual Machine (PVM) was used for the necessary communication. Krysl and Bittnar [31] and Rao [32, 33] adopted the Message Passing Interface (MPI) standard for the implementation of the exchange algorithm, which is used in this chapter.

This chapter addresses the behavior of functionally graded materials under dynamic impact loading within the framework of linear elasticity using MPI-based parallel explicit algorithm. Numerical examples are presented that verify the dynamic explicit finite element code and demonstrate the dynamic response of graded materials. Finite element modeling and simulation can be a critical tool to help understand physics behind the dynamic events.

2. Finite element formulation for dynamic analysis

The governing equation for structural dynamics is given by [34]

$$\int_{\Omega} (\sigma : \delta E + \rho \ddot{u} \bullet \delta u) d\Omega - \int_{\Gamma_{ext}} T_{ext} \bullet \delta u \ d\Gamma = 0 \tag{1}$$

where Ω is domain volume, Γ is the boundary with a normal vector n, u is the displacement vector, T is the traction vector, σ is the Cauchy stress tensor, ü is the acceleration vector, ρ is the mass density, Γ_{ext} represents the boundary surface on which external traction T_{ext} is applied, and E is the Green strain tensor. For a finite element of volume V and surface area S, the work balance becomes

$$\int \{\delta u\}^T \{F\} dV + \int \{\delta u\}^T \{\varnothing\} dS + \sum_{i=1}^{n} \{\delta u\}_i^T \{p\}_i$$
$$= \int \left(\{\delta u\}^T \rho \{\ddot{u}\} + \{\delta u\}^T c \{\dot{u}\} + \{\delta \varepsilon\}^T \{\sigma\} \right) dV \tag{2}$$

where {F} and {Φ} represent prescribed body forces and surface tractions, $\{p\}_i$ and $\{\delta u\}_i (\{\delta\varepsilon\}_i)$ represent prescribed concentrated loads and virtual displacements and strains at a total of n points, and c is a damping coefficient. The finite element discretization provides

$$\{u\} = [N]\{d\}; \{\dot{u}\} = [N]\{\dot{d}\}; \{\ddot{u}\} = [N]\{\ddot{d}\}; \{\varepsilon\} = [B]\{d\} \qquad (3)$$

in which N are the shape functions, the nodal displacement vectors $\{d\}$ are functions of time, and [B] is the matrix of shape function derivatives. The equation of motion is

$$[M]\{\ddot{D}\} + [C]\{\dot{D}\} + [K]\{D\} = \{F\} \qquad (4)$$

where the consistent mass (m), damping (c), and stiffness (k) matrices are given by

$$[M] = \int \varrho(\boldsymbol{x})[N]^T[N]dV \; [C] = \int c(\boldsymbol{x})[N]^T[N]dV [K] = \int [B]^T[D(\boldsymbol{x})][B]dV \quad (5)$$

where mass density, damping coefficient, and constitutive matrices are functions of spatial positions.

3. Explicit method, stability, and mass lumping

Dynamic response is evaluated at discrete instants of time separated by time increments Δt. At the nth time step, the equation of motion for linear dynamic problems is given by [34]

$$[M]\{\ddot{u}\}_n + [C]\{\dot{u}\}_n + [K]\{u\}_n = \{F^{ext}\}_n \qquad (6)$$

Discretization in time is accomplished using finite difference approximations of time derivatives. Explicit algorithms use a difference expression of the general form:

$$\{u\}_{n+1} = f\big(\{u\}_n, \{\dot{u}\}_n, \{\ddot{u}\}_n, \{u\}_{n-1}, ...\big) \qquad (7)$$

which contains only historical information on its right-hand side. This difference expression is combined with the equation of motion at time step n.

The stability of the explicit finite element scheme is governed by the Courant condition [34], which provides a critical time step size beyond which the results become unstable. It is given by

$$\Delta t \le l_e / C_d \qquad (8)$$

where l_e is the shortest distance between two nodes in the mesh and the dilatational wave speed C_d is expressed as

$$C_d^2 = \frac{E(x)(1 - \nu(x))}{(1 + \nu(x))(1 - 2\nu(x))\rho(x)} \qquad (9)$$

Since C_d varies due to material gradation, the desired time step for the finite element implementation is chosen based on the largest dilatational wave speed and is maintained constant throughout the simulation. The mass matrix used in the explicit method described above is typically lumped in order to avoid matrix

inversion. The HRZ technique [35] is used to lump the mass matrix in which only the diagonal terms are retained and scaled so as to preserve the total mass:

$$m_{ii}^l = m_{ii} \left(\sum_{j=1}^{n} m_{ij} \right) \Bigg/ \left(\sum_{i=1}^{n} m_{ii} \right) \tag{10}$$

where m^l is the lumped element mass matrix, m is the consistent mass matrix, and n is the number of degrees of freedom in the element.

4. Explicit parallel FEA using MPI

A master-slave approach in the parallel finite element code is used here to solve wave propagation-type problems using the Message Passing Interface (MPI) standard [36]. **Figure 1** shows the procedure used in the parallel execution of the

Initialize number of processors using
MPI_INIT and MPI_COMM_RANK

Partition FE mesh in to sub-meshes manually
Calculate K & M matrices for local elements

Loop over number of timesteps for time
integration using Newmark-beta method

Calculate displacement, velocity, and effective
force vector (EFV) at slaves & master nodes

Slaves send EFV to master for assembly
using MPI_SEND and MPI_RECV

Master returns assembled force vector to
slaves for calculating acceleration vector

Repeat time-integration for the rest of the
simulation by this exchange algorithm
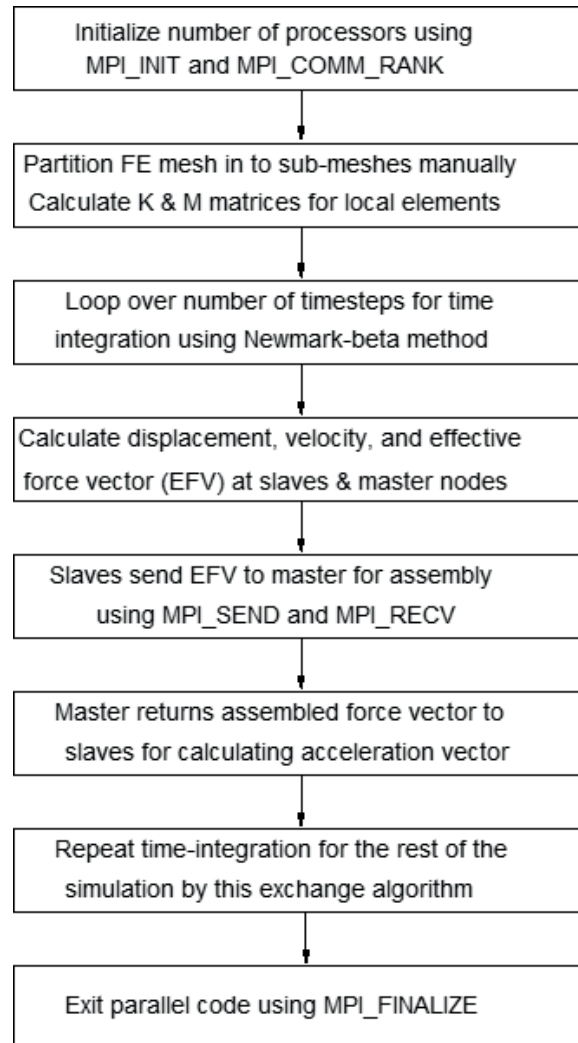
Exit parallel code using MPI_FINALIZE

Figure 1.
Time-integration procedure in the parallel execution of the explicit Newmark-β method [37] using MPI standard [36].

explicit Newmark-β method. The first step is to partition the structure (FE mesh) into number of sub-domains. The stiffness matrices are calculated for elements in the local processor. The stiffness matrix needs not be assembled in an explicit analysis as the algorithm is implemented on an element basis only. The parallel explicit time integration analysis of finite elements from onetime step to another consists in obtaining the unknown velocity and displacement of master and slaves, sending the effective force vector from slaves to the master for assembly and sending back the assembled force vector to the slaves for calculation of acceleration vector. The communication between the slaves and the master processor is done using MPI-based function calls as shown in the figure. The entire force vector at each processor is being sent to the master processor for assembly, and the master processor returns the assembled force vector to the slaves in the same manner. These steps are repeated for the rest of the time integration. Local field quantities like element stresses and strains can be calculated separately on each processor without any communication.

5. Example 1: 3D graded beam under velocity impact

A 3D three-point bending beam under velocity impact is studied to understand the influence of material gradation on the bending behavior in a 3D space. The beam is a real FGM system made of glass/epoxy phases. The dynamic fracture experiments of the linearly graded specimens have been conducted by Rousseau and Tippur [37–40].

In this paper, we investigate the 3D dynamic behavior of a beam. Using 3D explicit finite element code, we can simulate the 3D dynamic behavior of the beam. This 3D finite element study offers enhanced knowledge of the dynamic behavior of this material system and understanding of the stress field in homogeneous and graded materials, which help to predict fracture initiation times in various graded specimens.

Consider a three-point bending specimen under velocity impact load at the top as shown in **Figure 2(a)**. Due to the symmetry of the geometry and the loading conditions, one-fourth of the beam is modeled as shown in **Figure 2(b)**. **Figure 2(c)** and **2(d)** shows the 3D FE mesh of the one-fourth model and a zoom of the FE mesh at the left bottom corner, respectively. The mesh is refined along the loaded edge with a uniform element size of 92.5 μm, and the stress history at point P(0, 0.2 W) is retrieved, where W is the beam depth. Point P is of significance because it corresponds to the location of the crack tip in the dynamic fracture analysis of the cracked beam [38, 41].

Three material gradation cases are considered for the dynamic analysis of the three-point bending beam: a homogeneous beam (Homog, $E_2 = E_1$), a beam stiffer at the impacted surface (StiffTop, $E_2 > E_1$), and a beam softer at the impacted surface (StiffBot, $E_2 < E_1$), where subscripts 1 and 2 denote bottom and top surfaces of the beam, respectively. For the graded beam, Young's modulus (E) is varied linearly between 4 GPa and 12 GPa, and the mass density (ρ) is varied linearly between 1000 kg/cm^3 and 2000 kg/cm^3. These material properties correspond to values used in [42]. For the homogeneous beam, the mass density (ρ) is taken as the average of the graded beam counterparts, and Young's modulus (E) is calculated such that the equivalent E/ρ value equals that of the graded specimen in an average sense, i.e.,

$$\frac{E}{\rho} = \frac{1}{W} \int_0^W \frac{E(y)}{\rho(y)} dy \tag{11}$$
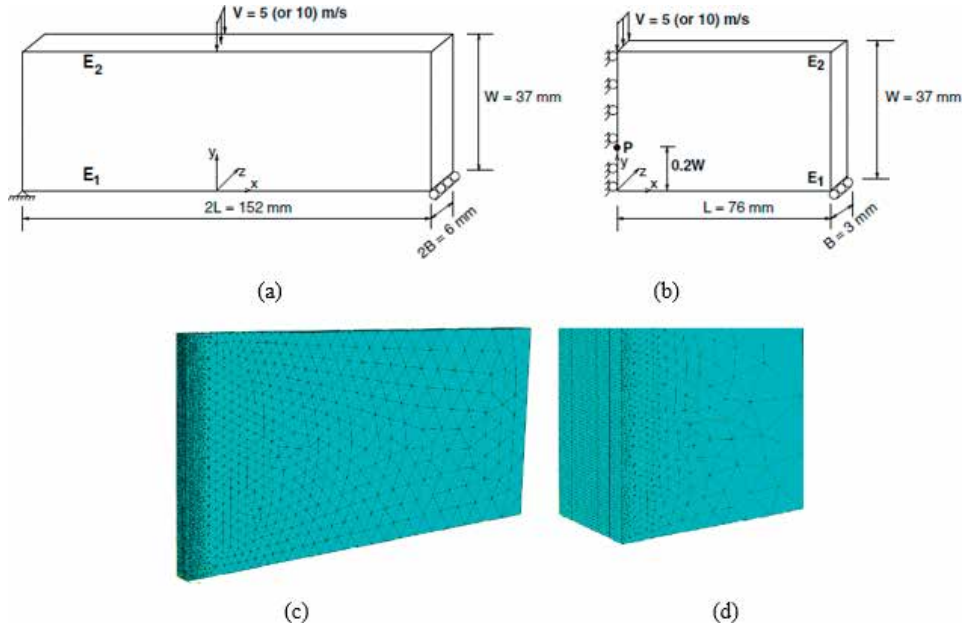
Figure 2.
Epoxy/glass beam subjected to velocity impact: (a) geometry and boundary conditions of the three-point bending specimen and (b) one-quarter model with symmetric boundary conditions. Stress values are retrieved at P(0, 0.2 W). (c) 3D FE mesh of the one-quarter model. The FE mesh contains 14,085 15-node wedge elements and 44,827 nodes. (d) Zoom of the FE mesh near the left bottom corner, i.e., at x = 0.

Poisson's ratio is 0.33 for all the three cases. The average dilatational wave speed ($C_{d(avg)}$) is defined as

$$C_d(avg) = \frac{1}{W} \int_0^W C_d(y)dy \tag{12}$$

where C_d is calculated assuming plane stress behavior given by

$$C_d^2 = \frac{E(y)}{(1 - \nu^2(y))\rho(y)} \tag{13}$$

The dilatational wave speed (C_d) is calculated assuming plane stress behavior to compare results with those obtained by Zhang and Paulino [42]. The difference in $C_{d(avg)}$ for each material gradation is marginal with 2421.5 m/s for the homogeneous beam and 2418.4 m/s for the graded beams. Hence, the dilatational wave speed is assumed constant as 2421.5 m/s, and the results are normalized based on this average dilatational wave speed. Upon impact on the top surface of the beam, compressive stress waves are generated and propagate toward the bottom surface and reflect back as tensile waves from the bottom surface.

A detailed stress history analysis is performed to obtain the influence of material gradation on the bending behavior of the beam. **Figure 3** shows the bending stress (σ_x) history of point P due to impact velocity of 5 m/s for the three cases mentioned above with normalized time $t' = t^*C_d/W$ as the x-axis and stress (MPa) as the y-axis. We see that material gradation leads to considerable change in the stress field at point P. The stress wave takes normalized time of about 0.7 to reach the point P, which is different from 0.8 in Zhang and Paulino [42]. This is due to 3D effects. In a 3D medium, stress waves travel at different speeds when compared to a 2D medium. At this time, the point P undergoes compressive stress until the

normalized time of around 1.1. This compressive stress is due to the Poisson's ratio (ν) effect. In a separate simulation of the beam under similar loading conditions, the Poisson's ratio of the beam was made zero, and we found that the point P underwent tensile stress throughout the simulation (result not shown). From this instant, i.e., after normalized time of 1.1, the point P undergoes monotonically increasing tensile stress. The maximum tensile stress is consistently attained in the StiffTop beam, and the minimum in the StiffBot beam and the Homog beam undergoes stresses in between these two. This type of behavior may be intuitively observed as the material properties (E, ρ) of a StiffTop beam at point P are lower than the StiffBot and Homog beams and hence may undergo higher stresses. We also found that for the line load, the stress component σ_x along the thickness (z) direction at point P(y = 0.2 W) does not vary considerably.

Figure 4 shows the stress history of component σ_y at point P for different material gradations due to impact velocity of 5 m/s. We see that there is a considerable effect of the gradation on this stress behavior, too. The first stress wave approaches point P at normalized time of 0.7 due to the compressive velocity loading. At this point, there is a sudden increase in σ_y stress magnitude (compressive) until a normalized time of 1.25. The stress wave reaches the bottom surface of the beam and reflects as tensile waves at which point there is a gradual decrease in the compressive stress until the normalized time of 2.0. Between normalized times 2.0 and 2.7, the stress behavior does not change considerably, although there are small variations, which may be because of the discrete wave reflections from the edges that occur in finite configurations, to form a plateau in the stress field. The stress wave, after reflecting from the top surface, becomes compressive and leads to an increase in compressive stress between normalized times 2.7 and 3.2. Between the normalized times of 3.2 and 6, the stress behavior tends to repeat itself as seen between 0.7 and 3.2, although with larger variations of increase and decrease. The results plotted in **Figures 13** and **14** are consistent with the plane stress simulation results obtained by Zhang and Paulino [42] and Rousseau and Tippur [38].

Figure 5 shows the 2D contour plot of the stress component σ_x at a specific time instant of 90 μs (t′ ∼ 5.9) for the three beams subjected to the impact velocity of 5 m/s. We firstly see that the stress pattern is considerably different among the
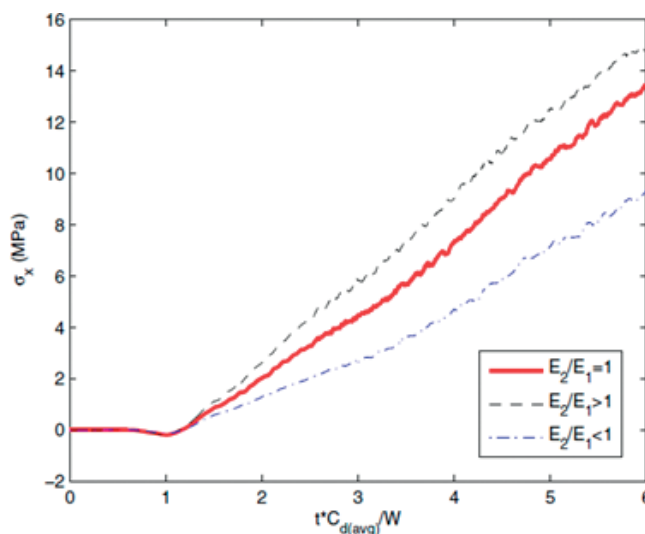

Figure 3.
Stress history σ_x at location P (0, 0.2 W) for homogeneous and graded beams with linearly varying E and ρ, subjected to velocity impact (V = 5 m/s) at the top.
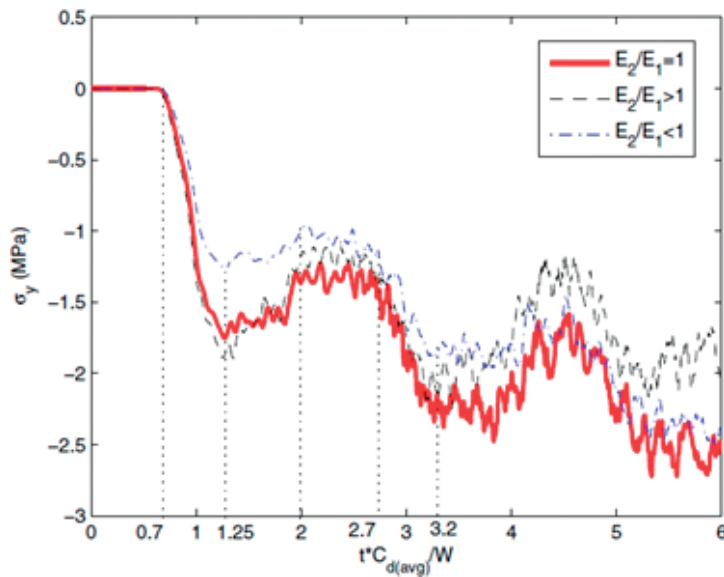
Figure 4.
Stress history σ_y at location P (0, 0.2 W) for homogeneous and graded beams with linearly varying E and ρ, subjected to velocity impact (V = 5 m/s) at the top.

beams considered. Further, at regions close to the loading, compressive stress is concentrated for all the beams, although the size of the compressive zone differs considerably. The StiffTop beam has the largest compressive region at the loading region followed by the Homog beam and the StiffBot beam. At regions close to the loading for the StiffTop beam, we see that the material properties are relatively higher than the other cases and hence the compressive load gets transferred to nearby regions. For the StiffBot case, the compressive region is localized in a small region because of the compliance at the top. Also, we see that the compressive region extends the most in the x direction in the same order as mentioned above. We observe that the size of the tensile zone near the bottom of the beam (i.e., x = 0, y = 0) varies in the same order as the compressive zone at the loading region. The neutral axis location varies for each of the graded beams considered which may be the reason behind the larger tensile region being developed for StiffTop beam when compared to the other two cases. For the dynamic loading considered, the neutral axis shifts in time; nevertheless, the overall stress pattern will be similar to those shown in **Figure 5**. With respect to crack initiation in such graded beams (assuming that the crack lies parallel to the applied loading), we know that the σ_x stress component dominates the most. We see that the StiffTop beam is consistently subjected to larger tensile stresses than other two cases at point P and will lead to earlier crack initiation.

Figures **6** and **7** show the σ_x and σ_y plots for the different graded beams subjected to 5 m/s and 10 m/s velocities of impact. We see that the stress behavior increases linearly (gets doubled almost) for V = 10 m/s when compared to the case of V = 5 m/s for all the gradation cases.

We have so far investigated the 2D dynamic behavior of a beam under the line load using 3D finite element method. Using 3D explicit finite element code, we can simulate the 3D dynamic behavior of the beam. We apply the impact point load of V = 10 m/s at a central node at the top edge of the beam. Note that this cannot be simulated using 2D finite elements in Zhang and Paulino [41]. The stress history results are obtained at point P and compared against those shown in **Figure 7**.

(a) *StiffBot*

(b) *Homogeneous*
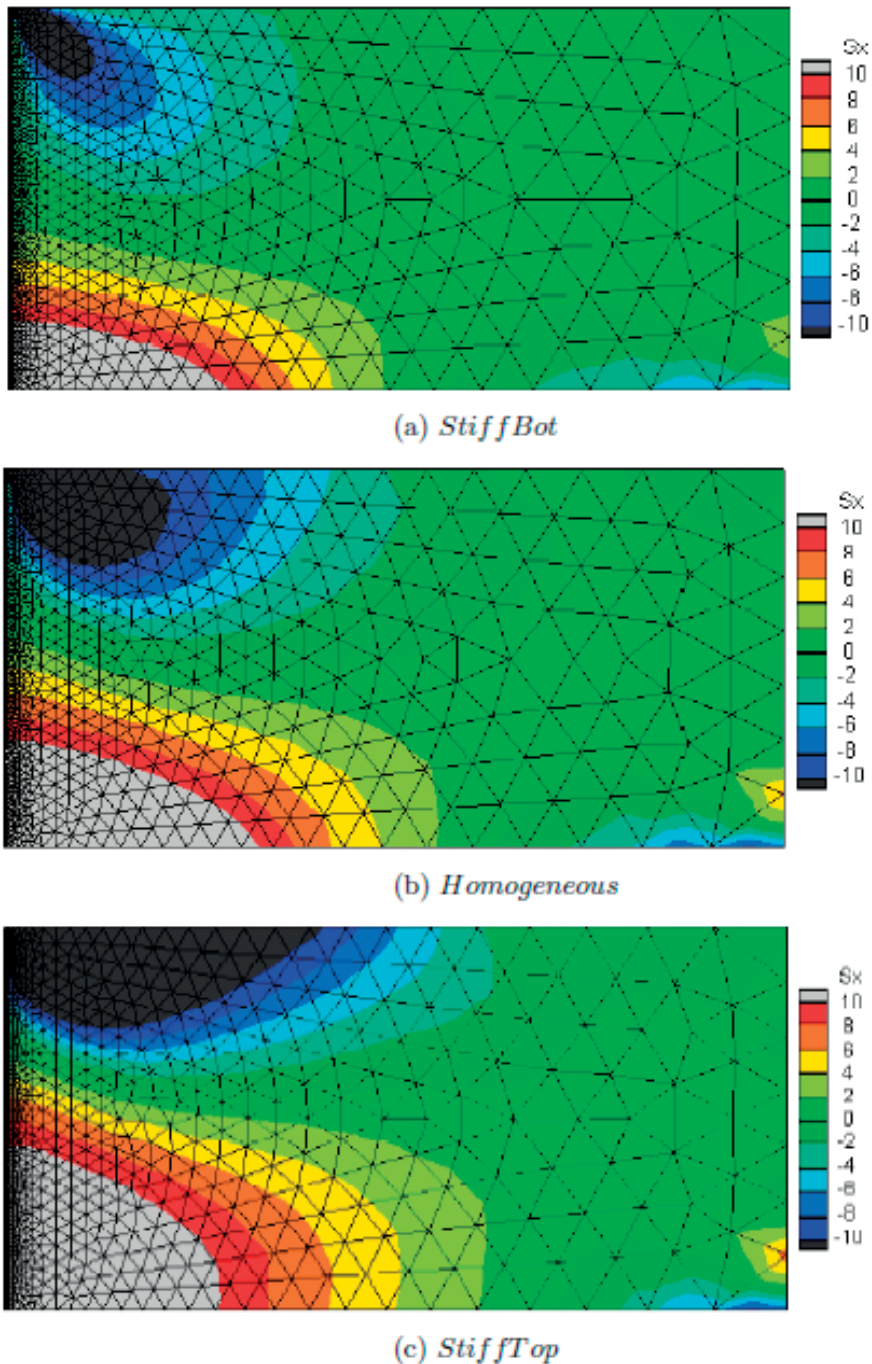
(c) *StiffTop*

Figure 5.
Stress contour (σ_x MPa) at t = 90 μs due to impact velocity of 5 m/s. (a) StiffBot beam ($E_2 < E_1$), (b) homogeneous beam ($E_2 = E_1$), and (c) StiffTop beam ($E_2 > E_1$).

Figures 8 and **9** show the comparison of σ_x and σ_y, respectively, for the three beams under impact velocity of V = 10 m/s applied throughout the thickness (line load) and at one central node (point load). We see that the stresses for the latter case (point load) are much lower than the former case (line load). Maximum tensile stress (σ_x) at point P due to point load is experienced by the StiffTop beam followed by the Homog beam and the StiffBot beam, similar to the line load case. The stress
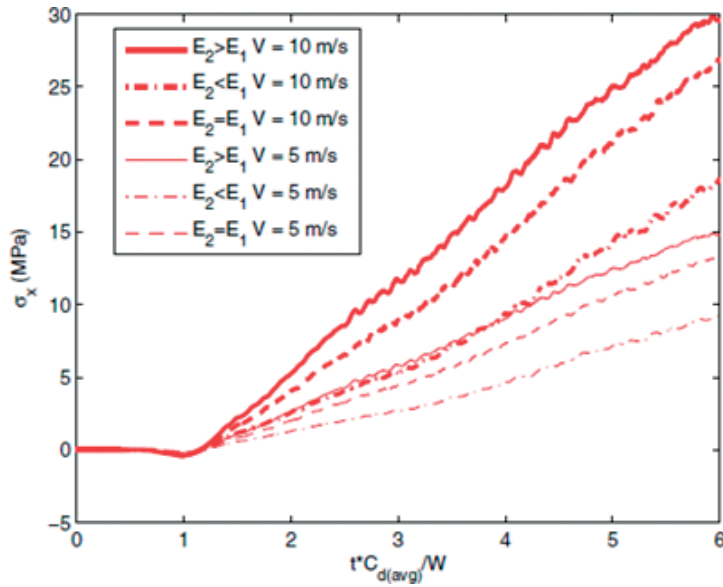
Figure 6.
Stress history σ_x at location P(0, 0.2 W) for homogeneous and graded beams subjected to two different velocities.
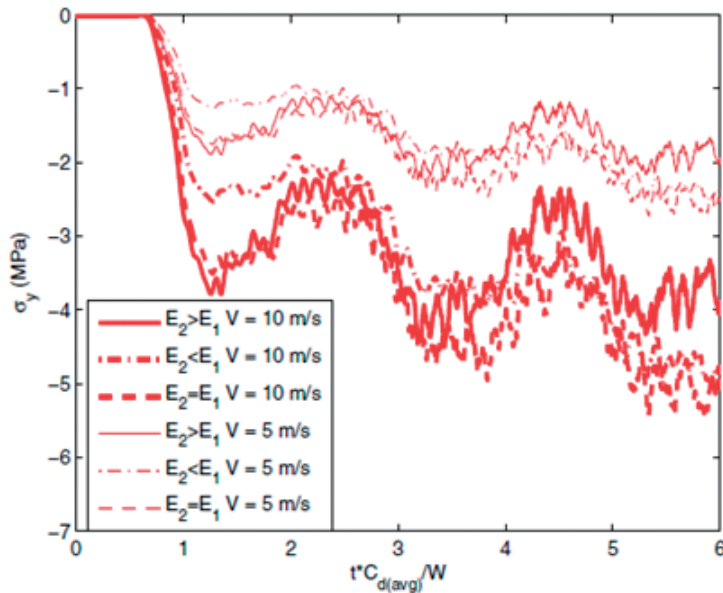
Figure 7.
Stress history σ_y at location P(0, 0.2 W) for homogeneous and graded beams subjected to two different velocities.

values at point P across the z (thickness) direction do not change noticeably (result not shown).

6. Example 2: wave propagation in 3D bar

Wave propagation in a fixed-free 3D bar with homogeneous and graded materials in the vertical direction (y) is simulated to illustrate the relevance of material gradation and also to verify the parallel explicit 3D finite element code. Consider a
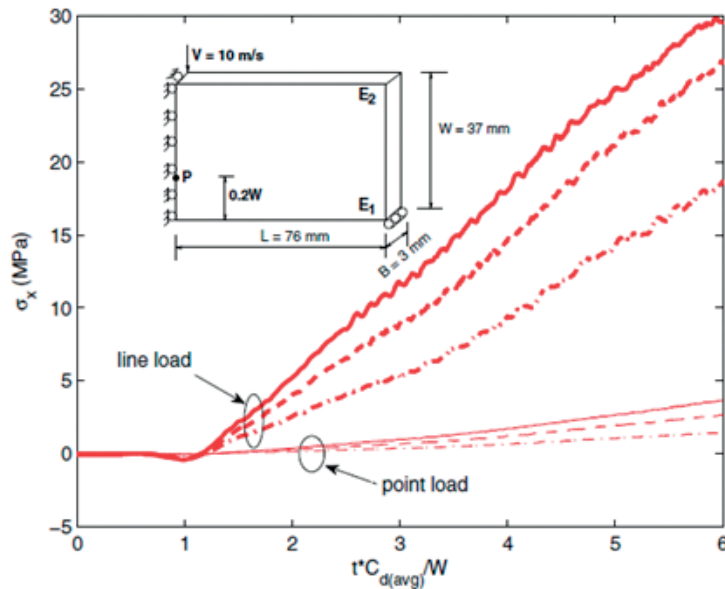
Figure 8.
Stress history σ_x at location P(0, 0.2 W) for homogeneous and graded beams subjected to impact velocity of 10 m/s as a line load and point load (see the insert). Thick and thin lines correspond to line load and point load, respectively. Solid, dashed, and dash-dot lines correspond to StiffTop, Homog, and StiffBot beams.
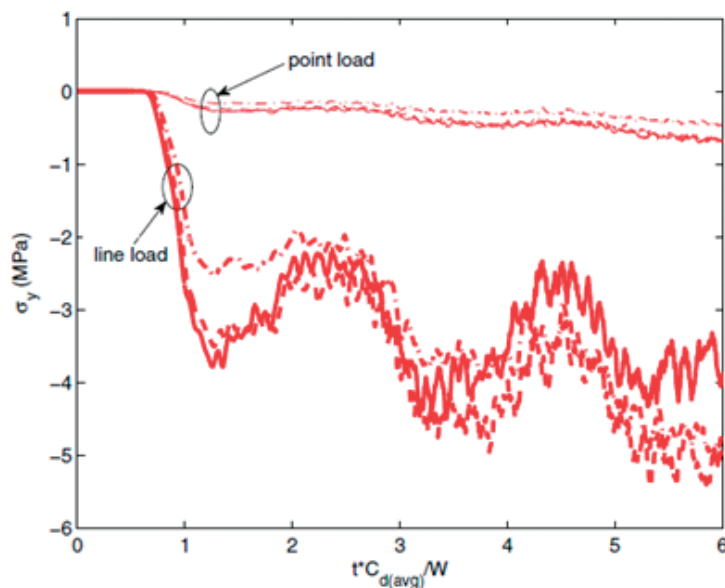
Figure 9.
Stress history σ_y at location P(0, 0.2 W) for homogeneous and graded beams subjected to impact velocity of 10 m/s as a line load and point load (see the insert). Thick and thin lines correspond to line load and point load, respectively. Solid, dashed, and dash-dot lines correspond to StiffTop, Homog, and StiffBot beams.

fixed-free bar in **Figure 10(a)**. The square bar is of length L = 1 m and height H = 0.05 m. A step loading is used (**Figure 10(b)**) at the free end of the bar. The material considered is steel for the homogeneous bar and steel and alumina for the graded bar. The properties of steel and alumina are given in **Table 1**. For the graded bar, the lower surface of the bar is made of alumina, and the upper part is made of steel, and the material properties vary linearly from alumina to steel.
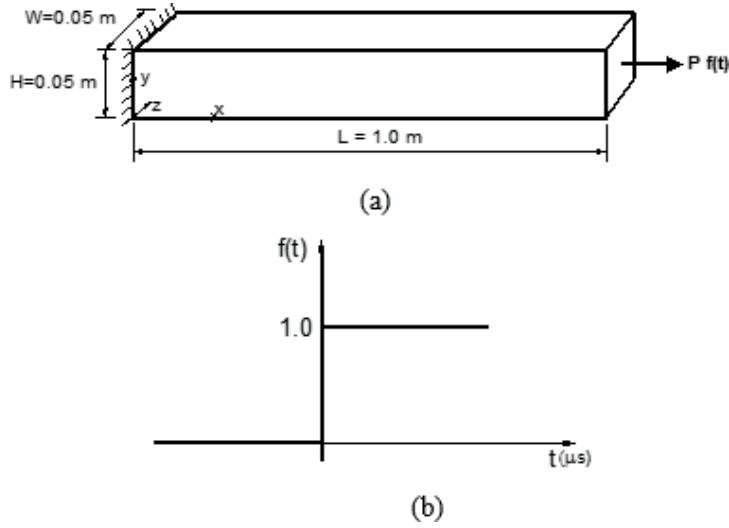
Figure 10.
(a) Schematic of the 3D bar and (b) step load.

Material	E (GPa)	ν	ρ (kg/m³)	C_d (m/s)
Steel	210	0.31	7800	6109
Alumina	390	0.22	3950	10,617

Table 1.
Material properties of steel and alumina.

Explicit time integration method is used for analyzing wave propagation type of problems since it avoids storage of large matrices and does not require the solution of global systems of equations, but is limited by its conditional stability [43]. The time step size has to be smaller than a critical value which is directly dependent on the largest frequency of the FE discretization (smallest element). Higher-order modes participate in the bar response which in turn requires refined element size. To capture the transient response, the time step size needs to be small enough in order to also track the change of applied loads, and adequate element size can be estimated according to the Courant condition [34]. Considering material gradation in the y direction, the FE mesh is discretized into 300 × 15 × 15 quads, each quad divided into four 15-node wedge elements, totaling 270,000 elements and 725,836 nodes. The 1D analytical solution for the motion of a bar with step force loading at the free end is obtained using a finite sine transform method given by [44]

$$u(x,t) = \frac{P_0}{EA}x - \frac{8P_0 L}{\pi^2 EA} \sum_{n=1}^{\infty} \frac{(-1)^{n-1}}{(2n-1)^2} \sin\left((2n-1)\frac{\pi x}{2L}\right) \cos\left((2n-1)\frac{\pi c}{2L}t\right) \quad (14)$$

where P_0, E, A, L, and c represent the applied force magnitude, the Young's modulus, cross-sectional area, length, and dilatational wave speed of the bar, respectively. The first term on the right side of Eq. (14) is the static solution, whereas the series represents a superposition of normal modes of amplitudes inversely proportional to $(2n-1)^2$. The axial stress can be easily obtained by differentiating displacement Eq. (14).

Results are presented for the 3D wave propagation in a bar under step loading considering homogeneous and graded material properties. **Figures 11** and **12** show
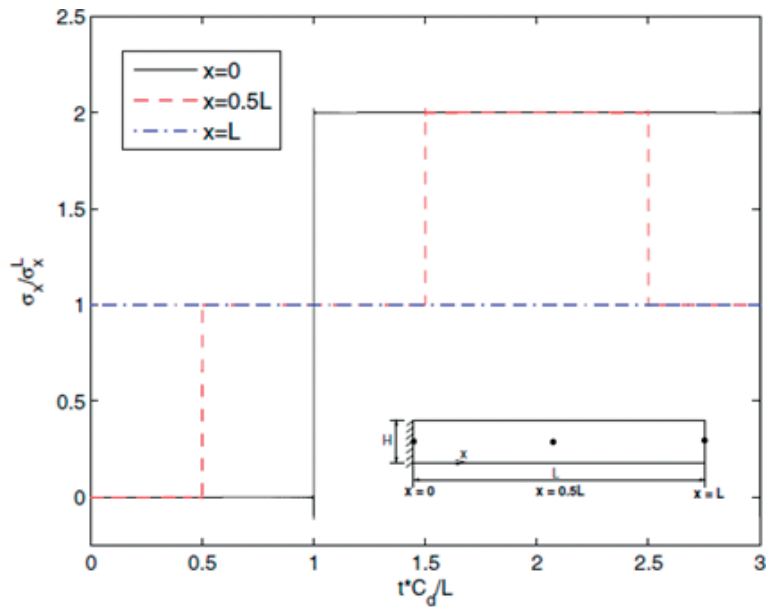
Figure 11.
Normalized longitudinal stress history at three locations (see the insert) of the homogeneous bar subjected to step loading using 1D analytical solution given in Eq. (14).
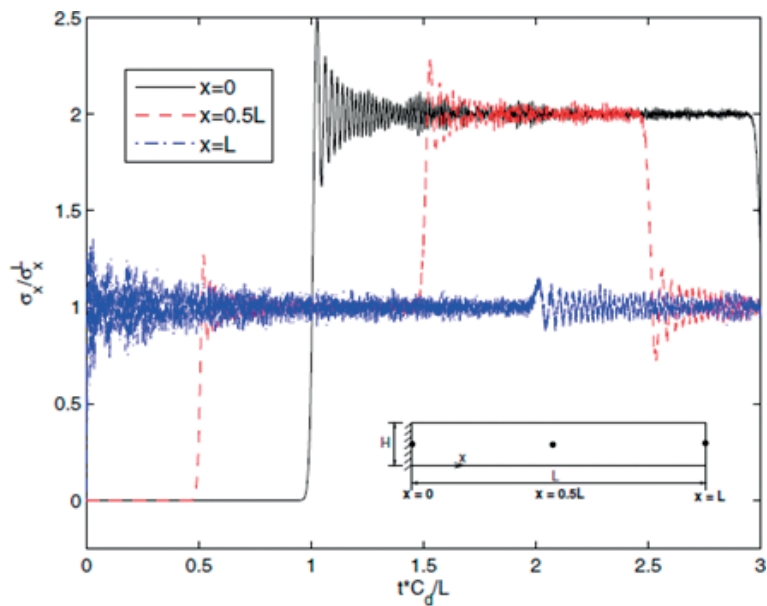
Figure 12.
Normalized longitudinal stress history at three locations (see the insert) of the homogeneous bar subjected to step loading obtained using finite element analysis.

the normalized longitudinal stress at three locations along the x-axis obtained using the exact solution and the finite element method, respectively. For the exact solution, we see small oscillation of the stress solution at x = 0 at t = 1 which is due to finite series of n used in Eq. (14). Poisson's ratio (ν) is taken as zero for the present finite element simulation. From the figures, we see that the overall stress behavior of the finite element simulation is similar to the exact solution, although there are

some oscillations. These oscillations are seen at times when there is a sudden increase or decrease in stress due to wave reaching a certain location in the bar. This oscillation effect may be due to discrete wave reflections that occur in finite configurations and also due to the finite element discretization.

Figures 13 and **14** show the normalized longitudinal stress at six locations (see the insert) for the functionally graded bar along z = 0.025 m and z = 0 m,
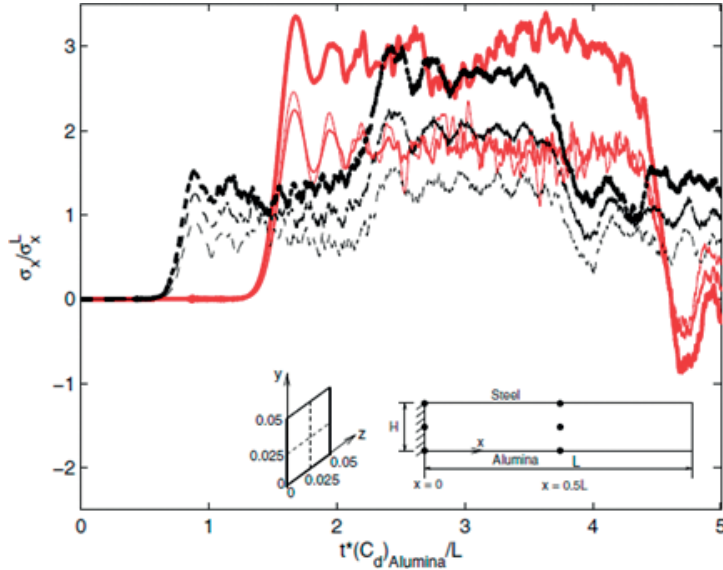
Figure 13.
Normalized longitudinal stress history of six points (see the insert) on a graded bar (z = 0.025 m) subjected to step loading. Solid and dashed lines indicate points at x = 0 and x = 0.5 L, respectively. Thick, intermediate-thick, and thin lines indicate alumina-rich side, midplane, and steel-rich side points, respectively.
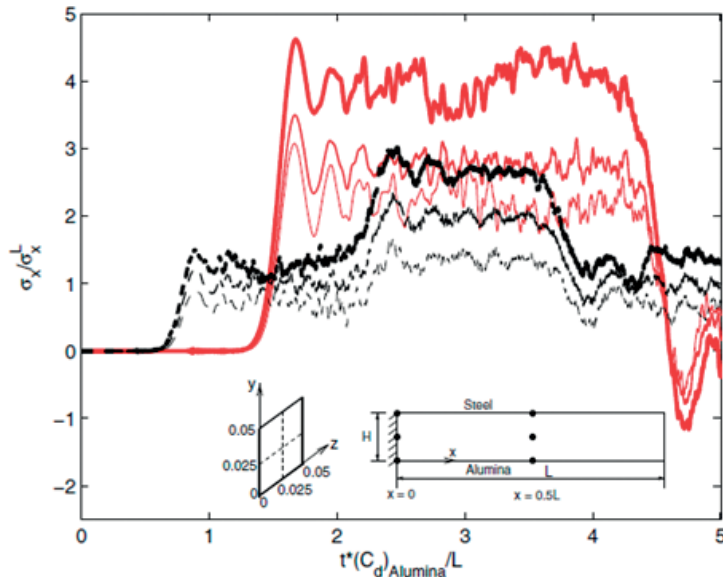
Figure 14.
Normalized longitudinal stress history of six points (see the insert) on a graded bar (z = 0 m) subjected to step loading. Solid and dashed lines indicate points at x = 0 and x = 0.5 L, respectively. Thick, intermediate-thick, and thin lines indicate alumina-rich side, midplane, and steel-rich side points, respectively.

respectively. The stress history at x = L is not plotted as the behavior is similar to the homogeneous case. We see that the stress wave gets distorted in time because of the material gradation. The stress wave at x = 0.5 L and mostly at x = 0 differs highly across the thickness direction due to difference in wave speeds. As expected, the alumina side undergoes higher stresses than the steel side, more so at the fixed end than at other x locations.

7. Conclusions

Dynamic and wave propagation behavior of 3D functionally graded continua is investigated using explicit finite element formulations. Three numerical examples are presented. The first example is on dynamic analysis of a three-point bending beam made of epoxy and glass phases under low-velocity impact. Material gradation considerably affects the dynamic stress behavior of the beam. Tensile stress is maximum for StiffTop beam at the imaginary crack-tip location for stress component (σ_x) indicating that crack initiation will occur earlier for this type of beam which was also verified by experiments conducted by Rousseau and Tippur [40].

The second example is on 3D wave propagation behavior of a homogeneous and functionally graded bar under sinusoidal and step loading. Stress results for the homogeneous bar with zero Poisson's ratio obtained using the finite element method match very well with the exact solution. Poisson's ratio and material constraints in a 3D continuum affect the stress behavior for both homogeneous and functionally graded bars. In the functionally graded bar, the alumina side consistently experienced more stress than the steel side. Finite element modeling and simulation discussed herein can be a critical tool to help understand physics behind the dynamic events.

Author details

Ganesh Anandakumar and Jeongho Kim*
Department of Civil and Environmental Engineering, University of Connecticut, Storrs, CT, USA

*Address all correspondence to: jeongho.kim@uconn.edu

IntechOpen

References

[1] Ootao Y, Kawamura R, Tanigawa Y, Imamura R. Optimization of material composition of nonhomogeneous hollow circular cylinder for thermal stress relaxation making use of neural network. Journal of Thermal Stresses. 1999;**22**:1-22

[2] Ilschner B. Processing-microstructure-property relationships in graded materials. Journal of the Mechanics and Physics of Solids. 1996;**44**(5):647-656

[3] Hirano T, Teraki J, Yamada T. On the design of functionally gradient materials. In: Yamanouochi M, Koizumi M, Hirai T, Shiota I, editors. Proceedings of the First International Symposium on Functionally Gradient Materials. Japan: Sendai; 1990. pp. 5-10

[4] Gupta A, Shirvanimoghaddam K. Functionally graded materials: A review of fabrication and properties. Applied Materials Today. 2016;**5**:223-245

[5] Liew KM, Lei ZX, Zhang LW. Mechanical analysis of functionally graded carbon nanotube reinforced composites: A review. Composite Structures. 2015;**120**:90-97

[6] Sola A, Bellucci D, Cannillo V. Functionally graded materials for orthopedic applications – an update on design and manufacturing. Biotechnology Advances. 2016;**34**(5): 504-531

[7] Osaka T, Matsubara H, Homma T, Mitamura S, Noda K. Microstructural study of electroless-plated CoNiReP/NiMoP double-layered media for perpendicular magnetic recording. Japanese Journal of Applied Physics. 1990;**29**(10):1939-1943

[8] Watanabe Y, Nakamura Y, Fukui Y, Nakanishi K. A magnetic-functionally graded material manufactured with deformation-induced martensitic transformation. Journal of Materials Science Letters. 1993;**12**(5):326-328

[9] Koike Y. Graded-index and single mode polymer optical fibers. In: Chiang LY, Garito AG, Sandman DJ, editors. Electrical, Optical, and Magnetic Properties of Organic Solid State Materials. Vol. 247. Pittsburgh, PA: Materials Research Society Proceedings; 1992. p. 817

[10] Udupa G, Rao SS, Gangadharan KV. Functionally graded composite materials: An overview. Procedia Materials Science. 2014;**5**:1291-1299

[11] Miyamoto Y, Kaysser WA, Rabin BH, Kawasaki A, Ford RG. Functionally Graded Materials: Design, Processing and Applications. Berlin, Germany: Springer; 2013

[12] Kieback B, Neubrand A, Riedel H. Processing techniques for functionally graded materials. Materials Science and Engineering A. 2003;**362**(1-2):81-106

[13] Hart NT, Brandon NP, Day MJ, Shemilt JE. Functionally graded cathodes for solid oxide fuel cells. Journal of Materials Science. 2001;**36**: 1077-1085

[14] Barthel K, Rambert C. Thermal spraying and performance of graded composite cathodes as SOFC-component. Materials Science Forum. 1999;**308-311**:800-805

[15] Holtappels P, Bagger C. Fabrication and performance of advanced multi-layer sofc cathodes. Journal of the European Ceramic Society. 2002;**22**:41-48

[16] Gerk C, Willert-Porada M. Development of graded composite electrodes for the SOFC. Materials Science Forum. 1999;**308-311**:806-815

[17] Suresh S, Mortensen A. Fundamentals of Functionally Graded Materials. London: IOM Communications Ltd; 1998

[18] Chakraborty A, Gopalakrishnan J. A spectrally formulated finite element for wave propagation analysis in functionally graded beams. International Journal of Solids and Structures. 2003;**40**(10):2421-2448

[19] Chiu TC, Erdogan F. One-dimensional wave propagation in a functionally graded elastic medium. Journal of Sound and Vibration. 1999;**222**(3):453-487

[20] Reddy JN, Chin CD. Thermomechanical analysis of functionally graded cylinders and plates. Journal of Thermal Stresses. 1998;**26**(1):593-626

[21] Gong SW, Lam KY, Reddy JN. The elastic response of functionally graded cylindrical shells to low-velocity impact. International Journal of Impact Engineering. 1999;**22**:397-417

[22] Rousseau C-E, Tippur HV. Compositionally graded materials with cracks normal to the elastic gradient. Acta Materialia. 2000;**48**(16):4021-4033

[23] Rousseau C-E, Tippur HV. Dynamic fracture of compositionally graded materials with cracks along the elastic gradient: Experiments and analysis. Mechanics of Materials. 2001;**33**:403-421

[24] Rousseau C-E, Tippur HV. Evaluation of crack tip fields and stress intensity factors in functionally graded elastic materials: Cracks parallel to elastic gradient. International Journal of Fracture. 2002;**114**:87-111

[25] Cheng Z, Zhang G, Wang Y, Bobaru F. A peridynamic model for dynamic fracture in functionally graded materials. Composite Structures. 2015;**133**:529-546

[26] Lindholm US, Doshi KD. Wave propagation in an elastic nonhomogeneous bar of finite length. Journal of Applied Mechanics. Transactions ASME. 1965;**32**:135-142

[27] Karlsson A, Otterheim H, Stewart R. Transient wave propagation in composite media: Green's function approach. Journal of the Optical Society of America A. Optics and Image Science. 1993;**10**:886-895

[28] Santare MH, Thamburaj P, Gazonas GA. The use of graded finite elements in the study of elastic wave propagation in continuously nonhomogeneous materials. International Journal of Solids and Structures. 2003;**40**:5621-5634

[29] Ekevid T, Wiberg N-E. A comparison of parallel implementation of explicit DG and central difference method. Communications in Numerical Methods in Engineering. 2002;**18**:585-597

[30] Krysl P, Belytschko T. Object-oriented parallelization of explicit structural dynamics with PVM. Computers and Structures. 1998;**66**(2-3):259-273

[31] Krysl P, Bittnar Z. Parallel explicit finite element solid dynamics with domain decomposition and message passing: Dual partitioning scalability. Computers and Structures. 2001;**79**:345-360

[32] Rao ARM. Explicit nonlinear dynamic finite element analysis on homogeneous/heterogeneous parallel computing environment. Advances in Engineering Software. 2006;**37**:701-720

[33] Rao ARM. A parallel mixed time integration algorithm for nonlinear dynamic analysis. Advances in Engineering Software. 2002;**33**:261-271

[34] Bathe K-J. Finite Element Procedures. New Jersey: Prentice-Hall; 1996

[35] Hilber HM, Hughes TJR, Taylor RL. Improved numerical dissipation for time integration algorithms in structural dynamics. Earthquake Engineering and Structural Dynamics. 1977;**5**:283-292

[36] MPI-2: Extension to the Message Passing Interface. Knoxville, Tennessee: University of Tennessee; 1997

[37] Rousseau C-E, Tippur HV. Compositionally graded materials with cracks normal to the elastic gradient. Acta Materialia. 2000;**48**(16): 4021-4033

[38] Rousseau C-E, Tippur HV. Dynamic fracture of compositionally graded materials with cracks along the elastic gradient: Experiments and analysis. Mechanics of Materials. 2001a;**33**: 403-421

[39] Rousseau C-E, Tippur HV. Influence of elastic gradient profiles on dynamically loaded functionally graded materials: Cracks along the gradient. International Journal of Solids and Structures. 2001b;**38**:7839-7856

[40] Rousseau C-E, Tippur HV. Evaluation of crack tip fields and stress intensity factors in functionally graded elastic materials: Cracks parallel to elastic gradient. International Journal of Fracture. 2002;**114**:87-111

[41] Zhang Z, Paulino GH. Cohesive zone modeling of dynamic fracture in homogeneous and functionally graded materials. International Journal of Plasticity. 2005;**21**(6):1195-1254

[42] Zhang Z, Paulino GH. Wave propagation and dynamic analysis of smoothly graded heterogeneous continua using graded finite elements. International Journal of Solids and Structures. 2007;**44**:3601-3626

[43] Rao ARM. Explicit nonlinear dynamic finite element analysis on homogeneous/heterogeneous parallel computing environment. Advances in Engineering Software. 2006;**37**:701-720

[44] Meirovitch L. Analytical Methods in Vibrations. New York: The Macmillan Company; 1967

Chapter 3

A New Concept to Numerically Evaluate the Performance of Yielding Support under Impulsive Loading

Faham Tahmasebinia, Chengguo Zhang, Ismet Canbulat,
Samad M.E. Sepasgozar, Onur Vardar, Serkan Saydam
and Chen Chen

Abstract

The dynamic capacity of a support system is dependent on the connectivity and compatibility of its reinforcement and surface support elements. Connectivity refers to the capacity of a system to transfer the dynamic load from an element to another, for example, from the reinforcement to the surface support through plates and terminating arrangements (split set rings, nuts, etc.), or from a reinforcement/ holding element to others via the surface support. Compatibility is related to the difference in stiffness amongst support elements. Load transfer may not take place appropriately when there are strong stiffness contrasts within a ground support system. Case studies revealed premature failures of stiffer elements prior to utilising the full capacity of more deformable elements within the same system. From a design perspective, it is important to understand that the dynamic-load capacity of a ground support system depends not only on the capacity of its reinforcement elements but also, and perhaps most importantly, on their compatibility with other elements of the system and on the strength of the connections. The failure of one component of the support system usually leads to the failure of the system.

Keywords: fully grouted rock bolts, yielding support, coal burst, shear dynamic loading

1. Introduction

Currently, rock/cable bolts and steel mesh are widely used as temporary and permanent support element in tunnelling, underground excavations, and the surface slope stability. A combination of the rock/cable bolts and steel mesh can provide a robust system, which is known as a combined or yielding support. A combined support can transfer the applied external load from the damaged exterior to the confined interior of a rock mass. The load transferring mechanism between the unstable exterior and interior of a rock mass by means of the combined support system is still of the grey areas in designing the support systems. The understanding the load transferring mechanism between the engaged elements in a rock mass will

be more complicated when it comes to designing effective elements against rock/coal burst. Ref. [1] defined ground support as a combination of surface support and reinforcement systems. Ref. [1] also mentioned that the words support and reinforcement are usually used interchangeably. Another concept to recall the support system as a membrane system is determined by [2]. Ref. [2] classified the surface support or containment support as the application of the reaction of the forces at the face of the excavation where it can include the techniques and smart devices to establish both local and global supports. These techniques and devices included fill, timber, steel sets, shotcrete, and the steel mesh. Ref. [3] defined rock reinforcement as an enhancement of the overall rock mass properties within the rock mass, and contain all techniques and devices that perform within the rock mass, including rock bolts, cable bolts, and ground anchors. Dynamic support is defined as ground support systems in which it would be available to resist against sudden energy release and dynamic loading so as to uphold the strength of an underground excavation. A number of researchers including [4–8] focused on studying the shear behaviour of rock bolts when it comes to the high stress and jointed rock mass condition. Ref. [9] classified the procedure for rock mass damage mechanisms by including the sudden volume expansion or bulking of the rock due to fracturing of the rock mass around an excavation. Rock mass bulking is a major cause of damage to support burst-prone condition.

2. Overview of research on yielding support

Ansell [10] carried out further tests on another type of energy-absorbing rock bolt made of soft steel. The aim of the test was to determine the strain rate effects on the yield stress and ultimate strength of the steel bars under dynamic loading conditions. The results demonstrated that the strain rate has a pronounced influence on the yield stress of steel bars. Ansell [10] concluded that the yield stress, the ultimate strength, and the energy absorbing capacity increased with the increasing loading rate, and the soft steel bars had a delayed plastic yielding when subjected to the dynamic loading. The impact was plastic during the retardation of the movable components of the testing machine; it was large at the beginning but dropped dramatically as an exponential curve. Ansell [10] also proposed that a rock bolt used under dynamic loading should have high dynamic-yield capacity so that it can resist high peak forces when experiencing impact loading. There are two methods commonly used to test energy absorption capacity of rock bolts under dynamic loading: free fall of a mass and momentum transfer. Plouffe et al. [11] performed the free fall method in the laboratory, where dynamic loading was simulated by dropping a mass over a certain distance onto the impact plate attached to the lower tube. The load and the displacement at the split were recorded by a load cell under the plate and a differential extensometer, respectively. The performance of bolts under dynamic loading was then analysed in terms of loads, displacements, and energy dissipated. The results showed that the potential and kinetic energies were almost equal to each other, and not all the energy was transferred to the support elements. The dissipated energy results in noise and permanent deformation of the domed plate. An experiment was carried out by [12] to estimate the energy absorption capacity of a new rock bolt, named D bolt, which has a large capacity for load bearing and deformation. Both static pull tests and dynamic drop tests were performed to evaluate the characteristics of the D bolt. For dynamic tests, boreholes were simulated by a split steel tube, which was placed in a jig to align it with a drill. During the test, a mass was dropped from a certain height onto a plate connected to the D bolt, and the impact load and the plate load were then measured during the

dropping process. The results indicated that the D bolt's impact peak load capacity was slightly larger than the static tensile strength of the bolt. The D bolt absorbed a large amount of energy along its entire length. The bolt was equally loaded in each deformable section which worked alone to stop rock expansion. Ghadimi et al. [13] developed an analytical model to calculate shear stress in a fully grouted rock bolt in jointed rock mass. The model considered the bolt profile and jump plane under pull test conditions. The results demonstrated that shear stress from the bolt to the rock decreased in an exponential rate. This decrease in shear stress is determined by bolt profiles such as the height, width and spacing of rib, resin thickness, material, and jointed properties. Jiang et al. [14] proposed another analytical model of the grouted rock bolt. The coupling behaviour of the rock bolt and rock mass was discussed from the point of displacement. Based on the analysis, the initial force in rock mass was controlled by its displacement. Another finding was that each bolt has at least one neutral point whose position is influenced by the displacement in the rock mass around the tunnel. The axial force of a rock bolt and the shear stress at the interface between the bolt and rock mass were affected by the length of the rock bolt, the internal radius of the tunnel, and the characteristics of the rock mass. A similar analytical model was also proposed by [15], in which the stress of distribution and variation of fully grouted rock bolts in surrounding rock mass were investigated and analysed. Based on the stress equilibrium in a tiny area of a rock bolt and the shear stress transfer mechanism of the interface between the rock bolt and rock mass, the axial displacement differential equation of the rock bolt was developed. Aziz et al. [16] researched the load transfer capacity of fully grouted rock bolts under an elastoplastic rock mass condition and proposed an analytical solution to determine the axial load along the rock bolts. In this model, the rock bolts were assumed to be elastic material and the surrounding rock mass was considered as an elastoplastic material. According to the model analysis, the load transfer capacity of a fully grouted rock bolt can be expressed as a function of various parameters of the surface condition, including bolt length, shear stiffness of the interfaces, in situ stress, and rock displacement along the bolt. Rock bolts are part of the reinforcement support system in underground excavations. It is important to evaluate and understand the performance of bolts under varying loads. Laboratory testing methods, especially the double shear test, can be used to determine the mechanical properties of rock bolts under static loading. Tests for rock bolts under dynamic loading are used to determine the energy absorption capacity, which is an important parameter for describing the dynamic performance of a rock bolt. Numerical modelling by using simulation software and theoretical analysis can also be used to analyse the behaviour of rock bolts in a jointed rock mass. Since experimental investigation of cable bolts under dynamic loading is very complicated and requires sophisticated facilities, numerical modelling can be used as a reliable method.

3. Numerical procedure

The proposed three-dimensional Finite Element model is developed using the commercial software ABAQUS, due to its ability to deal with complex contact problems. In fact, one of the main difficulties in the modelling of steel and concrete members with ABAQUS is in the convergence issues which need to be addressed due to the extensive number of contacts required to be implemented between the cable bolt and the concrete boxes. The proposed numerical model is developed to predict the structural response of the cable bolts using solid elements for all components. For this purpose, the 8-node linear brick element (C3D8R) with a reduced

integration and hourglass control is adopted, which is the element with three transitional degrees of freedom (**Figure 1**).

One of the main difficulties in the modelling of steel and concrete members with ABAQUS is in the convergence issues which need to be addressed due to the extensive number of contacts required to be implemented between the cable bolt and the concrete blocks. The proposed numerical model is developed to simulate the structural response of the cable bolts using solid elements for all components. For this purpose, the 8-node linear brick element (C3D8R) with a reduced integration and hourglass control is adopted, which is the element with three transitional degrees of freedom. The base model in this chapter is similar to the author's previous work [17], where preliminary numerical modelling and analytical study were conducted to examine cable behaviour. This study provides further parametric analysis on bolts behaviour under different conditions. The adequacy and stability of a Finite Element model to describe the behaviour of a cable bolt is strongly influenced by the definition of adequate contact properties between the concrete and steel components, as suggested by [17]. The presence of a large number of contact regions, especially when dealing with cable bolt models, significantly increases the complexity of the analysis due to the nonlinear and discontinuous nature of cable bolts. For this reason, the Finite Element simulations carried out as part of this study are implemented with ABAQUS/Explicit, to avoid convergence difficulties. The interface behaviour between the concrete box and the cable bolt is modelled using the surface-to-surface interaction available in ABAQUS. In particular, a HARD contact property is adopted in the direction normal to the interface plane. For the tangential behaviour, the PENALTY option is used with a friction coefficient of 0.5 between the cable bolts and the grout. The behaviour of the cable bolts is described using a linear elastic relationship up to yielding, followed by a strain-hardening behaviour. The concrete in compression is described with an initial linear elastic range up to 40% of its compressive strength after which it is represented by the Concrete Damage Plasticity model available in ABAQUS. Its
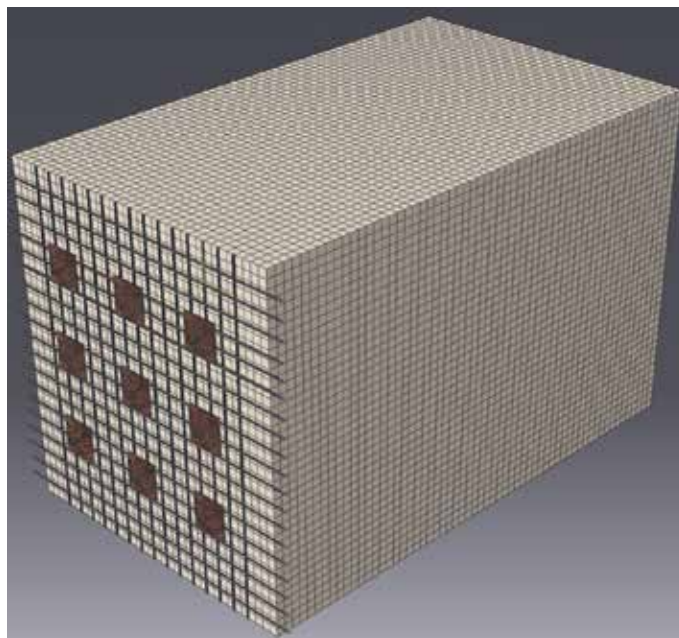

Figure 1.
An example of 3-D finite element models under static and dynamic loading.

tensile behaviour is initially linear elastic followed by a softening response after cracking is initiated.

4. Analytical and numerical solution

Plate is one of the important elements which may influence the overall performance of the combined support. To date, a little attention was devoted by the industry to evaluate the performance of the plate in the roof and rib blot system. The strength of the head plate can be part of a roof or rib bolt system component. However roof bolting system that uses pre-tension for reinforcing purposes may not always achieve full encapsulation, the head plate is in fact a vital component of the system. Thus, at this stage, different and critical buckling modes in a steel plate with hole in the centre of the plate were presented. A number of researchers [18–22] theoretically and experimentally reported buckling of square plates with central circular holes subjected to compression in the plane. The presented theoretical methods by most of the researchers [18–21] calculate the critical loads in a plate with hole in the centre were extracted from the minimum energy method [23]. However, the available methods buckling and post-buckling solutions, which are mathematically discussed, are limited to small hole sizes, and are not able to study the effects of different boundary conditions of the plate on the strengths of buckling plates with holes of arbitrary size. By inventing powerful computers and advantaging from simulating Finite Element software, it is now possible to calculate the stresses of post-buckling for rectangular plates with any aspect ratio, any shapes and sizes of cuts, and in different boundary conditions. **Figure 2** illustrates the applied boundary conditions and the applied pressure on the top and bottom edges. Initially, a fundamental method is presented for computing the compressive buckling load of a simply supported elastic rectangular plate having a central circular hole.

Subsequently, a three-dimensional Finite Element model is developed to comprehensively compute the critical buckling load in a rectangular plate having a central circular hole. The developed models will be extended to simulate the post-buckling analysis in the future research reports. An energy method to determine the buckling load of r rectangular plates of constant thickness under compressive loads is developed by Timoshenko [17]. A review of this derivation shows that the method is also applicable to plates of variable thickness. In this case, Timoshenko's integrals I_1, I_2 are [17]:

$$I_1 = \iint\limits_{Surface} D\left\{ \left(\frac{\partial^2 \omega}{\partial x^2} + \frac{\partial^2 \omega}{\partial y^2}\right)^2 - 2 \times (1 - \mu) \times \left[\frac{\partial^2 \omega}{\partial x^2} \times \frac{\partial^2 \omega}{\partial y^2} - \left(\frac{\partial^2 \omega}{\partial x \partial y}\right)^2\right] \right\} dx dy \quad (1)$$

$$I_2 = \iint\limits_{Surface} h\left[\frac{\sigma_x}{S} \times \left(\frac{\partial \omega}{\partial x}\right)^2 + \frac{\sigma_y}{S} \times \left(\frac{\partial \omega}{\partial y}\right)^2 + 2 \times \frac{\tau_{xy}}{S} \times \frac{\partial \omega}{\partial x} \times \frac{\partial \omega}{\partial y}\right] dx dy \quad (2)$$

where.
h : is the plate thickness (function of x and y), x, y : is the rectangular coordinates with origin at centre of plate and x-axis in direction of load, and ω : is the lateral deflection of plate.

$$D = \frac{E \times h^3}{12 \times (1 - \mu^2)} \quad (3)$$
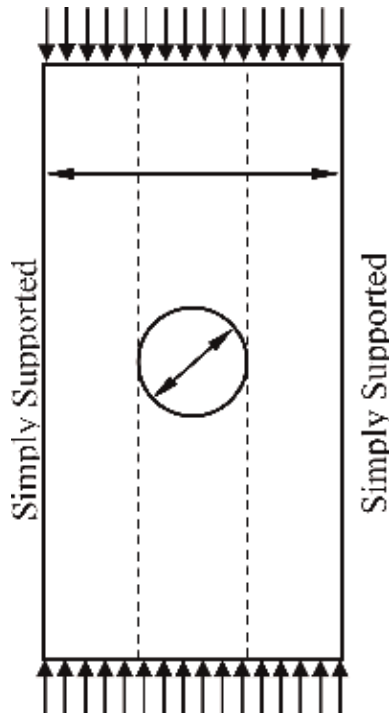
Figure 2.
A simply supported plate subjected to compression.

where D : is the flexural rigidity of plate (function of x and y); $\mu = 0.3$: is the Poisson's ratio; σ_x : is the tensile stress in x direction; σ_y : is the tensile stress in y direction; τ_{xy} : is the shear stress; and S : is the tensile stress in x direction far from hole.

This study investigates the effect of holes on the critical buckling of the web plates of studs subjected to pure compressive load along the length of the plate. The web of the studs is considered to be simply supported along the edges that intersect with the flanges. The buckling analysis is performed using the commercially available finite element software ABAQUS/Standard. In the current research, the general purpose of three-dimensional, stress/displacement, reduced integration with hourglass control, shell element S4R (available in the ABAQUS/Standard element library), is considered to model the plates. S4R is involved in four nodes (quadrilateral), with all six active degrees of freedom per node. S4R allows transverse shear deformation, and the transverse shear becomes very small as the shell thickness decreases.

4.1 Simulation of the behaviour of the steel mesh under dynamic impact loading

A same trend to simulated dynamic behaviour of the steel mesh due the applied dynamic loading was taken into account. Thus, the mesh steel reinforcement sizes 20 mm diameter which they arranged by 100 mm distance centre to centre of the steel bars were tested under free fall of the dropped hammer. The same dropped hammer, which was used in the last section, was considered for the current simulation. It is indicated that a 110 kg hammer was dropped at a velocity of 0.2 m/s on top of the steel reinforcement.

Figures 3 and **4** illustrates the simulated experimental set up which was used to simulate the structural behaviour of the steel mesh under impact loading. It should be noted that steel mesh can play a significant role as a part of the yielding support in a coal mine, as it can mitigate the effect of the destructive released kinetic energy due to a possible coal burst. In the coal mines, it was observed that both rock bolt and cable bolt might be losing the initial bond stiffness at the early stages of the applied dynamic loading due to the failure and separation of the anchored zone in the cable and rock bolt inside embedded coal. The anchorage length in a post-tensioned member and the magnitude of the transverse forces (both tensile and compressive), that act perpendicular to the longitudinal prestressing force, depend on the magnitude of the prestressing force and on the size and position of the
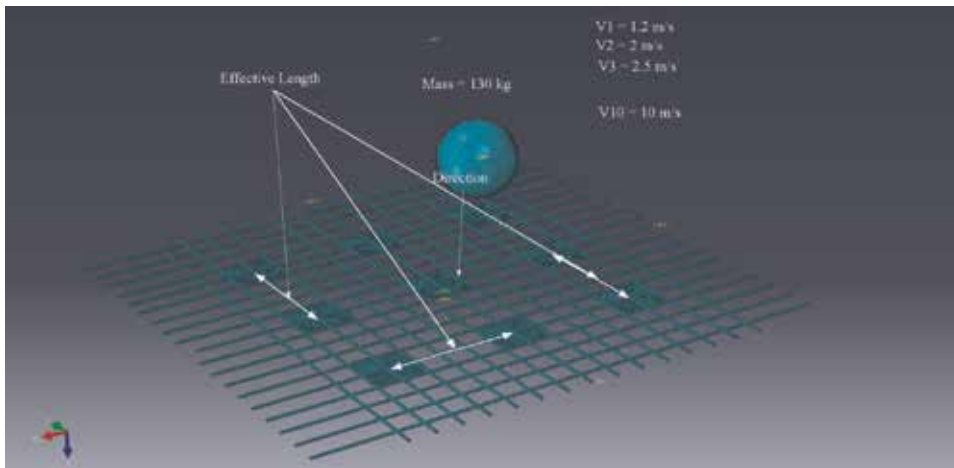
Figure 3.
The testing set up for simulating the behaviour of the steel mesh under impact loading.
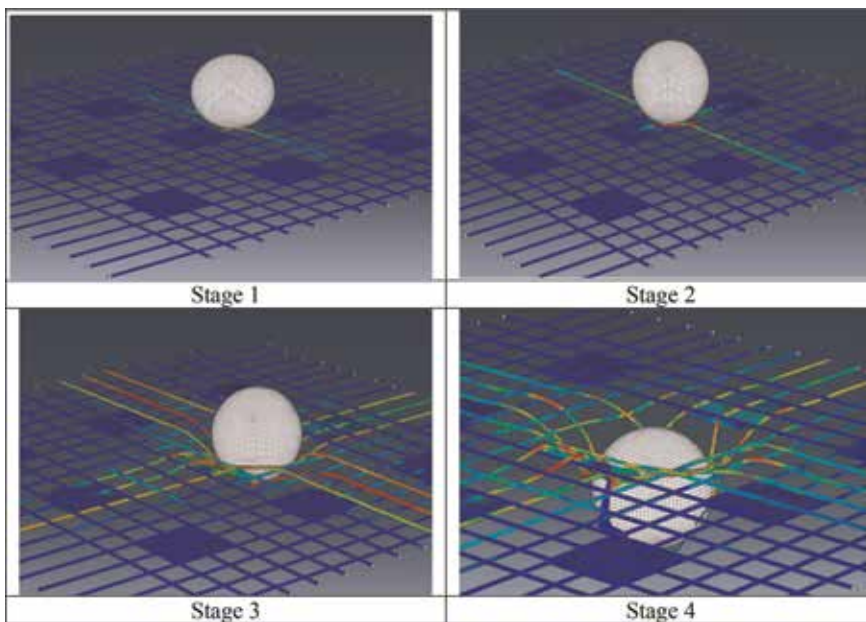
Figure 4.
Simulation of the behaviour of the steel mesh under dynamic impact loading.

anchorage hooks. Both single and multiple anchorages are commonly used in the coal mining. Prestressing force anchors transfer large forces to the coal in concentrated areas. Furthermore, coal is a very brittle material. This can cause localised bearing failure or split open the end of members. Thus, the steel mesh can considerably reduce the effect of the induced dynamic loading due to the coal burst. In the current simulation, the tensile stress for the steel mesh was f_y = *500 MPa* and the ultimate stress for the steel mesh f_u = *700 MPa* was taken into account. The post-failure of the steel mesh which may result in the rupturing of the steel bars was also defined. The ductile damage function was determined to simulate the post-failure of the steel mesh. Also, the rupturing strain $\varepsilon_{\text{rupture}}$ = 0.3% was assumed. Weld properties of the steel mesh can also influence the overall deformation and energy absorption of the yielding support.

4.2 Simulation under dynamic shear loading

After calibrating the numerical models under static loading, the structural behaviour of the simulated models under dynamic loading was also studied. Since preparing the laboratory experiments to simulate the behaviour of cable bolts under dynamic loading is demanding, a validated and novel numerical simulation was developed. In order to simulate the behaviour of the cable bolts under impact loading, a 110 kg mass at velocity of 0.2 m/s was dropped on top of the concrete blocks. **Figure 5** presents the structural behaviour of the cable bolts under impact loading. As illustrated, the momentum energy from the dropped mass would initially be transferred to the concrete surfaces. The transmitted energy due to the impulsive loading will reach the cable bolt. **Figure 5** demonstrates the failure process of the cable bolt under the impact loading starting with the initial deformed shape followed by the brittle shear failure. The computation time was
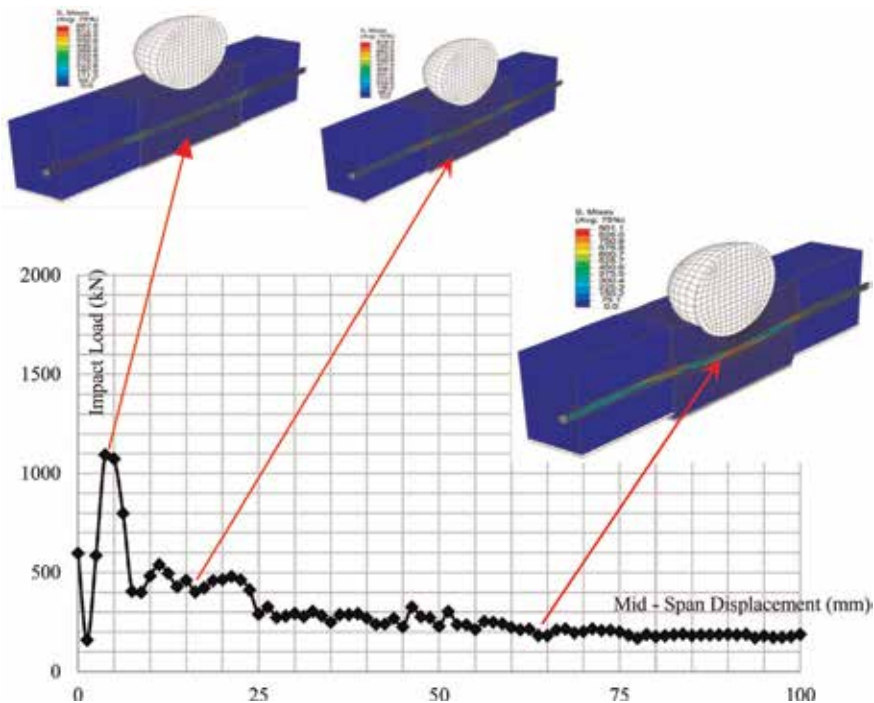
Figure 5.
Cable bolt under impact loading.

around t = 5e-3 seconds, which is very short to simulate the effect of the impulsive loading.

5. Conclusion

A Finite Element model to predict the structural behaviour of cable bolts under both static and dynamic loading was presented. The models were initially calibrated against the experiments available in the literature. By taking the advantage of numerical modelling, some of the localised structural performance of cable bolts under both static and dynamic loading can be observed. By computing the area under curves of the load–displacement curves under both static and dynamic loading, the amount of the absorbed energy in each cable bolt can be estimated. The results indicate that numerical modelling can be used to assess the rock bolt behaviour under dynamic loading for designing the ground support in burst-prone conditions. Numerical techniques can predict an acceptable estimation of the reaction of cable bolts under impact or impulse loading. The most recognised advantages of numerical modelling are that following the initial calibration stage, variety of loading conditions can be modelled and the behaviour of bolts can be studied in greater detail compared with laboratory tests. The current simulations can be taken into account as a cost-effective replacement instead of using drop test facilities. As indicated, drop test facilities are very complicated and expensive. Also, it needs to hire highly skilful technical staffs to calibrate the measurement tools including data acquisition system and the load cell. Subsequently, extracting the induced data after performing the impact test, individually, when it comes to remove the effect of the inertia forces, is one of the significant tasks. In the second section of the current paper, extensive parametrical studies from the developed Finite Element models will be undertaken. The main purpose of doing the following parametrical studies is to determine realistic and technical design guidelines for the combined support against impulsive dynamic loading.

Acknowledgements

Author details

Faham Tahmasebinia[1,2,3]*, Chengguo Zhang[1], Ismet Canbulat[1],
Samad M.E. Sepasgozar[2], Onur Vardar[1], Serkan Saydam[1] and Chen Chen[3]

1 School of Minerals and Energy Resources Engineering, University of New South Wales, Sydney, NSW, Australia

2 Faculty of Built Environment, The University of New South Wales, Sydney, NSW, Australia

3 School of Civil Engineering, The University of Sydney, Sydney, NSW, Australia

*Address all correspondence to: faham.tahmasebinia@sydney.edu.au

IntechOpen

References

[1] Windsor C. Rock reinforcement systems. International Journal of Rock Mechanics and Mining Sciences. 1997; **34**(6):919-951

[2] Stacey T. Review of membrane support mechanisms, loading mechanisms, desired membrance performance, and appropriate test methods. Journal of the Southern African Institute of Mining and Metallurgy. 2001;**101**(7):343-351

[3] Thompson A, Villaescusa E, Windsor C. Ground support terminology and classification: An update. Geotechnical and Geological Engineering. 2012;**30**(3): 553-580

[4] Bjurstrom S. Shear strength of hard rock joints reinforced by grouted untensioned bolts. In: Proc. 3rd Cong. ISRM, Denver. Vol. **2**. 1974. pp. 1194-1199

[5] Haas C. Analysis of rock bolting to prevent shear movement in fractured ground. Mining Engineering. 1981; **33**(6):698-704

[6] Egger P, Zabuski L. Behaviour of rough bolted joints in direct shear tests. In: 7th ISRM Congress. International Society for Rock Mechanics and Rock Engineering; 1991

[7] Ferrero AM. The shear strength of reinforced rock joints. International Journal of Rock Mechanics and Mining Science and Geomechanics Abstracts. 1995;**35**(7):889-905

[8] Hongwei S, Yanyan D, Jing Y. Numerical simulation on bolted rock joint shearing performance. Mining Science and Technology (China). 2010; **20**(3):460-465

[9] Kaiser PK, Cai M. Design of rock support system under rockburst condition. Journal of Rock Mechanics

and Geotechnical Engineering. 2012; **4**(3):215-227

[10] Ansell A. Dynamic testing of steel for a new type of energy absorbing rock bolt. Journal of Constructional Steel Research. 2006;**62**(5):501-512

[11] Plouffe M. Anderson T. Judge K. Rock bolts testing under dynamic conditions at CANMET-MMSL. In: Proceedings 6th international symposium on ground support in mining and civil engineering construction, Cape Town. S. Afr. Inst. Min. Metall. Symposium Series S; 2008

[12] Li CC. A new energy-absorbing bolt for rock support in high stress rock masses. International Journal of Rock Mechanics and Mining Sciences. 2010; **47**(3):396-404

[13] Ghadimi M, Shahriar K, Jalalifar H. A new analytical solution for the displacement of fully grouted rock bolt in rock joints and experimental and numerical verifications. Tunnelling and Underground Space Technology. 2015; **50**:143-151

[14] Cai Y, Esaki T, Jiang Y. An analytical model to predict axial load in grouted rock bolt for soft rock tunnelling. Tunnelling and Underground Space Technology. 2004;**19**(6):607-618

[15] Ma S, Nemcik J, Aziz N. An analytical model of fully grouted rock bolts subjected to tensile load. Construction and Building Materials. 2013;**49**:519-526

[16] Aziz N, et al. Shear strength properties of Hilti plain and indented strand cable bolts. 2014

[17] Tahmasebinia F, et al. Numerical and analytical simulation of the structural behaviour of fully grouted

cable bolts under impulsive loading. International Journal of Mining Science and Technology. 2018;**28**(5):807-811

[18] Levy S, Woolley RM, Kroll WD. Instability of simply supported square plate with reinforced circular hole in edge compression. Journal of Research. 1947;(39):571-577

[19] Kumai T. Elastic stability of the square plate with a central circular hole under edge thrust. In: Proc. Japan Nat. Cong. Appl. Mech. 1951

[20] Schlack A. Elastic stability of pierced square plates. Experimental Mechanics. 1964;**4**(6):167-172

[21] Kawai T, Ohtsubo H. A method of solution for the complicated buckling problems of elastic plates with combined use of Rayleigh-Ritz's procedure in the finite element method. In: Proceedings of the 2nd Air Force Conference on Matrix Methods in Structural Mechanics. Wright-Patterson Air Force Base OH; 1968

[22] Yu W-W, Davis CS. Cold-formed steel members with perforated elements. Journal of the Structural Division. 1973;**99**(10):2061-2077

[23] Timoshenko SP, Gere JM. Theory of Elastic Stability. Courier Corporation; 2009

Criteria for Adequacy Estimation of Mathematical Descriptions of Physical Processes

Yuri Menshikov

Abstract

In this chapter, adequacy estimation criteria for mathematical descriptions in the form of ordinary differential equations were proposed. Adequate mathematical descriptions can increase the objectivity of the results of mathematical modeling for future use. These descriptions make it possibly reasonable to use the results of mathematical modeling to optimize and predict the behavior of physical processes. Interrelations between criteria are considered. The proposed criteria are easily transferred on mathematical descriptions in algebraic form.

Keywords: mathematical simulation, adequate descriptions, criteria of adequacy, applications

1. Introduction

Mathematical modeling (simulation) of physical processes is an important tool for the study of the environment.

Mathematical modeling is a means of studying the real objects, processes, or systems by replacing the real objects on the mathematical models, which are more comfortable to study with the aid of computers.

The mathematical model is an approximate representation of real-world objects, processes, and systems, expressed in mathematical terms. In this case, a significant feature of original are saved from researcher's point of view.

First of all, some definitions and some concepts are given for the convenience of exposition.

A *mathematical model* of a real object will be called as mathematical dependencies and connections between the elements of a mathematical model. These elements are chosen on the basis of the interests of the researcher himself and the ultimate goals of study of the object. Usually, dependencies and relationships have forms of differential equations, integral equations, algebraic connections, etc.

The functions of external influences and external loads that are present in the mathematical model of the object in the form of symbols will be called as models of *external loads.*

The initial conditions, boundary conditions, and other conditions for the mathematical model will be called as *additional conditions*.

The totality of the mathematical model of the object, models of external influences, and additional conditions will be called as a *mathematical description* of the object.

The study of the behavior of the mathematical model of an object under the influence of models of external loads and additional conditions will be called as *mathematical modeling or mathematical simulation*.

The practical significance of the results of mathematical modeling or simulation of physical processes depends on the degree of coincidence of the results of mathematical modeling of the selected mathematical description of the real process with experimental data [1]. Such property of a mathematical description of a physical process is usually called *adequacy*.

1.1 Preliminary definition

A mathematical description will be called as an *adequate mathematical description* (AMD) of the process under study if the results of mathematical modeling (simulation) using this description coincide with experimental data with the accuracy of experimental measurements.

The definition of adequacy will be clarified later for some types of mathematical models.

If the coincidence of the results of mathematical modeling with experiment is bad, then further use of these mathematical descriptions is problematic.

It is note that authors of works on mathematical modeling concern seldom questions of adequacy of the constructed mathematical description of process to real measurements [2–5]. Sometimes, such adequacy is proved by the real facts; sometimes, authors refer to results of other authors; and sometimes, there have not been any arguments.

The considered situation requires formation of some uniform approach to this problem, common methodological approach, general algorithms, and common criteria of estimation of adequacy degree.

- Currently, there are two main approaches to the problem of constructing an adequate mathematical description [1, 6–8]: for a mathematical model with a priori chosen structure and inaccurate parameters, a model of external influence is determined, which together with the mathematical model of the process provide the adequacy condition (coincidence with experiment);

- a model of external loads is given a priori and then parameters of mathematical model or of its structure are selected, in such a way that results of mathematical simulation match up with experiment.

Having a comparison of the results of mathematical modeling with experimental data in definition of adequate mathematical description ensures the objectivity of the results of the synthesis of a mathematical description. In the literature, this approach is called as an identification method: estimation of the parameters of an adequate mathematical description based on the results of measurements of the characteristics of the state of the physical process [9, 10].

Mathematical models of physical processes can be presented as systems of ordinary differential equations, systems of partial differential equations, algebraic relations, integral equations, etc.

It should be noted that in many works, the accuracy of the results of mathematical modeling is several times lower than the accuracy of experimental data.

In the given work, the mathematical models of physical processes described only by the system of the ordinary differential equations will be examined [2, 3]. Such idealization of real processes or dynamic systems is widely used in various areas for the description of control systems [11], as well as of mechanical systems with the

concentrated parameters [5, 12], economic processes [13], biological processes [14], ecological processes [15], etc. In some works with the help of such systems, human emotions are simulated [16].

Many problems investigated in the given work, have place for other types of mathematical models of physical processes, for example, for mathematical models in the form of the partial differential equations.

The chapter proposes several criteria for checking the adequacy of the constructed mathematical descriptions for cases when the mathematical model of the physical process is represented by a system of differential equations.

The author hopes that the offered criteria of adequacy will be useful in a construction of the adequate mathematical descriptions of real physical processes.

2. Criteria of adequacy mathematical description of quantitative type

Consider the specified criteria for mathematical descriptions in the form of a system of differential equations.

For simplicity, we select the physical processes with mathematical models in the form of linear system of ordinary differential equations [17–19]:

$$\dot{x}(t) = Cx(t) + Dz(t), \tag{1}$$

where C, D—matrices with constant coefficients, which are given approximately, $x = (x_1, x_2, \ldots x_n)^T$—vector-function variables, characterized the state of process $((\cdot)^T$—a mark of transposition), $z(t) = (z_1(t), z_2(t), \ldots z_m(t))^T$—vector-function of external load; and $x \in X, z \in Z, X, Z$ are normalized functional spaces.

We assume that state variables $x_i(t), 1 \leq i \leq n$ of system (1) correspond to some real characteristics of process which is under investigation $\tilde{x}_i(t), 1 \leq i \leq n$.

By *mathematical description* of the physical process, we mean the set of the system of Eq. (1), the vector of the external loads functions $z(t) = (z_1(t), z_2(t), \ldots, z_m(t))^T$ and the initial conditions $x(t_0) = x^0$. In other words, a *mathematical description* is a collection of mathematical models, models of external influences, and initial conditions.

The process of solving the system of differential Eq. (1) under the influence of selected models of external loads $z(t) = (z_1(t), z_2(t), \ldots, z_m(t))^T$, taking into account, the initial conditions $x(t_0) = x^0$, is usually called *mathematical modeling* or *mathematical simulation*.

An adequate mathematical description of a physical process of such type with respect to all variables $x_1(t), x_2(t), \ldots, x_n(t)$ of quantitative type will be called as the mathematical description for which the results of mathematical simulation of variables $x_1(t), x_2(t), \ldots, x_n(t)$ coincide with the results of experimental measurements $x_1^{ex}(t), x_2^{ex}(t), \ldots, x_n^{ex}(t)$ of the characteristic $x_1(t), x_2(t), \ldots, x_n(t)$ with the accuracy of the experiments $\delta_1, \delta_2, \ldots, \delta_n$:

$$\left\| x_i(t) - x_i^{ex}(t) \right\|_X \leq \delta_i, 1 \leq i \leq n. \tag{2}$$

In practice, the measurement of the characteristics of state variables is limited to only one or two components. We formulate a refined definition of the adequacy of a mathematical description for the case of a single variable.

An adequate mathematical description of a physical process of such type with respect to the variable $x_k(t), 1 \leq k \leq n$ ($ALMD_{x_k}$) of quantitative type will be called as the mathematical description for which the results of mathematical simulation of

a variable $x_k(t)$ coincide with the results of experimental measurements $x_k^{ex}(t)$ of the characteristic $x_k(t)$ with the accuracy of the experiment δ_k:

$$\left\| x_k(t) - x_k^{ex}(t) \right\|_X \leq \delta_k. \tag{3}$$

For the rest of the variables, coincidence with experiment is not determined. Adequate mathematical descriptions are similarly determined in the case of several measurements of state variables. The metrics of comparison in this case is determined by the objectives of specific studies.

In [12, 20], which were considered before, coincidence with experiment is 10 times below the accuracy of experiment.

The criteria of mathematical description adequacy of quantitative type, which are offered in the given chapter, can be used for other types of mathematical descriptions of physical processes, for example, for mathematical descriptions in the form of the partial differential equations [21]. They have many common features.

It can be shown that there are an infinite set adequate mathematical descriptions for the same physical experiment.

In addition, qualitatively, different physical processes can have adequate mathematical descriptions for the same experiment.

There exist two approaches to problem of construction of adequate mathematical description of quantitative type [22, 23]:

1. Mathematical model of process of type (1) is given a priori with inexact parameters and then the models of external loads were determined for which the results of simulation coincide with experiment [22, 23];

2. Some models of external loads are given a priori and then mathematical model of process of type (1) is chosen for which the results of simulation coincide with experiment [6–8].

Now, we will consider the synthesis of adequate mathematical description of quantitative type in the frame of first approach analyzing the process with the concentrated parameters, for which the motion is described by ordinary differential equations of n-order (1).

We assume that some functions of state $x_1(t), x_2(t), ...x_r(t), r \leq n$ in system (1) are obtained from experiment and presented by graphs. Besides, we suppose that some functions of external loads, for example, $z_1(t), z_2(t), ...z_l(t), l \leq m$ are unknown. According to first approach, it is necessary to develop the construction of such model of external load component, which is characterized by the functions of state $x_1(t), x_2(t), ...x_r(t)$ of mathematical model (1), and will coincide with experimental measurements $\tilde{x}_1(t), \tilde{x}_2(t), ...\tilde{x}_r(t)$ with inaccuracy of initial data. Such mathematical model of process behavior together with obtained model of external load can be considered as *adequate mathematical description of quantitative type* of process.

Such method of obtaining of mathematical models of external loads (functions $z_1(t), z_2(t), ...z_l(t), l \leq m$) is determined in literature as a method of identification [9, 10]. By the way, physical reasons of occurrence of such external loads are not being taken into account. They are only functions, which in combination with mathematical model (1) provide results of modeling, which coincide with experiment with the given accuracy.

Consider an example of a mathematical description that satisfies the criterion of the adequacy of a quantitative type for all variables $x_1(t), x_2(t), ..., x_n(t)$.
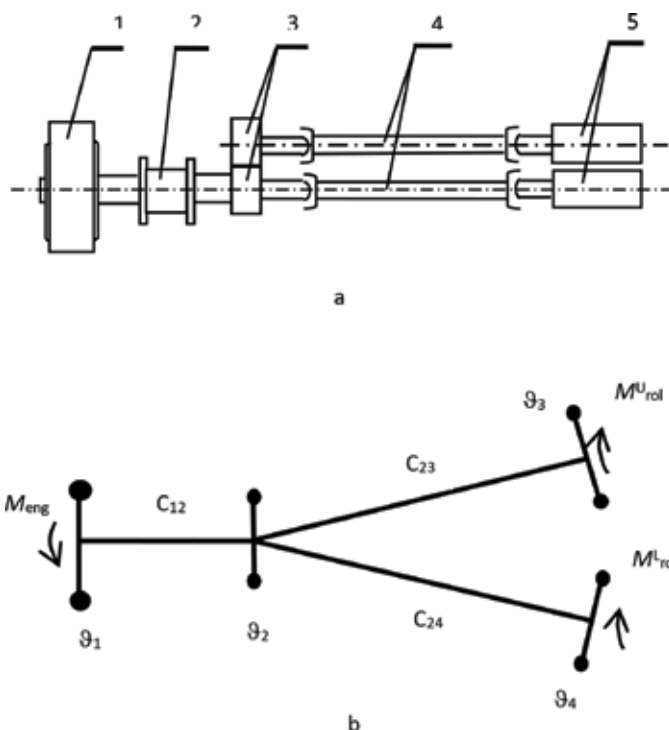
Figure 1.
Kinematic scheme of the main mechanical line of rolling mill.

2.1 Vibrations in the main mechanical line of the rolling mill

Now, we consider in detail, the problem in which the dynamics of the main mechanical lines of rolling mills is investigated [24, 25]. One variant of the kinematic scheme of it is presented in **Figure 1**. (a) where the engine is marked by label (1), the coupling is marked by label (2), gears is marked by label (3), driving shafts is marked by label (4), operational barrels is marked by label (5).

The four-mass model with weightless elastic connections is chosen as mathematical model of dynamic system of the main mechanical line of the rolling mill [24, 25]. The system of vibrations equations is obtained from the Lagrang's equations of second kind:

$$\ddot{M}_{12} + \omega_{12}^2 M_{12} - \frac{c_{12}}{\vartheta_2} M_{23} - \frac{c_{12}}{\vartheta_2} M_{24} = \frac{c_{12}}{\vartheta_1} M_{eng}(t);$$

$$\ddot{M}_{23} + \omega_{23}^2 M_{23} - \frac{c_{23}}{\vartheta_2} M_{12} + \frac{c_{23}}{\vartheta_2} M_{24} = \frac{c_{23}}{\vartheta_3} M^U{}_{rol}(t); \qquad (4)$$

$$\ddot{M}_{24} + \omega_{24}^2 M_{24} - \frac{c_{24}}{\vartheta_2} M_{12} + \frac{c_{24}}{\vartheta_4} M_{23} = \frac{c_{24}}{\vartheta_4} M^L{}_{rol}(t).$$

Here, the following designations were accepted: M_{eng}—moment of engine, ϑ_i—moments of inertia of the concentrated weights, c_{ik}—rigidity of the appropriate elastic connection, M_{rol}^U, M_{rol}^L—moments of technological resistance put to the upper and lower operational barrels accordingly, and M_{ik}—moments of elasticity forces, which are applied to shafts between mass ϑ_i and ϑ_k; $\omega^2{}_{ik} = (\vartheta_i \vartheta_k)^{-1} c_{ik}(\vartheta_i + \vartheta_k)$.

Actually, the constructed mathematical model may correspond to real process and may not. It is necessary to check up correctness of the constructed mathematical model. For this purpose, the data of experiment are used. If the results of mathematical modeling coincide with results of experiment (with accuracy of measurements), then mathematical description of process is considered as adequate to a reality in the quantitative sense. In other words, the mathematical description corresponds to real process.

The information related to the real motion of the main mechanical line of rolling mill was obtained by an experimental way [23, 24, 26]. Such information is being understood as availability of functions $M_{12}(t)$, $M_{23}(t)$, $M_{24}(t)$. The records of functions $M_{12}(t)$, $M_{23}(t)$, $M_{24}(t)$ of a given process are shown in **Figure 2**.

It is obvious, that the results of mathematical modeling of system (4) depend directly on character of change of external loads, which is applied to operational barrels of the rolling mill and external impact of the engine M_{eng}, M_{rol}^U, M_{rol}^L. Sometimes, it is possible to pick up such loadings M_{eng}, M_{rol}^U, M_{rol}^L in which the results of mathematical modeling $M_{12}(t)$, $M_{23}(t)$, $M_{24}(t)$ coincide with experiment (**Figure 2**).

If such choice is possible, then mathematical model (4) combined with the found loads M_{eng}, M_{rol}^U, M_{rol}^L will give adequate mathematical description of real process. It is necessary to note that in many papers analyzing the problem of mathematical modeling with the use of system of a differential Eq. (4) together with functions M_{eng}, M_{rol}^U, M_{rol}^L are determined as mathematical model of process. Coincidence is understood as coincidence with the accuracy of experimental measurements.
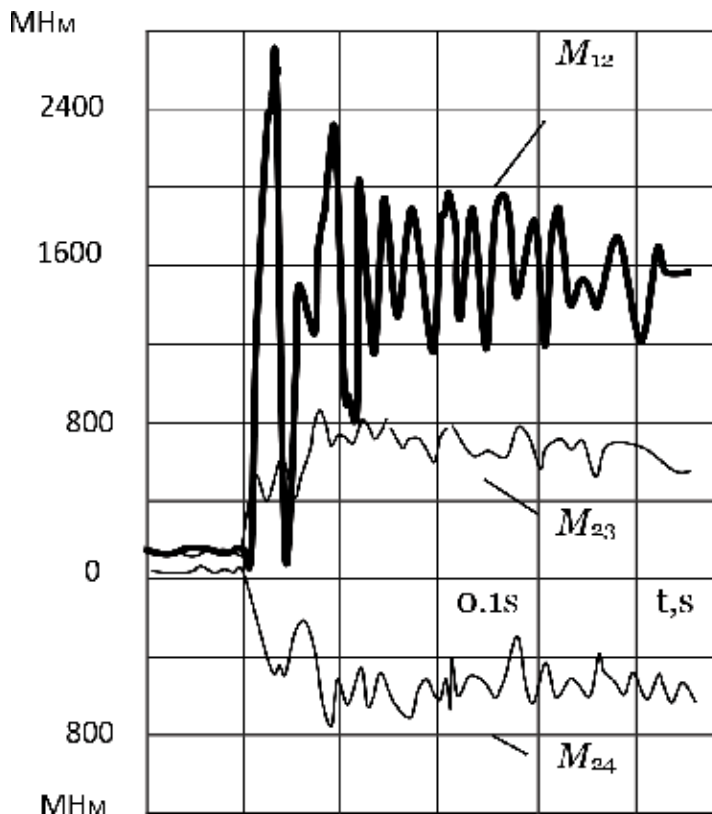
Figure 2.
The records of functions $M_{12}(t)$, $M_{23}(t)$, $M_{24}(t)$.

According to this approach, it is necessary to construct such models of external loads M_{rol}^U, M_{rol}^L on system (4), for which the functions $M_{12}(t), M_{23}(t), M_{24}(t)$ of elastic moments in the links of the model (solution of the system(4)), coincide with the corresponding experimental functions of the moments of elastic forces in the links of the main line of the rolling mill (**Figure 2**).

Consider the construction of an adequate mathematical description within the framework of the first approach. To construct, for example, a model M_{rol}^u, which corresponds to the moment of the external load to the upper work roll, consider the second equation in the system (4). The solution of this equation has the form

$$M_{23}(t) = M_{23}(0) \cos \omega_{23} t + \dot{M}_{23}(0) \omega_{23}^{-1} \sin \omega_{23} t + \frac{c_{23}}{\vartheta_3 \omega_{23}} \int_0^t M_{rol}^u(\tau) \sin \omega_{23}(t - \tau) d\tau$$

$$+ c_{23} (\vartheta_2 \omega_{23})^{-1} \int_0^t [M_{12}(\tau) - M_{24}(\tau)] \sin \omega_{23}(t - \tau) d\tau$$

or

$$\int_0^t \sin \omega_{23}(t - \tau) M_{rol}^u(\tau) d\tau = F(t), \tag{5}$$

where

$$F(t) = \vartheta_3 \omega_{23} (c_{23})^{-1} \{ M_{23}(t) - [M_{23}(0) \cos \omega_{23} t + \dot{M}_{23}(0) \omega_{23}^{-1} \sin \omega_{23} t] \}$$

$$- \vartheta_3 (\vartheta_2)^{-1} \int_0^t [M_{12}(\tau) - M_{24}(\tau)] \sin \omega_{23}(t - \tau) d\tau.$$

We will assume that function $F(t)$ in (5) belongs to the normalized space $L_2[0, T]$ ($[0, T]$ is the period of time at which the function M_{rol}^u is studied) and the solution M_{rol}^u of Eq. (5) belongs to the normalized functional space $C[0, T]$.

Let us rewrite the equation (5) in the more compact form

$$A_p z = u_\delta, \tag{6}$$

where z is the searched element, u_δ is the given element, which belong, respectively, to the functional spaces $C[0, T]$ and $L_2[0, T]$, A_p is the integral operator. In this case, $z = M_{rol}^u(t), u_\delta = F(t)$.

Since the right-hand side $F(t)$ of the integral Eq. (5) is determined from the experiment, it is natural to assume that instead of the exact right-hand side $u_{ex} = F_{ex}(t)$ of the Eq. (6), some approximation of it is given $u_\delta = F(t)$:
$\|u_\delta - u_T\|_{L_2[0,T]} = \|F(t) - F_T(t)\|_{L_2[0,T]} \leq \delta$, δ is given.

The set of possible solutions $Q_\delta \subset C[0, T]$ of Eq. (6) consists of elements that correspond to the equation with given accuracy:

$$Q_\delta = \left\{ z : \|A_p z - u_\delta\|_{L_2[o,T]} \leq \delta \right\}.$$

Each function in the set Q_δ together with the given mathematical model (6) provides an adequate mathematical description of the physical process.

In this case, the problem of identifying model of external load in the rolling mill is considered as the inverse of the synthesis problem [17].
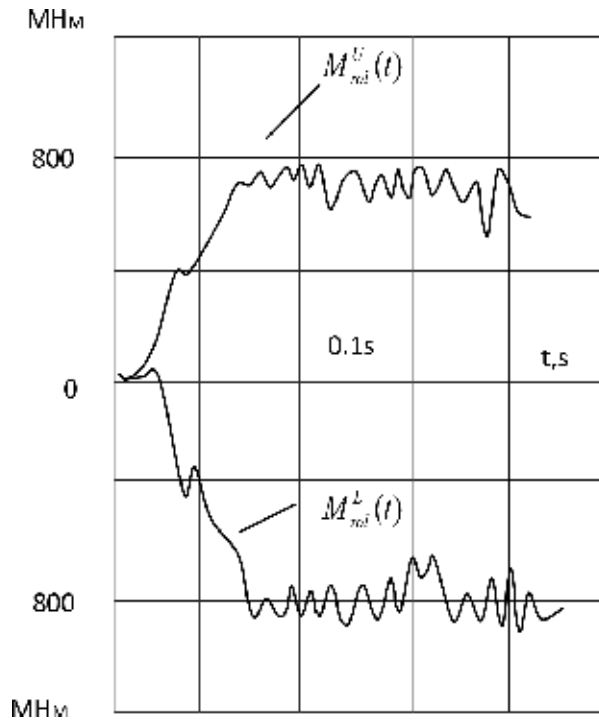
Figure 3.
The results of identification (functions $M_{rol}^{U}(t)$, $M_{rol}^{L}(t)$) for case of rolling that were shown on **Figure 2**.

In this chapter, oscillograms of the moments of the forces of elasticity in the links of the main line of rolling mill 1150, obtained in [24, 25], are used. A copy of this oscillogram is shown in **Figure 2**. The value of T is chosen equal to 0.48 s.

When synthesizing the model of external load on the lower work roll of the state, it is necessary to use the last differential equation in the system (4).

In **Figure 3**, the graphs of the models of external loads on the upper and lower working rolls for rolling case shown on **Figure 2**.

Thus, models of external loads $M_{rol}^{U}(t)$, $M_{rol}^{L}(t)$ were obtained that together with the mathematical model (4) and the initial conditions yield simulation results that coincide with the experimental measurements with the accuracy of the experiment. In other words, the mathematical model (4), models of external loads and initial conditions give an *adequate mathematical description of quantitative type* for all variables of physical process.

Now, we consider another example of astrodynamical processes mathematical description, which has the property of adequacy of quantitative type in only one variable.

Based on theoretical analysis of mathematical vortex model of planetary systems, the analytical expression for planetary distances in the prevailing planetary systems was obtained. These distances are functions of the coordinates of the centers of vortical rings of primary planetary vortex. Comparison of theoretical and real distances planets of the Solar system show their good agreement.

Known in the cosmogonic theories of the solar system, the law of Titsius-Bode (1772) of planetary distances r_n

$$r_n = 0,4 + 0,3 \cdot 2^n \ a.o. \tag{7}$$

is a successful empirical approximation of the real sequence of distances r_n of planets with number n from to Sun. In this case, the first planet (Mercury)

corresponds to the value $n \rightarrow -\infty$, Venus—$n = 0$, the Earth—$n = 1$, etc., and the conditional unformed planet between Mars and Jupiter must be attributed to the value of $n = 3$. Despite the excellent conformance of this law to the average number of planets, the law (7) for the first and distant planets of Neptune and Pluto is not fulfilled [27].

In the twentieth century, some attempts were made [28, 29] to theoretically obtain the law of planetary distances, but in the basis of these theories, the authors had to impose new arbitrary hypotheses. Schmidt [28] introduces a hypothetical function of the distribution of kinetic moments in the masses of the primary nebula, and for the simplest functions it receives a quadratic law, a geometric progression, and others. Kuiper [29] deduces his law on the basis of the theory of tidal stability using the concept of "critical density of Rosh." However, the law it received give the distance between planets, which differ on several orders from the real distance.

Below, based on the mathematical vortical model of the formation of planetary systems [30, 31], the analytical law of planetary distances for any planetary systems was obtained, which gives a good agreement with real distances in the solar system, which has another form compared with (7).

2.2 The theory of planetary vortex

The general picture and the basic relations in the primary vortex explosion, which creates stars and their planetary systems, is constructed in [30] on the basis of a separate exact solution of the Euler hydrodynamic equations for spherical eddy currents [30]. The main physical feature of this axisymmetric spatial flow, called the planetary vortex [30], is the presence of a vortex dipole in the center of the vortex dipole, which flows through a moving, twisted stream of outer space, and the interaction of these motions generates vortical flow of a planetary vortex [30].

Using the method of integrating the complete nonlinear system of Euler's hydrodynamic equations was introduced and flow functions $\Psi(y, \theta)$ constructed. The function of flow in spherical coordinates (r, θ, φ) [30] is constructed.

The planetary vortex described above as a complicated vortex flow is the initial stage of the formation of a star planetary system from the primary nebula that has fallen into the vortex region. Further prolonged evolution of this vortex to the state of the planetary system is characterized by a variety of complex physical processes such as: collision, accretion, accumulation of massive bodies, and their gravitation; the formation of a massive star and its light and gravitational action; mutual gravitational and resonant influence of system structures, etc. [27].

Since the forces of gravitation, collision, and others acting between parts of a single vortex are internal, they do not change its integral physical invariants.

In [30, 31], the modern planetary distances were calculated and they are shown in the graphs (**Figure 4**). As we can see, the theoretical curve in the entire range of distances is almost equidistant from the curve of real distributions of distances in the solar system with deviations in both directions of the order of 20%.

Finally, the technique developed here for the calculation of the primary vortex parameters can be applied in the reverse direction to determine according to the data of several open planets of the main parameter of the planetary system and the establishment of the method of work [38] of the complete structure of new exoplanetary systems: the number of vortex planets, their distances from the star, angular velocities, etc. This will give astronomers-observers reasoned data for the search for new, yet open exoplanets in stellar planetary systems, which have already opened 2–6 planets [32, 33].

Thus, the mathematical model of the process of formation of planetary systems, which describes interplanetary distances well, is constructed.
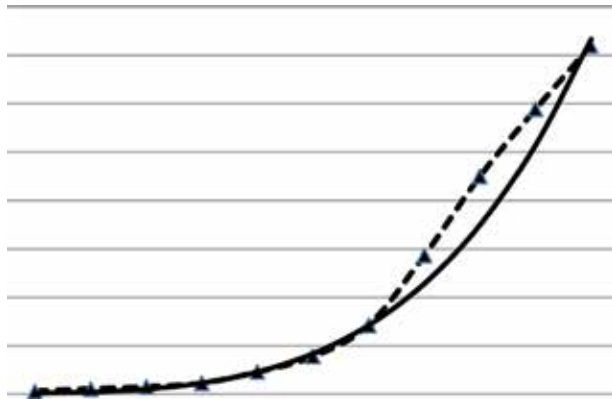
Figure 4.
Planetary distances in the solar system as functions of planetary numbers.

The development of this mathematical model does not take into account important physical factors that have a significant effect on the behavior of interplanetary matter. To such factors, it is necessary to attribute, first of all, gravitational interaction and heat flows. Because of this, one should not expect a good coincidence of the real characteristics of the physical process with the results of mathematical modeling. This situation occurs when the criterion of adequacy of the qualitative type is not met (see Section 2). Consequently, the coincidence of the results of mathematical modeling (with the adequate mathematical description constructed only one or two of the system's variables) with all the main characteristics of the physical process is an exception, as a rule, and it can take place only if the adequacy of a quality type is performed.

3. Criteria of adequacy of mathematical description of qualitative type

We will consider what prospects of adequate descriptions are valid for further use and what goals should be selected as the creation of adequate mathematical descriptions.

It will be useful to address to classical works in this area. In work [34], the following statement was done: "...the imitation modeling is the creation of experimental and applied methodology which aimed at the use of it for a prediction of the future behavior of system."

So, the adequate mathematical descriptions are intended for the forecast of behavior of real process at first. It is possible with the aid of adequate mathematical modeling to predict behavior of real process in new conditions of operation. For example, it is possible to test more intensive mode of operations of the real machine without risk of its destruction. Such tool (adequate mathematical description) allows determining the optimum parameters of real process.

Let us now consider the conditions under which it is possible to further use adequate mathematical descriptions for "...a prediction of the future behavior of system."

Obviously, the structure of system (1), its parameters, and the specific type of external influences are determined by the properties of a real physical process.

Let the selected structure of the mathematical model of the physical process include parameters $p = (p_1, p_2, ..., p_k)^T$ (e.g., the mass of the elements, the stiffness of the elastic elements, etc.), which are reflecting the actual physical characteristics.

The structure of the mathematical model also includes dependencies that reflected real physical patterns and dependencies of the process under study.

For the purpose of further substantiated use of mathematical descriptions, it is necessary to require that there is a one-to-one correspondence between the components of the vector parameter p of mathematical description and the actual physical elements. In addition, it is necessary to require that the interconnections between the parameters of a mathematical model comply with the physical laws of the process being studied, and the main external loads had been included. This important correspondence will be called the *main correspondence* (MC). The execution of the MC believed the fulfillment of the criterion of *adequacy of the qualitative type*. In other words, a mathematical description of a physical process satisfies the criterion of adequacy of a qualitative type if the main correspondence is fulfilled.

An additional requirement for the implementation of the MC is explained firstly by the fact that the quantitative agreement of the results of mathematical modeling with a specific experiment is possible for mathematical descriptions of qualitatively different physical processes due to the selection of parameters of mathematical descriptions.

The implementation of the MC leads to the fact that the models of external influences obtained by the method of identification will correspond to the real external influences on the physical process. At least, these models will not contradict the physical meaning. If we return to the example of the synthesis of an adequate mathematical description of the process of mechanical oscillations in the main line of the rolling mill, then it can be argued that the MC is being executed. By virtue of this, the obtained models of external influences have a reasonable physical interpretation (do not contradict the physical meaning). The external load smoothly increases from zero to a steady-state value (see **Figure 3**).

When fulfilling the adequacy of a mathematical description of a qualitative type, it becomes possible to argue that a mathematical description that satisfies two criteria of adequacy will retain its useful properties for other experiments in the future under small changes in the conditions of the physical process. In other words, this description can be used for "a prediction of the future behavior of system." An example of such a successful application could be further mathematical modeling using an adequate mathematical description for the rolling mill [23].

In the second example, given in Section 1, the main correspondence is not fulfilled, and therefore, the application of the obtained results in the new conditions will not be justified.

The algorithm for constructing an adequate mathematical description of a qualitative type cannot be formalized, as in the case of the adequacy of a mathematical description of a quantitative type. The process of constructing such a description mainly depends on subjective factors, such as the scientific tasks of studying the physical process using mathematical modeling methods.

In some cases, it is impossible to perform a check of mathematical description adequacy of a quantitative type due to lack of experimental data in principle. Let us give an example of a mathematical description that satisfies only the criterion of adequacy of a qualitative type.

An important and relatively new field of applications of methods of mathematical modeling is a tectonic processes study [35]. This work presents a complete algorithm required for the successful application of mathematical modeling methods of operations, which does not include the verification operation. Consider this algorithm in more detail.

It is widely known that earthquakes predicting is challenging and unsolved still (but it can be happen in future). Even where earthquakes have unambiguously

occurred within the parameters of a prediction, statistical analysis has generally shown these to be not better than lucky guesses. Now, there are hundreds of well-known earthquakes precursors and a number of theories to explain their origin. However, the problem of earthquake prediction in many of its aspects still remains open.

Utsu studied theoretically the relation between the size of aftershock activity and the magnitude of the main shock [36]. Independence of the occurrence of main shocks has been assumed in many models, some chapters discuss the migration of large earthquakes and casual relationship between seismic activities in different geophysical regions. Trigger models assume a series of primary events (main shocks) distributed completely random in time. Each of these primary events may generate secondary series of events. Epidemic-type model can be considered as birth and death process.

Utsu proposes a new model that takes into account the influence of strain solitary waves as a "trigger" of some shocks and appropriate methods of forecasting. Authors analyze the 2011 Japan earthquake. These studies show that solitary waves can be generated as aftershocks hypocenters at the Moho surface.

Significant amount of works have been devoted to research of solitons in solids. For example, considering structural-phenomenological approach one distinguishes damaged environment with microstructure, Kosser's continuum with limited traffic, Leru's continuum, environment with deformities [37], grainy environment, which has the soliton solutions of motion equations. It is known that the pulse perturbations in rocks are different from seismic waves of harmonic type.

Some researchers [36–38] have considered generalizations of the traveling wave solutions. The necessary and sufficient conditions for the existence of appropriate solutions were obtained.

Let us consider an anisotropic elastic medium. By [39], it follows that relations between stress and strain in Hooke's law contain 21 free coefficients. The system of motion equations in this case has the form:

$$\rho \frac{\partial^2 u}{\partial t^2} = ((c_{11}, c_{66}, c_{55}, 2c_{16}, 2c_{15}, 2c_{56}), \Theta u)$$
$$+ ((c_{16}, c_{26}, c_{45}, c_{12} + c_{66}, c_{14} + c_6, c_{46} + c_{25}), \Theta v) \tag{8}$$
$$+ ((c_{15}, c_{46}, c_{35}, c_{14} + c_{56}, c_{13} + c_{55}, c_{36} + c_{45}), \Theta w),$$

$$\rho \frac{\partial^2 v}{\partial t^2} = ((c_{16}, c_{26}, c_{45}, c_{66} + c_{12}, c_{56} + c_{14}, c_{25} + c_{46}), \Theta u)$$
$$+ ((c_{66}, c_{22}, c_{44}, 2c_{26}, 2c_{46}, 2c_{24}), \Theta v) \tag{9}$$
$$+ ((c_{56}, c_{24}, c_{34}, c_{46} + c_{25}, c_{36} + c_{45}, c_{23} + c_{44}), \Theta w),$$

$$\rho \frac{\partial^2 w}{\partial t^2} = ((c_{15}, c_{46}, c_{35}, c_{14} + c_{56}, c_{13} + c_{55}, c_{45} + c_{36}), \Theta u)$$
$$+ ((c_{56}, c_{24}, c_{34}, c_{46} + c_{25}, c_{45} + c_{36}, c_{23} + c_{44}), \Theta v) \tag{10}$$
$$+ ((c_{55}, c_{44}, c_{33}, 2c_{45}, 2c_{35}, 2c_{34}), \Theta w),$$

where u, v, and w are the displacements along the respective axes of a Cartesian coordinate system, $\rho(x_1, x_2, x_3)$ is the density,
$\Theta = \left(\frac{\partial^2}{\partial x_1^2}, \frac{\partial^2}{\partial x_2^2}, \frac{\partial^2}{\partial x_3^2}, \frac{\partial^2}{\partial x_2 \partial x_1}, \frac{\partial^2}{\partial x_3 \partial x_1}, \frac{\partial^2}{\partial x_2 \partial x_3} \right)$, $C = \left\| c_{ij} \right\|_{i,j=\overline{1,6}}$ is matrix of elastic constants.

There, the following concept was introduced. Authors found the solutions of (8)–(10) as follows:

$$(u, v, w)^T = (\psi_u(t), \psi_v(t), \psi_w(t))^T W(x, y, z, t), \tag{11}$$

where $W(.) = \exp\left(-\frac{g(x - \tilde{x}(t))}{\varepsilon_1} - \frac{g(y - \tilde{y}(t))}{\varepsilon_2} - \frac{g(z - \tilde{z}(t))}{\varepsilon_3}\right)$, $g(.) \in G$ is the class of positive-definite, unimodal, twice continuously differentiated functions with a minimum at zero, and for which the second derivative is not a constant, $\psi_u(t)$, $\psi_v(t)$, $\psi_w(t)$ are the functions which determined the amplitude of the relevant perturbations, ε_1, ε_2, ε_3 are constants which determined the localization perturbations, $\tilde{x}(t)$, $\tilde{y}(t)$, $\tilde{z}(t)$ are the functions which determined the trajectory of solitary waves.

In [39], authors got the necessary and sufficient conditions of existent solutions of the system (8)–(10) in the form (11). In [40], the various crystal systems for the existence of the appropriate type of motion equations solutions are studied.

The main hypothesis of method of earthquakes forecast is that a single shock causes the appearance of one or more solitary waves that move from the hypocenter of the earthquake. Each wave passing through the zone of accumulation of seismic energy, causing a new earthquake can in turn generate new solitons. The method of prediction involves the separation from the total population of earthquake subsequences caused by the same soliton and the construction of a hypothetical trajectory of the solitons. Knowing the distance between individual impulses along the trajectory of the soliton can estimate its speed. Knowing some point of its trajectory, it is possible to make an assessment of the trajectory. With the rate and trajectory of each soliton, one can estimate its position at any time. Having information about the position of the soliton at some time can determine the "soliton component" of shock probability at this time.

As initial data, we consider a sequence of the form: (x_1, t_1, μ_1), (x_2, t_2, μ_2), ..., (x_k, t_k, μ_k), where $x_1, x_2, ..., x_k$ are earthquake hypocenters, $\mu_1, \mu_2, ..., \mu_k$ are magnitudes, and $t_1, t_2, ..., t_k$ are times of shocks.

Let a trajectory of the soliton be described parametrically: $x(t) = (x_1(t), x_2(t))$, $v(t)$ is speed. Then, we have:

$$v(t) = \frac{dx(t)}{dt} = \sqrt{(x_1{}'(t))^2 + (x_2{}'(t))^2},$$

$$\int_{t_i}^{t_{i+1}} v(t)dt = \int_{t_i}^{t_{i+1}} \sqrt{(x_1{}'(t))^2 + (x_2{}'(t))^2}dt = l(x(t_i), x(t_{i+1})),$$

$$v_i = \frac{l(x(t_i), x(t_{i+1}))}{t_{i+1} - t_i} = \int_{t_i}^{t_{i+1}} v(t)dt / (t_{i+1} - t_i),$$

where $l(x(t_i), x(t_{i+1})$ is the length of the curve corresponding to time interval (t_i, t_{i+1}).

Assume that the speed of the soliton is monotone—decreasing function. If the motion occur in the region of constant density, the ratio will be implemented: $v_1 = v_2 = ... = v_{k-1}$. In the field of variable density: $v_1 > v_2 > ... > v_{k-1}$.

Then, we consider the approximate speed $\tilde{v}_1 = \frac{x_2 - x_1}{t_2 - t_1}$, $\tilde{v}_2 = \frac{x_3 - x_2}{t_3 - t_2}$, ..., $\tilde{v}_{k-1} = \frac{x_k - x_{k-1}}{t_k - t_{k-1}}$.

If a density is constant, then $\tilde{v}_1 + \varepsilon_1 = \tilde{v}_2 + \varepsilon_2 = ...\tilde{v}_{k-1} + \varepsilon_{k-1}$, where $\varepsilon_1, \varepsilon_2, ...\varepsilon_{k-1}$ is the curvature parameters. If a density is variable, then:

$\tilde{v}_1 > \tilde{v}_2 > ... > \tilde{v}_{k-1}$. This is criteria for the identification a subsequence of individual solitons trajectory.

In **Figure 5**, the results of seismic process analysis that occurred on the Japanese islands for 3 days before the earthquake of magnitude 8.9 (occurred on March 11, 2011) are shown. Here, the numbers from 0 to 12 mark epicenters of the foreshock, the epicenter of the main shock indicates maximum circle radius (it is near to the epicenter of the foreshock number 1). Curves and straight lines marked the soliton trajectory, which are calculated using a special software. The calculations take into account the hypothetical rate of the solitary waves and their possible reflection from the areas with a high density of rocks.

As you can see, the foreshock is arranged so that a large number of possible waves pass through the region, where there was a maximum magnitude shock. Clearly, traced kind of a soliton with a focusing effect is at the point where there was the main shock.

Thus, here it proposed the mathematical model of the process of earthquake sequences, taking into account the impact of slow solitary wave soliton type as a "trigger" to some shocks. The proposed theory allows us to construct forecasts when geophysics seismic process is similar to that which occurred on Japanese islands in 2011.

The considered example of a mathematical description cannot be checked for the adequacy of a quantitative type due to objective reasons. But this description meets the criterion of adequacy of the qualitative type and so the results of mathematical modeling do not contradict the physical meaning.

Further, consider an example of a mathematical description, the adequacy of which cannot be fundamentally assessed.

Methods of mathematical modeling penetrate recently into many nontraditional areas of human activity such as the study and modeling of emotions [16]. Let us consider in more detail the peculiarities of the application of methods of mathematical modeling in this field.
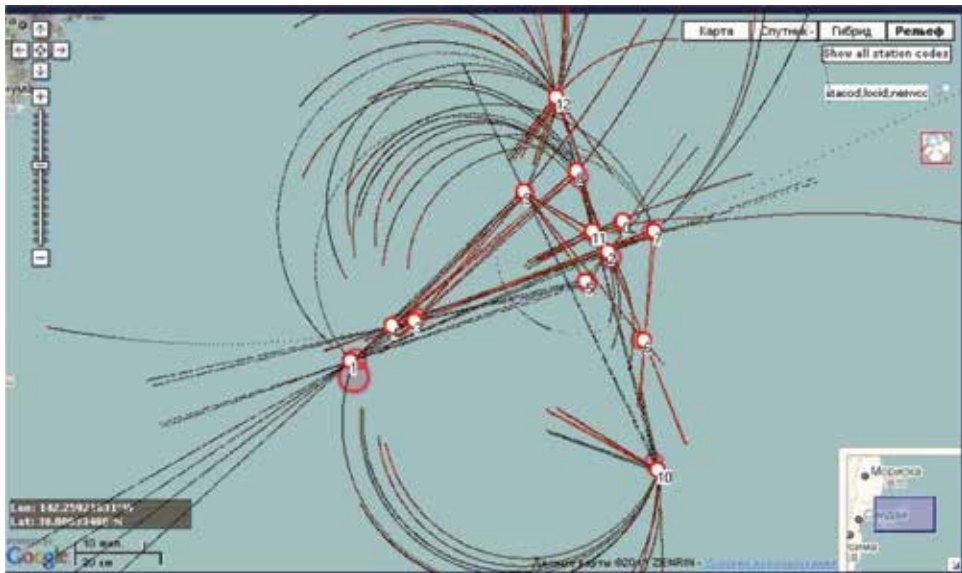

Figure 5.
Results of seismic process analysis that occurred on the Japanese islands on March 11, 2011 for 3 days before the earthquake of magnitude 8.9.

The mathematician Rinaldi investigated as first Petrarch's emotional cycle and established an ODE model, starting point for the investigations in two directions: mapping the mathematical model to a suitable modeling concept, and trying to extend the model for love dynamics in modern times.

A control-oriented approach observes emotions and inspiration as states fading over time-behaving like a transfer function approaching a steady state. This observation suggests a modeling approach by transfer functions. Both model approaches allow an easy extension to modern times.

In literature, two special contributions can be found:

- Love affairs and differential equations by Strogatz [41], —harmonic oscillators making reference to Romeo and Juliet;

- Laura and Petrarch: an Intriguing Case of Cyclical Love Dynamics by Rinaldi [42]—presenting a nonlinear ODE with cyclic solutions.

Both contributions start directly with nonlinear oscillations, observing a certain historic emotional behavior of prominent couples. Laura group at Vienna University of Technology tries to consider general modeling concepts for emotional relations, which cover or coincide with Petrarch's emotional cycle, in case of appropriate parameterization.

Following a suggestion of Strogatz [41] here examines a sequence of dynamical models involving coupled ordinary differential equations describing the time-variation of the love or hate displayed by individuals in a romantic relationship. The models start with a linear system of two individuals and advance to love triangles, and finally to include the effect of nonlinearities, which are shown to produce chaos.

An obvious difficulty in any model of love is defining what is meant by love and quantifying it in some meaningful way.

3.1 Simple linear model

Strogatz [40] considers a love affair between Romeo and Juliet, where $R(t)$ is Romeo's love (or hate if negative) for Juliet at time t and $J(t)$ is Juliet's love for Romeo.

The simplest model is linear with

$$\frac{dR(t)}{dt} = a\,R(t) + b\,J(t),$$

$$\frac{dJ(t)}{dt} = c\,R(t) + d\,J(t), \tag{12}$$

where a and b specify Romeo's "romantic style," and c and ad specify Juliet's style. The parameter a describes the extent to which Romeo is encouraged by his own feelings, and b is the extent to which he is encouraged by Juliet's feelings. The resulting dynamics are two-dimensional, governed by the initial conditions and the four parameters, which may be positive or negative.

A similar linear model has been proposed by Rinaldi [42] in which a constant term is added to each of the derivatives in (12) to account for the appeal (or repulsion if negative) that each partner presents to the other in the absence of other feelings. Such a model is more realistic since it allows feelings to grow from a state of indifference and provides an equilibrium not characterized by complete apathy. However, it does so at the expense of introducing two additional parameters. While the existence of a non-apathetic equilibrium may be very important to the

individuals involved, it does not alter the dynamics other than to move the origin of the RJ state space.

Romeo can exhibit one of four romantic styles depending on the signs of a and b, with names adapted from those suggested by Strogatz [40] and his students:

1. Eager beaver: $a > 0$, $b > 0$ (Romeo is encouraged by his own feelings as well as Juliet's).

2. Narcissistic nerd: $a > 0$, $b < 0$ (Romeo wants more of what he feels but retreats from Juliet's feelings).

3. Cautious (or secure) lover: $a < 0$, $b > 0$ (Romeo retreats from his own feelings but is encouraged by Juliet's).

4. Hermit: $a < 0$, $b < 0$ (Romeo retreats from his own feelings as well as Juliet's).

Note that for the mathematical description (12), the criterion of the adequacy of the quantitative type and the criterion of the adequacy of the qualitative type cannot be checked due to the specificity of the process under study. Therefore, the further use of the results of mathematical modeling is unreasonable. However, there are no obstacles to nontraditional interpretations of the results of mathematical modeling of emotional processes.

4. Conclusion

The proposed adequacy criteria for mathematical descriptions in the form of ordinary differential equations make it possible to reasonably use the results of mathematical modeling to optimize and predict the behavior of physical processes.

The proposed criteria are easily transferred on mathematical descriptions in algebraic form [43].

Criteria for the adequacy of mathematical descriptions in the form of partial differential equations are currently missing in the literature. However, some criteria for the adequacy of mathematical descriptions can be transferred to the specified descriptions. For example, the criterion of adequacy of the qualitative type can be transferred almost unchanged.

Author details

Yuri Menshikov
University of Dnipro, Dnipro, Ukraine

*Address all correspondence to: menshikov2003@list.ru

IntechOpen

References

[1] Menshikov Y. About adequacy of mathematical modeling results. In: Proceedings of the International Conference "Simulation-2008"; Kiev, Ukraine. 2008. pp. 119-124

[2] Soeiro N et al. Experimental measurements and numerical modelling of vibroacoustics behaviour of a vehicle gearbox. In: Proceedings of the International Eleventh International Congress on Sound and Vibration; St. Petersburg, Russia. 2004. pp. 2821-2828

[3] Alexik M. Modelling and identification of eye-hand dynamics. Simulation Practice and Theory. 2000;**8**: 25-38. ISSN 0928-48693

[4] Pop O, Valle V, Cottron M. Numerical and experimental study of the plastic in the vicinity of the crack tip by the optical caustics method. In: Proceedings of XXI International Congress of Theoretical and Applied Mechanics; Warsaw, Poland. 2004. 24 p

[5] Lino P, Maione B. Multi-Domain and Control in Mechatronics: The Case of Common Rail Injection Systems. Vienna, Austria: In-Teh is Croatian Branch of I-Tech and Publishing KG; 2008. pp. 234-245. DOI: 10.5772/5825

[6] Stepashko V. Method of critical dispersions as analytical tools of theory of inductive modeling. Problems of Control and Information. 2008;**40**(2): 4-22. DOI: 10.1615/JAutomatInfScien. v40.i3.20

[7] Gubarev V, Method of iterative identification of multidimensional systems by uncertain data. Part I. Theoretical aspects, Problems of Control and Information. 2008;**38**(9):8-26. DOI: 10.1615/J Automat Inf Scien.v38.i9.20

[8] Gukov O. Algorithms of iterative identification of many-dimensional systems. In: Proceedings of XV International Conference on Authomatical Control, Authomatics. Odessa, Ukraine: ONMA; 2008. pp. 774-777

[9] Ikeda S, Migamoto S, Sawaragi Y. Regularization method for identification of distributed systems. In: Proceedings of IY a Symposium IFAC on Identification and Evaluation of Parameters of Systems. Vol. 3. Tbilisi, Moscow: USSR, Preprint; 1976. pp. 153-162

[10] Gelfandbein J, Kolosov L. Retrospective identification of perturbations and interferences. Science; Moscow. 1972. 232 p

[11] Krasovskij N. Theory of motion control. Science; Moscow. 1968. 476 p

[12] Sarmar I, Malik A. Modeling, analysis and simulation of a pan tilt platform based on linear and nonlinear systems. In: Proceedings of International Conference IEEE/ASME MESA, China. 2008. pp. 147-152

[13] De la Fuente A. Mathematical Methods and Models for Economists. London: Cambridge University Press; 2000. ISBN: 0521585295, 0521585120, 9780521585293

[14] Tillack J et al. Software framework for modeling and simulation of dynamic metabolic and isotopic systems. In: Proceedings of 6-th International Vienna Conference on Mathematical Modelling, Vienna, Full Papers CD Volume. 2009. pp. 769-778

[15] Perminov V. Mathematical modelling of large forest fires initiation. In: Proceedings of 6-th International Vienna Conference on Mathematical Modelling, Vienna, Full Papers CD Volume. 2009. pp. 1165-1172

[16] Breitenecker F et al. Laura and Petrarca—True emotions vs. modelled

emotions. In: Proceedings of 6-th International Vienna Conference on Mathematical Modelling, Vienna, Full Papers CD Volume, Vienna Univ. of Technology. 2009. pp. 46-69. ISBM 978-3-901608-35-3

[17] Menshikov YL. Synthesis of adequate mathematical description as solution of special inverse problems. European Joumal of Mathematical Sciences. 2013;**2**(3):256-271. DOI: 10.4236/jmp.2015.614217

[18] Bogaevski V, Povzner A. Equations in partial derivatives. In: Algebraic Methods in Nonlinear Perturbation Theory. Applied Mathematical Sciences. Vol. 88. New York, NY: Springer; 1991. DOI: 10.1007/978-1-4612-4438-7_5

[19] Kalman R. Mathematical linear description of dynamical systems. SIAM Journal on Control and Optimization. 1963;**1**(2):152-192. Available from: h ttp://www.siam.org/journals/ojsa.php

[20] Schulmeister K, Kozek M. Modelling of lateral dynamics for an endless metal process belt. In: Proceedings of 6-th International Vienna Conference on Mathematical Modelling, Vienna, full Papers CD Volume. 2009. pp. 1965-1973

[21] Porter W. Modern Foundations of Systems Engineering. New York/ London: The Macmillan Company/Collier-Macmillan Limited; 1970. DOI: 10.1126/ science.157.3792.1030-a

[22] Menshikov Y. Synthesis of adequate mathematical description for dynamical systems. In: Proceedings of International Conference on Mathematical Modelling in Applied Sciences. ICMMAS'2017; 24-28 July 2017. St. Petersburg-Russia: SPbPU; 2017. 2 p

[23] Menshikov Y, Polyakov N. Handbook of Identification of Models of External Influences. Dnepropetrovsk,

Ukraine: Science and Osvita; 2009. 188 p. ISBN 978-966-8736-05-6

[24] Menshikov Y. Identification of moment of technological resistance on rolling. Journal of Differential Equations and their Applications in Physics. 1976; **1**:22-28

[25] Menshikov Y, Yah G. Synthesis of the moment of technological resistance on a rolling mill. Journal of Dynamics and Strength of Heavy Machines. 1983; 7:33-39

[26] Bondar V et al. Some results of an experimental study of the main line of blooming 1150. Journal of Dynamic Strength and Stability of Elements of Large Machines. 1973:3-17

[27] Alfven H. The structure and evolutionary history of the solar system. Astrophysics and Space Science. 1973; **21**(1):117-176. DOI: 10.1007/BF00642197

[28] Schmidt O. The origin of the earth and planets. Science (Moscow). 1962. 279 p

[29] Kuiper GP. On the origin of the solar system. In: Hynek JA, editor. Article in Astrophysics. New York, Toronto, London: McGraw-Hill; 1951

[30] Perehrest V. The planetary vortex and the Laplace and Weizsäcker hypotheses. Visnik Dnipropetr University. Mechanics. 2009;**17**(5): 113-124

[31] Perehrest V. About the structure of planetary viiors and laws of law and wrapping. Visnik Dnipropetr University. Mechanics. 2010;**18**(14): 110–118

[32] NASA "Sun Fact Sheet". Available from: http://nssds.gfsc.nasa.gov/plantary 2009

[33] Available from: http://exoplanets. org/exotable/exotable.html

[34] Shanon R. Systems Simulation—The Art and Science. New Jersey: Prentice-Hall, Inc., Englewood Cliffs; 1975. ISBN 10.0138818398

[35] Vere-Jones D. Some models and procedures for space-time point processes. Environmental and Ecological Statistics. 2008;**16**(2): 173-195. DOI: 10.1007/s10651-007-0086-0

[36] Utsu T. Representation and analysis of the earthquake size distribution: A historical review and some new approaches, Mechanics. 2010;**18**(14): 110-118. DOI: 10.1007/s000240050276

[37] Erofeev V. Wave Processes in Solids with Microstructure. Moscow: Moscow University; 1999. 255 p

[38] Turbal Y. The trajectories of self-reinforsing solitary wave in the gas disc of galaxies. In: Proceedings of the 3rd International Conference on Nonlinear Dynamic. 2010. pp. 112-118

[39] Turbal Y. Necessary and sufficient conditions for the existence of the motion equations solutions for anisotropic elastic bodies in the form of solitary waves. Problems of Applied Mathematics and Mathematical Modeling. 2012;**12**:78-86. DOI: 10.1155/2013/537520

[40] Turbal Y. Elastic anisotropy from the standpoint of the solitary waves existence like δ-Soliton. Problems of Mechanics. 2012;**18**:76-90

[41] Strogatz SH. Love affairs and differential equations. Mathematics Magazine. 1988;**61**:35. DOI: 10.2307/2690328

[42] Rinaldi S. Laura and Petrarch: An intriguing case of cyclical love dynamics. SIAM Journal on Applied Mathematics. 1998;**58**(4):1205-1221. DOI: 10.1007/s11071-015-2351-3

[43] Menshikov Y. Features of parameters identification of algebraic mathematical models. International Journal of Engineering and Innovative Technology. 2014;**4**(5):5. ISSN: 2277-3754

Chapter 5

Power Flow Analysis

Mohammed Albadi

Abstract

Power flow, or load flow, is widely used in power system operation and planning. The power flow model of a power system is built using the relevant network, load, and generation data. Outputs of the power flow model include voltages at different buses, line flows in the network, and system losses. These outputs are obtained by solving nodal power balance equations. Since these equations are nonlinear, iterative techniques such as the Newton-Raphson, the Gauss-Seidel, and the fast-decoupled methods are commonly used to solve this problem. The problem is simplified as a linear problem in the DC power flow technique. This chapter will provide an overview of different techniques used to solve the power flow problem.

Keywords: power flow, load flow, iterative techniques, Newton-Raphson, Gauss-Seidel, fast-decoupled, DC power flow

1. Problem formulation

Power flow analysis is a fundamental study discussed in any power system analysis textbook such as [1–6]. The objective of a power flow study is to calculate the voltages (magnitude and angle) for a given load, generation, and network condition. Once voltages are known for all buses, line flows and losses can be calculated. The starting point of solving power flow problems is to identify the known and unknown variables in the system. Based on these variables, buses are classified into three types: slack, generation, and load buses as shown in **Table 1**.

The slack bus is required to provide the mismatch between scheduled generation the total system load including losses and total generation. The slack bus is commonly considered as the reference bus because both voltage magnitude and angles are specified; therefore, it is called the swing bus. The rest of generator buses are called regulated or PV buses because the net real power is specified and voltage magnitude is regulated. Most of the buses in practical power systems are load buses. Load buses are called PQ buses because both net real and reactive power loads are specified.

For PQ buses, both voltage magnitudes and angles are unknown, whereas for PV buses, only the voltage angle is unknown. As both voltage magnitudes and angles are specified for the Slack bus, there are no variables that must be solved for. In a system with *n* buses and *g* generators, there are *2(n-1)-(g-1)* unknowns. To solve these unknowns, real and reactive power balance equations are used. To write these equations, the transmission network is modeled using the admittance matrix (Y-bus).

Bus type	Voltage ($\lvert V_i \rvert \angle \delta_i$)		Real power			Reactive power		
	Magnitude	**Angle**	**Generation**	**Load**	**Net (P_i)**	**Generation**	**Load**	**Net (Q_i)**
Slack/ Swing	Specified	Specified	Unknown	Specified	Unknown	Unknown	Specified	Unknown
Generator/ Regulated/ PV	Specified	Unknown	Specified	Specified	Specified	Unknown	Specified	Unknown
Load/PQ	Unknown	Unknown	Specified	Specified	Specified	Specified	Specified	Specified

Table 1.
Type of buses in the power flow problem.

2. Admittance matrix and power flow equation

The admittance matrix of a power system is an abstract mathematical model of the system. It consists of admittance values of both lines and buses. The Y-bus is a square matrix with dimensions equal to the number of buses. This matrix is symmetrical along the diagonal.

$$Y = \begin{bmatrix} Y_{11} & \cdots & Y_{1n} \\ \vdots & \ddots & \vdots \\ Y_{n1} & \cdots & Y_{nn} \end{bmatrix} \tag{1}$$

The values of diagonal elements (Y_{ii}) are equal to the sum of the admittances connected to bus i. The off-diagonal elements (Y_{ij}) are equal to the negative of the admittance connecting the two buses i and j. It is worth noting that with large systems, Y-bus is a sparse matrix.

$$Y_{ii} = \sum_{\substack{j=0 \\ j \neq i}}^{n} y_{ij} \tag{2}$$

$$Y_{ij} = Y_{ji} = -y_{ij} \tag{3}$$

The net injected power at any bus can be calculated using the bus voltage (V_i), neighboring bus voltages (V_j), and admittances between the bus and its neighboring buses (y_{ij}) as shown in **Figure 1**.

$$I_i = V_i y_{i0} + (V_i - V_1)y_{i1} + (V_i - V_2)y_{i2} + \ldots + (V_i - V_j)y_{ij}$$

Rearranging the elements as a function of voltages, the current equation becomes as follows:

$$I_i = V_i \left(y_{i0} + y_{i1} + y_{i2} + \ldots + y_{ij} \right) - V_1 y_{i1} - V_2 y_{i2} - \ldots - V_j y_{ij}$$

$$I_i = V_i \sum_{\substack{j=0 \\ j \neq i}} y_{ij} - \sum_{\substack{j=1 \\ j \neq i}} y_{ij} V_j = V_i Y_{ii} + \sum_{\substack{j=1 \\ j \neq i}} Y_{ij} V_j$$

The power equation at any bus can be written as follows:

$$S_i = P_i + jQ_i = V_i I_i^*$$
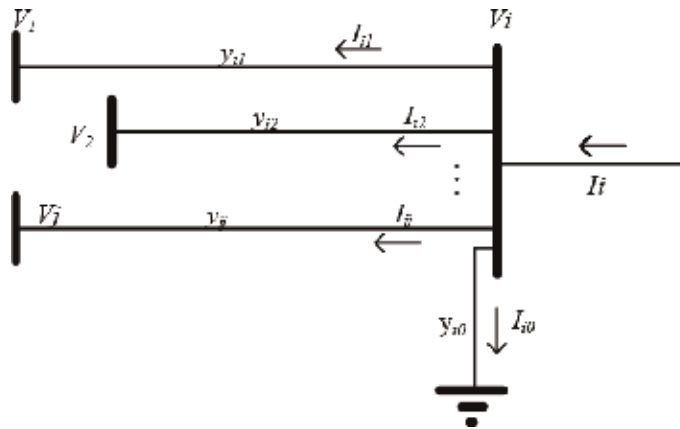
Figure 1.
Net injected power.

Or

$$S_i^* = P_i - jQ_i = V_i^* I_i$$

Substituting the expression on the current in S_i^* equation results in the following formula:

$$S_i^* = V_i^* \left(V_i \sum_{\substack{j=0 \\ j \neq i}} y_{ij} - \sum_{\substack{j=1 \\ j \neq i}} y_{ij} V_j \right) = V_i^* \left(V_i Y_{ii} + \sum_{\substack{j=1 \\ j \neq i}} Y_{ij} V_j \right)$$

Real and reactive power can be calculated from the following equations:

$$P_i = Re \left\{ V_i^* \left(V_i \sum_{\substack{j=0 \\ j \neq i}} y_{ij} - \sum_{\substack{j=1 \\ j \neq i}} y_{ij} V_j \right) \right\} = Re \left\{ V_i^* \left(V_i Y_{ii} + \sum_{\substack{j=1 \\ j \neq i}} Y_{ij} V_j \right) \right\}$$

$$Q_i = -Im \left\{ V_i^* \left(V_i \sum_{\substack{j=0 \\ j \neq i}} y_{ij} - \sum_{\substack{j=1 \\ j \neq i}} y_{ij} V_j \right) \right\} = -Im \left\{ V_i^* \left(V_i Y_{ii} + \sum_{\substack{j=1 \\ j \neq i}} Y_{ij} V_j \right) \right\}$$

Or

$$P_i = \sum_{j=1}^{n} |V_i||V_j||Y_{ij}| \cos \left(\theta_{ij} - \delta_i + \delta_j \right) \tag{4}$$

$$Q_i = -\sum_{j=1}^{n} |V_i||V_j||Y_{ij}| \sin \left(\theta_{ij} - \delta_i + \delta_j \right) \tag{5}$$

And the current (I_i) can be written as a function of the power as follows:

$$\frac{P_i - jQ_i}{V_i^*} = V_i \sum_{\substack{j=0 \\ j \neq i}} y_{ij} - \sum_{\substack{j=1 \\ j \neq i}} y_{ij} V_j = V_i Y_{ii} + \sum_{\substack{j=1 \\ j \neq i}} Y_{ij} V_j \tag{6}$$
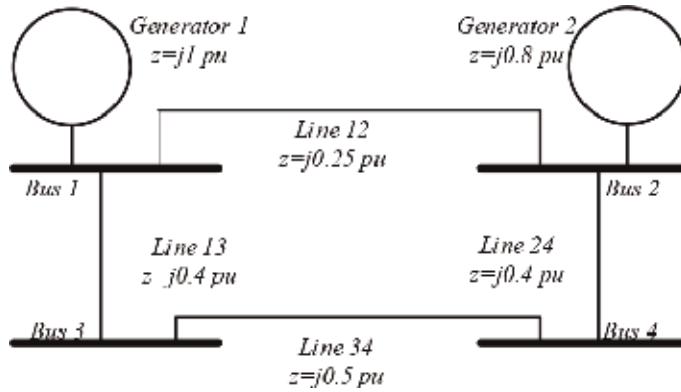
Figure 2.
Impedance diagram.
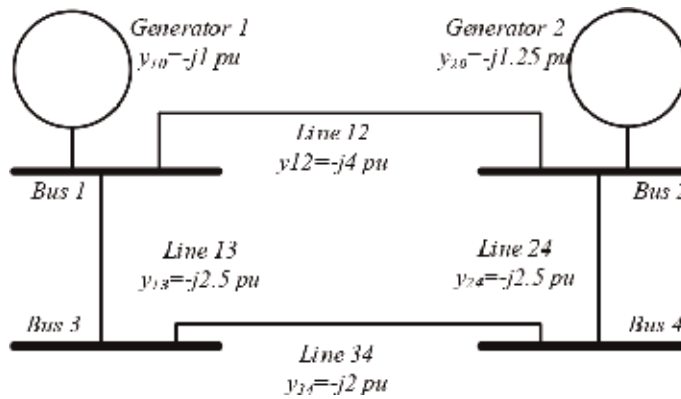
Figure 3.
Admittance diagram.

Example 1: Admittance matrix formation.

For the below 4-bus system in **Figure 2**, the admittance matrix is constructed by converting all impedances in the system into admittances as shown in **Figure 3**. Then, diagonal and off-diagonal elements are calculated using Eqs. (2) and (3).

$$
Y = \begin{bmatrix} -j7.5 & j4 & j2.5 & 0 \\ j4 & -j7.75 & 0 & j2.5 \\ j2.5 & 0 & -j4.5 & j2 \\ 0 & j2.5 & j2 & -j4.5 \end{bmatrix} = \begin{bmatrix} 7.5\angle-90° & 4\angle90° & 2.5\angle90° & 0 \\ 4\angle90° & 7.75\angle-90° & 0 & 2.5\angle90° \\ 2.5\angle90° & 0 & 4.5\angle-90° & 2\angle90° \\ 0 & 2.5\angle90° & 2\angle90° & 4.5\angle-90° \end{bmatrix}
$$

3. Gauss-Seidel technique

The Gauss-Seidel (GS) method, also known as the method of successive displacement, is the simplest iterative technique used to solve power flow problems. In general, GS method follows the following iterative steps to reach the solution for the function $f(x) = 0$:

- Rearrange the function into the form $x = g(x)$ to calculate the unknown variable.

- Calculate the value $g\left(x^{[0]}\right)$ based on initial estimates $x^{[0]}$.

- Calculate the improved value $x^{[1]} = g\left(x^{[0]}\right)$.

- Continue solving for improved values until the solution is within acceptable limits $\left|x^{[k+1]} - x^{[k]}\right| \leq \epsilon$.

The rate of convergence can be improved using acceleration factors by modifying the step size α.

$$x^{[k+1]} = x^{[k]} + \alpha\left[g\left(x^{[k+1]}\right) - x^{[k]}\right] \tag{7}$$

In the context of a power flow problem, the unknown variables are voltages at all buses, but the slack. Both voltage magnitudes and angles are unknown for load buses, whereas voltage angles are unknown for regulated/generation buses.

The voltage V_i at bus i can be calculated using either equations:

$$V_i = \frac{1}{\sum_{\substack{j=1}} y_{ij}} \left(\frac{P_i^{sch} - jQ_i^{sch}}{V_i^*} + \sum_j y_{ij} V_j\right) \tag{8}$$
$$j \neq i$$

$$V_i = \frac{1}{Y_{ii}} \left(\frac{P_i^{sch} - jQ_i^{sch}}{V_i^*} - \sum_{\substack{j=1 \\ j \neq i}} Y_{ij} V_j\right) \tag{9}$$

where y_{ij} is the admittance between buses i and j, Y_{ij} is the Y-bus element, P_i^{sch} the net scheduled injected real power, Q_i^{sch} is the net scheduled injected reactive power, and V_i^* is the conjugate of V_i. The net injected quantities are the sum of the generation minus load. Typically, the initial estimates of $V_i = 1\angle 0°$.

The iterative voltage equation is as follows:

$$V_i^{[k+1]} = \frac{1}{Y_{ii}} \left(\frac{P_i^{sch} - jQ_i^{sch}}{V_i^{*[k]}} - \sum_{j \neq i} Y_{ij} V_j^{[k \text{ or } k+1]}\right) \tag{10}$$

Or

$$V_i^{[k+1]} = \frac{1}{\sum_{j=0} y_{ij}} \left(\frac{P_i^{sch} - jQ_i^{sch}}{V_i^*} + \sum_{j \neq i} y_{ij} V_j^{[k \text{ or } k+1]}\right) \tag{11}$$

Both real and reactive powers are scheduled for the load buses, and Eq. 6 is used to determine both voltage magnitudes and angles ($|V_i| \angle \delta$) for every iteration ($V_i^{[k+1]}$).

For regulated buses, only real power is scheduled. Therefore, net injected reactive power is calculated based on the iterative voltages ($V_i^{[k+1]}$) using either equations:

$$Q_i^{[k+1]} = -Im\left\{V_i^{*[k]}\left(V_i^{[k]} \sum_{j=0}^{n} y_{ij} - \sum_{\substack{j=1 \\ j \neq i}}^{n} y_{ij} V_j^{[k \text{ or } k+1]}\right)\right\} \tag{12}$$

$$Q_i{}^{[k+1]} = -\sum_{j=1}^{n} |V_i|^{[k]} |V_j|^{[k \ or \ k+1]} |Y_{ij}| \ sin\left(\theta_{ij} - \delta_i{}^{[k]} + \delta_j{}^{[k]}\right) \qquad (13)$$

where $|V_i|$ and $|V_j|$ are the magnitudes of the voltage at buses i and j, respectively. δ_i and δ_j are the associated angles. y_{ij} is the admittance between buses i and j. $|Y_{ij}|$ is the magnitude of the Y-bus element between the two buses; and θ_{ij} is the corresponding angle.

Since the voltage magnitude ($|V_i|$) is specified at regulated/PV buses, Eqs. (8) or (9) will be used to determine the voltage angles only. To achieve this, two options can be used:

1. When using the polar form ($|V_i| \angle \delta_i$), discard the iterative voltage magnitude and keep the iterative angle.

2. When using the rectangular form ($Re_i + j \ Im_i$), discard the real part (Re_i) and keep the imaginary part (Im_i) of the iterative voltage. The new real part ($Re_i{}^{new}$) can be calculated from the specified magnitude ($|V_i|$) and the iterative imaginary part.

$$Re_i{}^{new} = \sqrt{|V_i|^2 - Im_i{}^2} \qquad (14)$$

The iterative process stops when the voltage improvement reaches acceptable limits: $|V_i{}^{[k+1]} - V_i{}^{[k]}| \le \epsilon$.

Example 2: Gauss-Seidel power flow solution.

Figure 4 below shows a 3-bus system. Perform 2 iterations to obtain the voltage magnitude and angles at buses 2 and 3. Impedances are given on 100 MVA base.

Solution:

The admittance values of the transmission network and the injected power in per unit at buses 2 and 3 are calculated as shown in **Figure 5**. Note that net injected power at the load bus is negative while that of the PV bus is positive. Per units values are obtained by diving actual values (MW and MVAR) by the base (100 MVA).

Iteration #1: assume $V_2{}^{[0]} = 1.00 \angle 0°$ and $V_3{}^{[0]} = 1.03 \angle 0°$.

$$V_2{}^{[1]} = \frac{1}{y_{21} + y_{23}} \left(\frac{P_2{}^{sch} - jQ_2{}^{sch}}{V_2{}^{[0]*}} + y_{21}V_1 + y_{23}V_3{}^{[0]} \right)$$

$$= \frac{1}{(5 - j15) + (15 - j50)} \left(\frac{-2 + j0.5}{1.00 \angle 0°} + (5 - j15)1.02 \angle 0° + (15 - j50)1.00 \angle 0° \right)$$

$$V_2{}^{[1]} = 1.0120 - j0.0260 = 1.0123 \angle -1.4717°$$

As Q_3 is not given, it is calculated based on the latest available information using Eqs. (12) or (13).

$$Q_3{}^{[1]} = -Im\left\{ V_3{}^{*[0]} \left(V_3{}^{[0]} \sum_{j=0}^{n} y_{3j} - \sum_{\substack{j=1 \\ j \neq i}}^{n} y_{3j} V_j{}^{[k \ or \ k+1]} \right) \right\}$$

$$Q_3{}^{[1]} = -Im\left\{ V_3{}^{*[0]} \left(V_3{}^{[0]} (y_{31} + y_{32}) - \left[y_{31}V_1 + y_{32}V_2{}^{[1]} \right] \right) \right\}$$
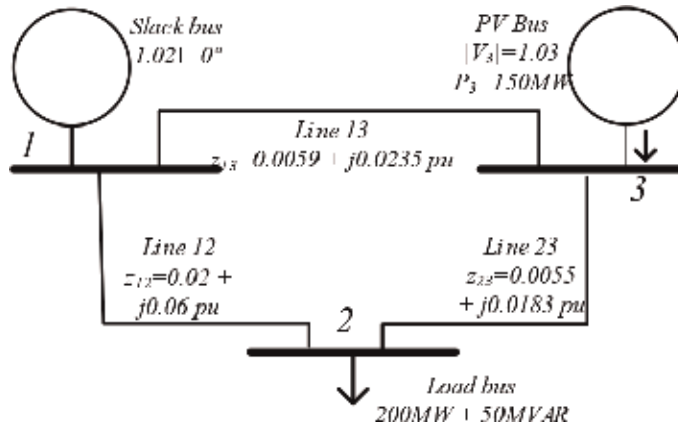
Figure 4.
3-Bus power system.
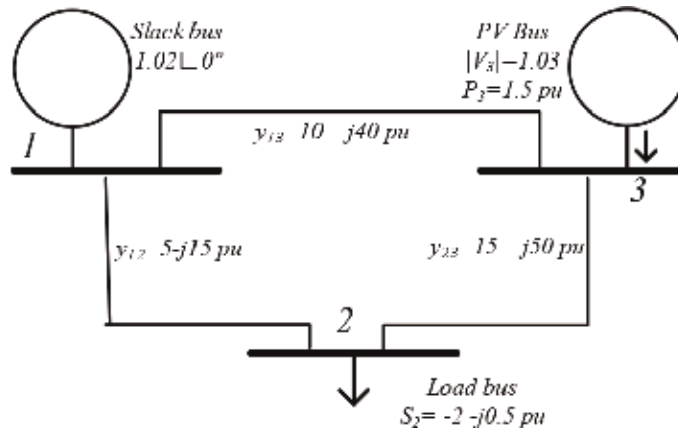
Figure 5.
Power flow input data.

$$Q_3^{[1]} = -Im\{1.03 \angle 0°(1.03 \angle 0°(10 - j40 + 15 - j50) - [(10 - j40)1.02 \angle 0°$$
$$+(15 - j50)(1.0120 - j0.0260)])\}$$
$$= -Im\{1.7201 - j0.9373\} = 0.9373\, pu$$

Now that $Q_3^{[1]}$ is calculated, the voltage $V_3^{[1]}$ can be calculated:

$$V_3^{[1]} = \frac{1}{y_{31} + y_{32}}\left(\frac{P_3^{sch} - jQ_3^{[1]}}{V_3^{[0]*}} + y_{31}V_1 + y_{32}V_2^{[1]}\right)$$

$$= \frac{1}{10 - j40 + 15 - j50}\left(\frac{1.5 - j0.9373}{1.03 \angle 0°} + (10 - j40)1.02 \angle 0° + (15 - j50)(1.0120 - j0.0260)\right)$$

$$= 1.0294 - j0.0022\, pu$$

Since the magnitude of V_3 is specified, we retain the imaginary part of $V_3^{[1]}$ and calculate the real part using Eq. (14).

$$Re_i^{new} = \sqrt{1.03^2 - 0.0022^2} = 1.03\, pu$$

Therefore,

$$V_3^{[1]} = V_3^{[1]} = 1.03 - j0.0022 = 1.03 \angle -0.1226° \ pu$$

Iteration #2: considering $V_2^{[1]} = 1.0120 - j0.0260$ and $V_3^{[1]} = 1.03 - j0.0022$.

$$V_2^{[2]} = \frac{1}{y_{21} + y_{23}} \left(\frac{P_2^{sch} - jQ_2^{sch}}{V_2^{[1]*}} + y_{21}V_1 + y_{23}V_3^{[1]} \right)$$

$$= \frac{1}{(5-j15)+(15-j50)} \left(\frac{-2+j0.5}{1.0120-j0.0260} + (5-j15)1.02 \angle 0° + (15-j50)(1.03-j0.0022) \right) V_2^{[2]}$$

$$= 1.0115 - j\,0.0270 = 1.0119 \angle -1.5273°$$

$Q_3^{[2]}$ calculation is given below:

$$Q_3^{[2]} = -Im \left\{ V_3^{*[1]} \left(V_3^{[1]} (y_{31} + y_{32}) - \left[y_{31}V_1 + y_{32}V_2^{[2]} \right] \right) \right\}$$

$$Q_3^{[2]} = -Im\{(1.03 - j0.0022)((1.03 - j0.0022)(10 - j40 + 15 - j50)$$
$$- \left[(10-j40)1.02 \angle 0° + (15-j50)(1.0115 - j\,0.0270) \right]) \}$$
$$= 1.0000 \ pu$$

The voltage $V_3^{[2]}$ is calculated as follows:

$$V_3^{[2]} = \frac{1}{y_{31} + y_{32}} \left(\frac{P_3^{sch} - jQ_3^{[2]}}{V_3^{[1]*}} + y_{31}V_1 + y_{32}V_2^{[2]} \right)$$

$$= \frac{1}{10-j40+15-j50} \left(\frac{1.5-j1}{1.03 \angle 0°} + (10-j40)1.02 \angle 0° + (15-j50)(1.0115 - j\,0.0270) \right)$$

$$= 1.0298 - j0.0030 \ pu$$

Only imaginary value of the calculated $V_3^{[2]}$ is retained and the real part is calculated based on the retained imaginary values and the scheduled $|V_3|$.

$$Re_i^{new} = \sqrt{1.03^2 - 0.0030^2} = 1.03 \ pu$$

Therefore,

$$V_3^{[2]} = 1.03 - j0.003 = 1.03 \angle -0.1644° \ pu$$

The iterative solution is presented in **Table 2**.

Iteration	$V_2^{[k]}$	$V_3^{[k]}$
1	$1.0123 \angle -1.4717°$	$1.03 \angle -0.1226°$
2	$1.0119 \angle -1.5273°$	$1.03 \angle -0.1644°$
3	$1.0119 \angle -1.5598°$	$1.03 \angle -0.1846°$
4	$1.0119 \angle -1.5750°$	$1.03 \angle -0.1941°$
5	$1.0118 \angle -1.5823°$	$1.03 \angle -0.1986°$
6	$1.0118 \angle -1.5857°$	$1.03 \angle -0.2008°$

Table 2.
Gauss-Seidel iterative solution.

4. Newton-Raphson technique

The Newton-Raphson (N-R) technique, also known as the method of successive approximation, is based on Taylor's expansion approximation. The unknown x in the function $f(x) = c$ can be determined using Taylor's expansion approximation. Starting with an initial estimate $x^{[0]}$, the deviation from the correct solution is $\Delta x^{[0]}$. Applying Taylor's expansion, the function can be written as follows:

$$f\left(x^{[0]} + \Delta x^{[0]}\right) = c \tag{15}$$

$$f\left(x^{[0]} + \Delta x^{[0]}\right) = f\left(x^{[0]}\right) + f'\left(x^{[0]}\right)\Delta x^{[0]} + \frac{1}{2!}f''\left(x^{[0]}\right)\Delta x^{[0]\,2} + \frac{1}{3!}f'''\left(x^{[0]}\right)\Delta x^{[0]\,3} + \ldots = c \tag{16}$$

Assuming $\Delta x^{[0]}$ is small, the higher order terms $(\frac{1}{2!}f''\left(x^{[0]}\right)\Delta x^{[0]\,2} + \frac{1}{3!}f'''\left(x^{[0]}\right)\Delta x^{[0]\,3} + \ldots)$ are neglected and the function can be approximated by the first two terms.

$$f\left(x^{[0]} + \Delta x^{[0]}\right) \approx f\left(x^{[0]}\right) + f'\left(x^{[0]}\right)\Delta x^{[0]} = c \tag{17}$$

Based on $x^{[0]}$, the deviation from the correct solution can be iteratively calculated.

$$\Delta x^{[0]} = \frac{c - f\left(x^{[0]}\right)}{f'(x^{[0]})} = \frac{\Delta f\left(x^{[0]}\right)}{f'(x^{[0]})} \tag{18}$$

The improved solution can be calculated iteratively.

$$x^{[1]} = x^{[0]} + \Delta x^{[0]} \tag{19}$$

The iterative process is stopped when the mismatch between scheduled and calculated value $(\Delta f^{[k]} = c - f\left(x^{[k]}\right))$ is within acceptable limits $\left|\Delta f^{[k]}\right| \leq \epsilon$.

In the context of power flow problems, unknown variables x are both voltage magnitude and angles $(|V_i| \angle \delta_i)$ at load buses, as well as voltage angles (δ_i) at regulated buses. The scheduled (specified) quantities (c) are both net real (P_i^{sch}) and reactive power (jQ_i^{sch}) values at load buses and real power at generation buses as shown in **Table 1**. The iterative values of reactive power are calculated using Eqs. (12) or (13). Similarly, the iterative values of real power are calculated using Eqs. (20) or (21):

$$P_i^{[k+1]} = Re\left\{V_i^{*[k]}\left(V_i^{[k]}\sum_{j=0}^{n} y_{ij} - \sum_{\substack{j=1 \\ j \neq i}}^{n} y_{ij}V_j^{[k \text{ or } k+1]}\right)\right\} \tag{20}$$

$$P_i^{[k+1]} = \sum_{j=1}^{n} |V_i|^{[k]}|V_j|^{[k \text{ or } k+1]}|Y_{ij}|\cos\left(\theta_{ij} - \delta_i^{[k]} + \delta_j^{[k]}\right) \tag{21}$$

The Newton-Raphson power flow formulation can be written as follows:

$$x^{[k]} = \begin{bmatrix} \delta_i^{[k]} \\ |V_i|^{[k]} \end{bmatrix}, c = \begin{bmatrix} P_i^{sch} \\ Q_i^{sch} \end{bmatrix}, f = \begin{bmatrix} P_i^{[k]} \\ Q_i^{[k]} \end{bmatrix}, \text{ and } \begin{bmatrix} P_i^{sch} \\ Q_i^{sch} \end{bmatrix} - \begin{bmatrix} P_i^{[k]} \\ Q_i^{[k]} \end{bmatrix} = \begin{bmatrix} \Delta P_i^{[k]} \\ \Delta Q_i^{[k]} \end{bmatrix}.$$

When more variables are used, the derivative f' is replaced by partial derivatives with respect to different variables. The partial derivative matrix is called the Jacobian matrix.

$$f' = \begin{bmatrix} \dfrac{\partial P_i}{\partial \delta_i} & \dfrac{\partial P_i}{\partial |V_i|} \\ \dfrac{\partial Q_i}{\partial \delta_i} & \dfrac{\partial Q_i}{\partial |V_i|} \end{bmatrix} = \begin{bmatrix} J_{P\delta} & J_{P|V|} \\ J_{Q\delta} & J_{Q|V|} \end{bmatrix} \tag{22}$$

Therefore, the Newton-Raphson power flow formulation can be solved using the below equation:

$$\begin{bmatrix} P_i^{sch} \\ Q_i^{sch} \end{bmatrix} - \begin{bmatrix} P_i^{[k]} \\ Q_i^{[k]} \end{bmatrix} = \begin{bmatrix} \Delta P_i^{[k]} \\ \Delta Q_i^{[k]} \end{bmatrix} = \begin{bmatrix} \frac{\partial P_i^{[k]}}{\partial \delta_i} & \frac{\partial P_i^{[k]}}{\partial |V_i|} \\ \frac{\partial Q_i^{[k]}}{\partial \delta_i} & \frac{\partial Q_i^{[k]}}{\partial |V_i|} \end{bmatrix} \begin{bmatrix} \Delta \delta_i^{[k]} \\ \Delta |V_i|^{[k]} \end{bmatrix} \tag{23}$$

To solve for the deviation, the inverse of the Jacobian matrix is required for every iteration.

$$\begin{bmatrix} \Delta \delta^{[k]} \\ \Delta |V_i|^{[k]} \end{bmatrix} = \begin{bmatrix} J_{P\delta}^{[k]} & J_{P|V|}^{[k]} \\ J_{Q\delta}^{[k]} & J_{Q|V|}^{[k]} \end{bmatrix}^{-1} \begin{bmatrix} \Delta P_i^{[k]} \\ \Delta Q_i^{[k]} \end{bmatrix} \tag{24}$$

Then, new values are calculated:

$$\begin{bmatrix} \delta_i^{[k]} \\ |V_i|^{[k]} \end{bmatrix} = \begin{bmatrix} \delta_i^{[k-1]} \\ |V_i|^{[k-1]} \end{bmatrix} + \begin{bmatrix} \Delta \delta_i^{[k]} \\ \Delta |V_i|^{[k]} \end{bmatrix} \tag{25}$$

The iterative process stops when the mismatch between calculated and scheduled quantities is within $\begin{bmatrix} \Delta P_i^{[k]} \\ \Delta Q_i^{[k]} \end{bmatrix} \leq \epsilon$.

Example 3: Newton-Raphson power flow solution.

Solve the power flow problem shown in **Figure 3** using the Newton-Raphson technique. Perform two iterations.

Solution:

The first step in Newton-Raphson Power Flow technique is building Y-bus using Eqs. (2) and (3).

$$Y = \begin{bmatrix} 15 - j55 & -5 + j15 & -10 + j40 \\ -5 + j15 & 20 - j65 & -15 + j50 \\ -10 + j40 & -15 + j50 & 25 - j90 \end{bmatrix}$$

$$= \begin{bmatrix} 57.01 \angle -74.74^\circ & 15.81 \angle 108.43^\circ & 41.23 \angle 104.04^\circ \\ 15.81 \angle 108.43^\circ & 68.01 \angle -72.90^\circ & 52.20 \angle 106.70^\circ \\ 41.23 \angle 104.04^\circ & 52.20 \angle 106.70^\circ & 93.41 \angle -74.48^\circ \end{bmatrix}$$

Since the unknown variables are δ_2, δ_3, and $|V_2|$; the scheduled quantities are P_2^{sch}, P_3^{sch}, and Q_2^{sch}, the following problem formulation can be written.

$$
\begin{bmatrix} P_2{}^{sch} \\ P_3{}^{sch} \\ Q_2{}^{sch} \end{bmatrix} - \begin{bmatrix} P_2{}^{[k]} \\ P_3{}^{[k]} \\ Q_2{}^{[k]} \end{bmatrix} = \begin{bmatrix} \dfrac{\partial P_2{}^{[k]}}{\partial \delta_2} & \dfrac{\partial P_2{}^{[k]}}{\partial \delta_3} & \dfrac{\partial P_2{}^{[k]}}{\partial |V_2|} \\[2mm] \dfrac{\partial P_3{}^{[k]}}{\partial \delta_2} & \dfrac{\partial P_3{}^{[k]}}{\partial \delta_3} & \dfrac{\partial P_3{}^{[k]}}{\partial |V_2|} \\[2mm] \dfrac{\partial Q_2{}^{[k]}}{\partial \delta_2} & \dfrac{\partial Q_2{}^{[k]}}{\partial \delta_3} & \dfrac{\partial Q_2{}^{[k]}}{\partial |V_2|} \end{bmatrix} \begin{bmatrix} \Delta\delta_2{}^{[k]} \\ \Delta\delta_3{}^{[k]} \\ \Delta|V_2|^{[k]} \end{bmatrix}
$$

To calculate the Jacobian matrix elements, P_2, P_3, and Q_2 equations are obtained using (4) and (5).

$$
P_2 = \sum_{j=1}^{n} |V_2||V_j||Y_{2j}| \cos\left(\theta_{2j} - \delta_2 + \delta_j\right)
$$

$$
= |V_2||V_1||Y_{21}| \cos\left(\theta_{21} - \delta_2 + \delta_1\right) + |V_2|^2 |Y_{22}| \cos\left(\theta_{22}\right) + |V_2||V_3||Y_{23}| \cos\left(\theta_{23} - \delta_2 + \delta_3\right)
$$

$$
\frac{\partial P_2}{\partial \delta_2} = |V_2||V_1||Y_{21}| \sin\left(\theta_{21} - \delta_2 + \delta_1\right) + |V_2||V_3||Y_{23}| \sin\left(\theta_{23} - \delta_2 + \delta_3\right)
$$

$$
\frac{\partial P_2}{\partial \delta_3} = -|V_2||V_3||Y_{23}| \sin\left(\theta_{23} - \delta_2 + \delta_3\right)
$$

$$
\frac{\partial P_2}{\partial |V_2|} = |V_1||Y_{21}| \cos\left(\theta_{21} - \delta_2 + \delta_1\right) + 2|V_2||Y_{22}| \cos\left(\theta_{22}\right) + |V_3||Y_{23}| \cos\left(\theta_{23} - \delta_2 + \delta_3\right)
$$

$$
P_3 = \sum_{j=1}^{n} |V_3||V_j||Y_{3j}| \cos\left(\theta_{3j} - \delta_3 + \delta_j\right)
$$

$$
= |V_3||V_1||Y_{31}| \cos\left(\theta_{31} - \delta_3 + \delta_1\right) + |V_3||V_2||Y_{32}| \cos\left(\theta_{32} - \delta_3 + \delta_2\right) + |V_3|^2 |Y_{33}| \cos\left(\theta_{33}\right)
$$

$$
\frac{\partial P_3}{\partial \delta_2} = -|V_2||V_3||Y_{32}| \sin\left(\theta_{32} - \delta_3 + \delta_2\right)
$$

$$
\frac{\partial P_3}{\partial \delta_3} = |V_3||V_1||Y_{31}| \sin\left(\theta_{31} - \delta_3 + \delta_1\right) + |V_3||V_2||Y_{32}| \sin\left(\theta_{32} - \delta_3 + \delta_2\right)
$$

$$
\frac{\partial P_3}{\partial |V_2|} = |V_3||Y_{32}| \cos\left(\theta_{32} - \delta_3 + \delta_2\right)
$$

$$
Q_2 = -\sum_{j=1}^{n} |V_2||V_j||Y_{2j}| \sin\left(\theta_{2j} - \delta_2 + \delta_j\right)
$$

$$
= -|V_2||V_1||Y_{21}| \sin\left(\theta_{21} - \delta_2 + \delta_1\right) - |V_2|^2 |Y_{22}| \sin\left(\theta_{22}\right) - |V_2||V_3||Y_{23}| \sin\left(\theta_{23} - \delta_2 + \delta_3\right)
$$

$$
\frac{\partial Q_3}{\partial \delta_2} = |V_2||V_1||Y_{21}| \cos\left(\theta_{21} - \delta_2 + \delta_1\right) + |V_2||V_3||Y_{23}| \cos\left(\theta_{23} - \delta_2 + \delta_3\right)
$$

$$
\frac{\partial Q_3}{\partial \delta_3} = -|V_2||V_3||Y_{23}| \cos\left(\theta_{23} - \delta_2 + \delta_3\right)
$$

$$
\frac{\partial Q_3}{\partial |V_2|} = -|V_1||Y_{21}| \sin\left(\theta_{21} - \delta_2 + \delta_1\right) - 2|V_2||Y_{22}| \sin\left(\theta_{22}\right) - |V_3||Y_{23}| \sin\left(\theta_{23} - \delta_2 + \delta_3\right)
$$

Iteration #1: assume $V_2{}^{[0]} = 1.00 \angle 0°$ and $V_3{}^{[0]} = 1.03 \angle 0°$.

The calculated quantities: $\begin{bmatrix} P_2{}^{[1]} \\ P_3{}^{[1]} \\ Q_2{}^{[1]} \end{bmatrix} = \begin{bmatrix} -0.5500 \\ 0.5665 \\ -1.8000. \end{bmatrix}$

The scheduled quantities: $\begin{bmatrix} P_2{}^{sch} \\ P_3{}^{sch} \\ Q_2{}^{sch} \end{bmatrix} = \begin{bmatrix} -2 \\ 1.5 \\ -0.5 \end{bmatrix}$

The mismatch power matrix:
$$
\begin{bmatrix} \Delta P_2^{[1]} \\ \Delta P_3^{[1]} \\ \Delta Q_2^{[1]} \end{bmatrix} = \begin{bmatrix} -2 \\ 1.5 \\ -0.5 \end{bmatrix} - \begin{bmatrix} -0.5500 \\ 0.5665 \\ -1.8000 \end{bmatrix} = \begin{bmatrix} -1.4500 \\ 0.9335 \\ 1.3000 \end{bmatrix}
$$

The Jacobian matrix (J) elements for iteration # 1 are as follows:

$$
J = \begin{bmatrix} 66.8 & -51.5 & 19.45 \\ -51.5 & 93.52 & -15.45 \\ -20.55 & 15.45 & 63.2 \end{bmatrix}
$$

Newton-Raphson formulation is as follows:

$$
\begin{bmatrix} -1.4500 \\ 0.9335 \\ 1.3000 \end{bmatrix} = \begin{bmatrix} 66.8 & -51.5 & 19.45 \\ -51.5 & 93.52 & -15.45 \\ -20.55 & 15.45 & 63.2 \end{bmatrix} \begin{bmatrix} \Delta\delta_2^{[1]} \\ \Delta\delta_3^{[1]} \\ \Delta|V_2|^{[1]} \end{bmatrix}
$$

$$
\begin{bmatrix} \Delta\delta_2^{[1]} \\ \Delta\delta_3^{[1]} \\ \Delta|V_2|^{[1]} \end{bmatrix} = \begin{bmatrix} 66.8 & -51.5 & 19.45 \\ -51.5 & 93.52 & -15.45 \\ -20.55 & 15.45 & 63.2 \end{bmatrix}^{-1} \begin{bmatrix} -1.4500 \\ 0.9335 \\ 1.3000 \end{bmatrix} = \begin{bmatrix} -0.0279\ rad \\ -0.0033\ rad \\ 0.0123\ pu \end{bmatrix}
$$

$$
\begin{bmatrix} \delta_2^{[1]} \\ \delta_3^{[1]} \\ |V_2|^{[1]} \end{bmatrix} = \begin{bmatrix} \delta_2^{[0]} \\ \delta_3^{[0]} \\ |V_2|^{[0]} \end{bmatrix} + \begin{bmatrix} \Delta\delta_2^{[1]} \\ \Delta\delta_3^{[1]} \\ \Delta|V_2|^{[1]} \end{bmatrix}
$$

$$
\begin{bmatrix} \delta_2^{[1]} \\ \delta_3^{[1]} \\ |V_2|^{[1]} \end{bmatrix} = \begin{bmatrix} 0 \\ 0 \\ 1.00 \end{bmatrix} + \begin{bmatrix} -0.0279\ rad \\ -0.0033\ rad \\ 0.0123\ pu \end{bmatrix} = \begin{bmatrix} -0.0279\ rad \\ -0.0033\ rad \\ 1.0123\ pu \end{bmatrix} = \begin{bmatrix} -1.5986° \\ -0.1891° \\ 1.0123\ pu \end{bmatrix}
$$

Iteration #2: Consider $V_2^{[1]} = 1.0123\ \angle -1.5986°$ and $V_3^{[1]} = 1.03\ \angle -0.1891°$.

The calculated quantities:
$$
\begin{bmatrix} P_2^{[2]} \\ P_3^{[2]} \\ Q_2^{[2]} \end{bmatrix} = \begin{bmatrix} -2.0109 \\ 1.5202 \\ -0.4621 \end{bmatrix}
$$

The mismatch power matrix:
$$
\begin{bmatrix} \Delta P_2^{[2]} \\ \Delta P_3^{[2]} \\ \Delta Q_2^{[2]} \end{bmatrix} = \begin{bmatrix} -2 \\ 1.5 \\ -0.5 \end{bmatrix} - \begin{bmatrix} -2.0109 \\ 1.5202 \\ -0.4621 \end{bmatrix} = \begin{bmatrix} 0.0109 \\ -0.0202 \\ -0.0379 \end{bmatrix}
$$

The Jacobian matrix elements are calculated as follows:

$$
J = \begin{bmatrix} 67.07 & -51.74 & 18.26 \\ -52.50 & 94.49 & -14.18 \\ -22.51 & 16.91 & 65.34 \end{bmatrix}
$$

$$
\begin{bmatrix} \Delta\delta_2^{[2]} \\ \Delta\delta_3^{[2]} \\ \Delta|V_2|^{[2]} \end{bmatrix} = \begin{bmatrix} 67.07 & -51.74 & 18.26 \\ -52.50 & 94.49 & -14.18 \\ -22.51 & 16.91 & 65.34 \end{bmatrix}^{-1} \begin{bmatrix} 0.0109 \\ -0.0202 \\ -0.0379 \end{bmatrix}
$$

$$
\begin{bmatrix} \Delta\delta_2^{[2]} \\ \Delta\delta_3^{[2]} \\ \Delta|V_2|^{[2]} \end{bmatrix} = \begin{bmatrix} 0.1272 \times 10^{-3}\ rad \\ -0.2154 \times 10^{-3}\ rad \\ -0.4810 \times 10^{-3}\ pu \end{bmatrix}
$$

$$\begin{bmatrix} \delta_2{}^{[2]} \\ \delta_3{}^{[2]} \\ |V_2|^{[2]} \end{bmatrix} = \begin{bmatrix} \delta_2{}^{[1]} \\ \delta_3{}^{[1]} \\ |V_2|^{[1]} \end{bmatrix} + \begin{bmatrix} \Delta\delta_2{}^{[2]} \\ \Delta\delta_3{}^{[2]} \\ \Delta|V_2|^{[2]} \end{bmatrix}$$

$$\begin{bmatrix} \delta_2{}^{[2]} \\ \delta_3{}^{[2]} \\ |V_2|^{[2]} \end{bmatrix} = \begin{bmatrix} -0.0279 \ rad \\ -0.0033 \ rad \\ 1.0123 \ pu \end{bmatrix} + \begin{bmatrix} 0.1272 \times 10^{-3} \ rad \\ -0.2154 \times 10^{-3} \ rad \\ -0.4810 \times 10^{-3} \ pu \end{bmatrix}$$

$$\begin{bmatrix} \delta_2{}^{[2]} \\ \delta_3{}^{[2]} \\ |V_2|^{[2]} \end{bmatrix} == \begin{bmatrix} -0.0277 \ rad \\ -0.0035 \ rad \\ 1.0118 pu \end{bmatrix} = \begin{bmatrix} -1.5871^{\circ} \\ -0.2005^{\circ} \\ 1.0118 \ pu \end{bmatrix}$$

It is worth noting that the mismatch between calculated and scheduled quantities diminishes very quickly.

$$\begin{bmatrix} \Delta P_2{}^{[1]} \\ \Delta P_3{}^{[1]} \\ \Delta Q_2{}^{[1]} \end{bmatrix} = \begin{bmatrix} -1.4500 \\ 0.9335 \\ 1.3000 \end{bmatrix} and \begin{bmatrix} \Delta P_2{}^{[2]} \\ \Delta P_3{}^{[2]} \\ \Delta Q_2{}^{[2]} \end{bmatrix} = \begin{bmatrix} 0.0109 \\ -0.0202 \\ -0.0379 \end{bmatrix}$$

The iterative solution is presented in **Table 3**.

Iteration	$V_2{}^{[k]}$	$V_3{}^{[k]}$
1	$1.0123 \angle -1.5986^{\circ}$	$1.03 \angle -0.1891^{\circ}$
2	$1.0118 \angle -1.5871^{\circ}$	$1.03 \angle -0.2005^{\circ}$
3	$1.0118 \angle -1.5871^{\circ}$	$1.03 \angle -0.2005^{\circ}$

Table 3.
Newton-Raphson iterative solution.

5. Fast-decoupled technique

In high voltage transmission systems, the voltage angles between adjacent buses are relatively small. In addition, X/R ratio is high. These two properties result in a strong coupling between real power and voltage angle and between reactive power and voltage magnitude. In contrary, the coupling between real power and voltage magnitude, as well as reactive power and voltage angle, is weak. Considering adjacent buses, real power flows from the bus with a higher voltage angle to the bus with a lower voltage angle. Similarly, reactive power flows from the bus with a higher voltage magnitude to the bus with a lower voltage magnitude.

Fast-decoupled power flow technique includes two steps: (1) decoupling real and reactive power calculations; (2) obtaining of the Jacobian matrix elements directly from the Y-bus.

$$\begin{bmatrix} \Delta P \\ \Delta Q \end{bmatrix} = \begin{bmatrix} J_{P\delta} & 0 \\ 0 & J_{Q|V|} \end{bmatrix} \begin{bmatrix} \Delta\delta \\ \Delta|V| \end{bmatrix} \quad (26)$$

or

$$[\Delta P] = [J_{P\delta}][\Delta\delta] \quad (27)$$

Computational Models in Engineering

$$[\Delta Q] = \left[J_{Q|V|} \right] [\Delta |V|] \tag{28}$$

Next step is to obtain $J_{P\delta}$ and $J_{Q|V|}$ from the Y-bus as flowing:

$$[\Delta \delta] = -[B']^{-1} \left[\frac{\Delta P}{|V|} \right] \tag{29}$$

$$[\Delta |V|] = -\left[B'' \right]^{-1} \left[\frac{\Delta Q}{|V|} \right] \tag{30}$$

Where the $[B']$ and $\left[B'' \right]$ are relevant imaginary part of the Y-bus matrix elements. $[B']$ is related to the buses at which real power is scheduled (δ is unknown) and $\left[B'' \right]$ is related to the buses at which reactive power is scheduled ($|V|$ is unknown).

$$B_{ij} = \left| Y_{ij} \right| \sin \left(\theta_{ij} \right) \tag{31}$$

The fast-decoupled technique requires more iterations to converge compared to the Newton-Raphson power flow formulation, especially if X/R ratio is not high. Another advantage of this method is that the Jacobian matrix has constant term elements which are obtained and inverted once at the beginning of the iterative process.

Example 4: Fast-decoupled power flow solution.
Solve the power flow problem shown in **Figure 3** using fast-decoupled power flow technique. Perform two iterations.
Solution:
The first step in fast-decoupled power flow technique is obtaining $[B']$ and $\left[B'' \right]$ from the Y-bus.

$$Y = \begin{bmatrix} 15 - j55 & -5 + j15 & -10 + j40 \\ -5 + j15 & 20 - j65 & -15 + j50 \\ -10 + j40 & -15 + j50 & 25 - j90 \end{bmatrix}$$

Since the unknown voltage angles are δ_2 and δ_3, elements for $[B']$ are obtained from the Y-bus (intersection of columns numbers 2 & 3 and rows numbers 2 & 3) as follows:

$$[B'] = \begin{bmatrix} -65 & 50 \\ 50 & -90 \end{bmatrix}$$

Since the unknown voltage magnitude is $|V_2|$ at bus 2, $\left[B'' \right]$ contains one element only (intersection of the column and the row number 2):

$$[B'] = [-65]$$

The fast-decoupled power flow formulation becomes as follows:

$$\begin{bmatrix} \Delta \delta_2 \\ \Delta \delta_3 \end{bmatrix} = -[B']^{-1} \begin{bmatrix} \frac{\Delta P_2}{|V_2|} \\ \frac{\Delta P_3}{|V_3|} \end{bmatrix} \quad \text{and} [\Delta |V_2|] = -[B'']^{-1} \left[\frac{\Delta Q_2}{|V_2|} \right]$$

Or

$$\begin{bmatrix} \Delta\delta_2{}^{[k]} \\ \Delta\delta_3{}^{[k]} \end{bmatrix} = -[B']^{-1}\begin{bmatrix} \dfrac{\Delta P_2{}^{[k]}}{|V_2|^{[k-1]}} \\ \dfrac{\Delta P_3{}^{[k]}}{|V_3|^{[k-1]}} \end{bmatrix} \text{ and } \left[\Delta|V_2|^{[k]}\right] = -\left[B''\right]^{-1}\left[\dfrac{\Delta Q_2{}^{[k]}}{|V_2|^{[k-1]}}\right]$$

Iteration #1: assume $V_2{}^{[0]} = 1.00 \angle 0°$ and $V_3{}^{[0]} = 1.03 \angle 0°$.
The calculated quantities:

$$\begin{bmatrix} P_2{}^{[1]} \\ P_3{}^{[1]} \\ Q_2{}^{[1]} \end{bmatrix} = \begin{bmatrix} -0.5500 \\ 0.5665 \\ -1.8000 \end{bmatrix}$$

The mismatch power matrix:

$$\begin{bmatrix} \Delta P_2{}^{[1]} \\ \Delta P_3{}^{[1]} \\ \Delta Q_2{}^{[1]} \end{bmatrix} = \begin{bmatrix} -2 \\ 1.5 \\ -0.5 \end{bmatrix} - \begin{bmatrix} -0.5500 \\ 0.5665 \\ -1.8000 \end{bmatrix} = \begin{bmatrix} -1.4500 \\ 0.9335 \\ 1.3000 \end{bmatrix}$$

Calculation of δ_2 and δ_3:

$$\begin{bmatrix} \Delta\delta_2{}^{[1]} \\ \Delta\delta_3{}^{[1]} \end{bmatrix} = -[B']^{-1}\begin{bmatrix} \dfrac{\Delta P_2{}^{[1]}}{|V_2|^{[0]}} \\ \dfrac{\Delta P_3{}^{[1]}}{|V_3|^{[0]}} \end{bmatrix} = -\begin{bmatrix} -65 & 50 \\ 50 & -90 \end{bmatrix}^{-1}\begin{bmatrix} \dfrac{-1.4500}{1.00} \\ \dfrac{0.9335}{1.03} \end{bmatrix}$$

$$= \begin{bmatrix} -0.0254\ rad \\ -0.0041\ rad \end{bmatrix} = \begin{bmatrix} -1.4569° \\ -0.2324° \end{bmatrix}$$

$$\begin{bmatrix} \delta_2{}^{[1]} \\ \delta_3{}^{[1]} \end{bmatrix} = \begin{bmatrix} \delta_2{}^{[0]} \\ \delta_3{}^{[0]} \end{bmatrix} + \begin{bmatrix} \Delta\delta_2{}^{[1]} \\ \Delta\delta_3{}^{[1]} \end{bmatrix} = \begin{bmatrix} 0 \\ 0 \end{bmatrix} + \begin{bmatrix} -1.4569° \\ -0.2324° \end{bmatrix} = \begin{bmatrix} -1.4569° \\ -0.2324° \end{bmatrix}$$

Calculation of $|V_2|$:

$$\left[\Delta|V_2|^{[1]}\right] = -[-65]^{-1}\begin{bmatrix} \dfrac{1.3}{1.00} \end{bmatrix} = 0.0200$$

$$\left[\Delta|V_2|^{[1]}\right] = |V_2|^{[0]} + \Delta|V_2|^{[1]} = 1.00 + 0.0200 = 1.020\ pu$$

Iteration #2: considering $V_2{}^{[1]} = 1.020 \angle -1.4569°$ and $V_3{}^{[0]} = 1.03 \angle -0.2324°$.
The calculated quantities:

$$\begin{bmatrix} P_2{}^{[2]} \\ P_3{}^{[2]} \\ Q_2{}^{[2]} \end{bmatrix} = \begin{bmatrix} -1.6671 \\ 1.2133 \\ -0.0239 \end{bmatrix}$$

The mismatch power matrix:

$$\begin{bmatrix} \Delta P_2{}^{[2]} \\ \Delta P_3{}^{[2]} \\ \Delta Q_2{}^{[2]} \end{bmatrix} = \begin{bmatrix} -2 \\ 1.5 \\ -0.5 \end{bmatrix} - \begin{bmatrix} -1.6671 \\ 1.2133 \\ -0.0239 \end{bmatrix} = \begin{bmatrix} -0.3329 \\ 0.2867 \\ -0.4761 \end{bmatrix}$$

Calculation of δ_2 and δ_3:

$$\begin{bmatrix} \Delta\delta_2^{[2]} \\ \Delta\delta_3^{[2]} \end{bmatrix} = -[B']^{-1} \begin{bmatrix} \dfrac{\Delta P_2^{[2]}}{|V_2|^{[1]}} \\ \dfrac{\Delta P_3^{[2]}}{|V_3|^{[1]}} \end{bmatrix} = -\begin{bmatrix} -65 & 50 \\ 50 & -90 \end{bmatrix}^{-1} \begin{bmatrix} \dfrac{-0.3329}{1.02} \\ \dfrac{0.2867}{1.03} \end{bmatrix}$$

$$\begin{bmatrix} \Delta\delta_2^{[2]} \\ \Delta\delta_3^{[2]} \end{bmatrix} = \begin{bmatrix} -0.0046 \ rad \\ 0.0005 \ rad \end{bmatrix} = \begin{bmatrix} -0.0300° \\ 0.0286° \end{bmatrix}$$

$$\begin{bmatrix} \delta_2^{[2]} \\ \delta_3^{[2]} \end{bmatrix} = \begin{bmatrix} \delta_2^{[1]} \\ \delta_3^{[1]} \end{bmatrix} + \begin{bmatrix} \Delta\delta_2^{[2]} \\ \Delta\delta_3^{[2]} \end{bmatrix} = \begin{bmatrix} -1.4569° \\ -0.2324° \end{bmatrix} + \begin{bmatrix} -0.0300° \\ 0.0286° \end{bmatrix} = \begin{bmatrix} -1.7213° \\ -0.2021° \end{bmatrix}$$

Calculation of $|V_2|$:

$$\left[\Delta|V_2|^{[2]}\right] = -[-65]^{-1}\left[\dfrac{-0.4761}{1.02}\right] = -0.0072$$

$$\left[|V_2|^{[2]}\right] = |V_2|^{[1]} + \Delta|V_2|^{[2]} = 1.02 - 0.0072 = 1.0128 \ pu$$

The remaining five iterations are shown in **Table 4**. It shows that this method converges slower than Newton-Raphson method.

Iteration	$V_2^{[k]}$	$V_3^{[k]}$
1	$1.0200 \angle -1.4569°$	$1.03 \angle -0.2324°$
2	$1.0128 \angle -1.7213°$	$1.03 \angle -0.2021°$
3	$1.0111 \angle -1.6019°$	$1.03 \angle -0.2029°$
4	$1.0118 \angle -1.5759°$	$1.03 \angle -0.2026°$
5	$1.0119 \angle -1.5877°$	$1.03 \angle -0.2027°$

Table 4.
Fast-decoupled iterative solution.

6. DC power flow technique

DC power is an extension to the Fast-decoupled power flow formulation. In DC power flow method, the voltage is assumed constant at all buses; therefore, the $(\Delta|V|, \Delta Q)$ equation is neglected. The $(\Delta\delta, \Delta P)$ equation can be further simplified to a linear problem that does not require iterative solution:

$$-[B][\delta] = [P] \tag{32}$$

Or

$$[\delta] = -[B]^{-1}[P] \tag{33}$$

Example 5: DC power flow.
Solve the power flow problem shown in **Figure 3** using the DC power flow technique.

Solution:
The first step in DC power flow technique is obtaining $[B]$ from the Y-bus.

$$Y = \begin{bmatrix} 15 - j55 & -5 + j15 & -10 + j40 \\ -5 + j15 & 20 - j65 & -15 + j50 \\ -10 + j40 & -15 + j50 & 25 - j90 \end{bmatrix}$$

For this problem, Since the unknown voltage angles are δ_2 and δ_3, elements for $[B]$ are obtained from the Y-bus as follows:

$$[B] = \begin{bmatrix} -65 & 50 \\ 50 & -90 \end{bmatrix}$$

$$\begin{bmatrix} \delta_2 \\ \delta_3 \end{bmatrix} = -\begin{bmatrix} -65 & 50 \\ 50 & -90 \end{bmatrix}^{-1} \begin{bmatrix} P_2 \\ P_3 \end{bmatrix} = -\begin{bmatrix} -65 & 50 \\ 50 & -90 \end{bmatrix}^{-1} \begin{bmatrix} -2 \\ 1.5 \end{bmatrix}$$

$$= \begin{bmatrix} -0.0313 \; rad \\ -0.0007 \; rad \end{bmatrix} = \begin{bmatrix} -1.7958° \\ -0.0428° \end{bmatrix}$$

7. Slack bus power and losses calculations

The main objective of power flow calculations is to determine the voltages (magnitude and angle) for a given load and generation conditions. Once voltages are known for all buses, slack bus power, as well as line flows and losses, can be calculated. The slack bus real and reactive power are calculated using Eqs. (4) and (5), respectively. Overall system losses are the difference between generation and load.

$$S_L = S_{Gen} - S_{Load} \tag{34}$$

Specific branch losses are calculated using branch power flow. For example, the losses in the line $i - j$ are the algebraic sum of the power flow.

$$S_{L \; ij} = S_{ij} + S_{ji} \tag{35}$$

S_{ij} and S_{ji} are defined as follows:

$$S_{ij} = V_i \, I_{ij}{}^* \tag{36}$$

$$S_{ji} = V_j \, I_{ji}{}^* \tag{37}$$

The current between buses I_{ij} is a function of the voltages and the admittance between V_i and V_j. It is worth noting that $I_{ji} = -I_{ij}$

$$I_{ij} = (V_i - V_j) y_{ij} \tag{38}$$

Example 6: Slack bus power and losses.
For the 3-bus system shown in **Figure 3**, the voltages at buses 2 and 3 were iteratively calculated: $V_1 = 1.02 \angle 0°$, $V_2 = 1.0118 \angle -1.5871°$ and $V_3 = 1.03 \angle -0.2005°$

a. Calculate the slack bus power.

b. Calculate the total system losses.

c. Calculate individual branch losses.

Solution:
The polar form of the Y-bus is used.

$$Y = \begin{bmatrix} 57.01 \angle -74.74^{\circ} & 15.81 \angle 108.43^{\circ} & 41.23 \angle 104.04^{\circ} \\ 15.81 \angle 108.43^{\circ} & 68.01 \angle -72.90^{\circ} & 52.20 \angle 106.70^{\circ} \\ 41.23 \angle 104.04^{\circ} & 52.20 \angle 106.70^{\circ} & 93.41 \angle -74.48^{\circ} \end{bmatrix}$$

a. The slack bus power

The slack bus power can be calculated using real and reactive power equations:

$$P_1 = \sum_{j=1}^{n} |V_1||V_j||Y_{1j}| \cos\left(\theta_{1j} - \delta_1 + \delta_j\right)$$

$$= |V_1|^2 |Y_{11}| \cos(\theta_{11}) + |V_1||V_2||Y_{12}| \cos(\theta_{12} - \delta_1 + \delta_2) + |V_1||V_3||Y_{13}| \cos(\theta_{13} - \delta_1 + \delta_3)$$

$$= 0.5195 \, pu$$

$$Q_1 = -\sum_{j=1}^{n} |V_1||V_j||Y_{1j}| \sin\left(\theta_{1j} - \delta_1 + \delta_j\right)$$

$$= -|V_1|^2 |Y_{11}| \sin(\theta_{11}) - |V_1||V_2||Y_{12}| \cos(\theta_{12} - \delta_1 + \delta_2) - |V_1||V_3||Y_{13}| \sin(\theta_{13} - \delta_1 + \delta_3)$$

$$= -0.4572 \, pu$$

b. The total system losses

The total real power losses can be calculated using the total net injected real a power at all buses:

$$P_L = P_1 + P_2 + P_3$$

$$P_L = P_1 + P_2 + P_3 = 0.5195 - 2 + 1.5 = 0.0195 \, pu$$

Similarly, the reactive power losses can be calculated.

$$Q_L = Q_1 + Q_2 + Q_3$$

However, Q_3 is unknown and can be calculated based on the given bus voltages:

$$Q_3 = -\sum_{j=1}^{n} |V_3||V_j||Y_{3j}| \sin\left(\theta_{3j} - \delta_3 + \delta_j\right)$$

$$= -|V_3||V_1||Y_{31}| \sin(\theta_{31} - \delta_3 + \delta_1) - |V_3||V_2||Y_{32}| \sin(\theta_{32} - \delta_3 + \delta_2) - |V_3|^2 |Y_{33}| \sin(\theta_{33})$$

$$= 1.0220 \, pu$$

Once Q_2 is calculated, the total reactive power losses are calculated:

$$Q_L = Q_1 + Q_2 + Q_3 = -0.4572 - 0.5 + 1.0220 = 0.0648 \, pu$$
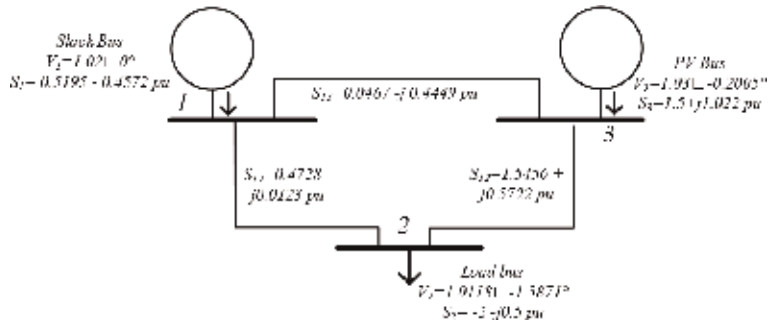
Figure 6.
Power flow results.

c. Branch losses

To calculate the losses in line 1–2, $S_{L\,12}$ is calculated by summing S_{12} and S_{21}. These flows are calculated as follows: $S_{12} = V_1\,I_{12}{}^*$ and $S_{21} = V_2\,I_{21}{}^*$

$$I_{12} = (V_1 - V_2)y_{12} = (1.02 \angle 0° - 1.0118 \angle -1.5871°)(-5 + j15) = 0.4635 + j0.0121\,pu$$

$$I_{21} = (V_2 - V_1)y_{21} = -I_{12} = -0.4635 - j0.0121\,pu$$

$$S_{12} = V_1\,I_{12}{}^* = 1.02 \angle 0° \times (0.4635 - j0.0121) = 0.4728 - j\,0.0123\,pu$$

$$S_{21} = V_2\,I_{21}{}^* = 1.0118 \angle -1.5871° \times (-0.4635 + j0.0121) = -0.4685 + j0.0252\,pu$$

$$S_{L\,12} = S_{12} + S_{12} = (0.4728 - j\,0.0123) + (-0.4685 + j0.0252) = 0.0043 + j0.0129pu$$

Similarly, power flow and losses in other branches are calculated.
Line 1–3:

$$S_{31} = -0.0456 + j0.4494$$

$$S_{13} = 0.0467 - j\,0.4449$$

$$S_{L\,13} = 0.0011 + j\,0.0045$$

Line 2–3:

$$S_{23} = -1.5315 - j0.5252$$

$$S_{32} = 1.5456 + j0.5722$$

$$S_{L\,23} = 0.0141 + j\,0.0470$$

Total losses:

$$S_L = S_{L\,13} + S_{L\,23} + S_{L\,12} = 0.0195 + j0.0648\,pu$$

The generation and load at different buses is shown in **Figure 6**.

8. Conclusions

Power flow analysis, or load flow analysis, has a wide range of applications in power systems operation and planning. This chapter presents an overview of the power flow problem, its formulation as well as different solution methods. The

power flow model of a power system can be built using the relevant network, load, and generation data. Outputs of the power flow model include voltages (magnitude and angles) at different buses. Once nodal voltages are calculated, real and reactive power flows in different network branches can be calculated. The calculation of branch power flows enables technical loss calculation in different network branches, as well as the total system technical losses.

Power flow analysis is performed by solving nodal power balance equations. Since these equations are nonlinear, iterative techniques such as the Gauss-Seidel, the Newton-Raphson, and the fast-decoupled power flow methods are commonly used to solve this problem. In general, the Gauss-Seidel method is simple but converges slower than the Newton-Raphson method. However, the latter method required the Jacobian matrix formation of at every iteration. The fast-decoupled power flow method is a simplified version of the Newton-Raphson method. This simplification is achieved in two steps: 1) decoupling real and reactive power calculations; 2) obtaining of the Jacobian matrix elements directly from the Y-bus matrix. The DC power method is an extension to the fast-decoupled power flow formulation. In DC power flow method, the voltage is assumed constant at all buses and the problem becomes linear.

Acknowledgements

Author details

Mohammed Albadi
Sultan Qaboos University, Muscat, Oman

*Address all correspondence to: mbadi@squ.edu.om

IntechOpen

References

[1] Bergen AR. Power Systems Analysis. Delhi, India: Pearson Education India; 2009

[2] Glover JD, Sarma MS. Power System Analysis and Design: With Personal Computer Applications. Toronto, ON, Canada: International Thomson Publishing Company; 1994

[3] Glover JD, Sarma MS, Overbye T. Power System Analysis & Design, SI Version. Noida, India: Cengage Learning; 2012

[4] Grainger JJ, Stevenson WD, Stevenson WD. Power System Analysis. New York, USA; 2003

[5] Gross CA. Power System Analysis. Vol. 1. New York: Wiley; 1986

[6] Saadat H. Power System Analysis. Vol. 232. Singapore: WCB/McGraw-Hill; 1999

Chapter 6

Modeling Emerging Semiconductor Devices for Circuit Simulation

Md Sakib Hasan, Mst Shamim Ara Shawkat, Sherif Amer,
Syed Kamrul Islam, Nicole McFarlane and Garrett S. Rose

Abstract

Circuit simulation is an indispensable part of modern IC design. The significant cost of fabrication has driven researchers to verify the chip functionality through simulation before submitting the design for final fabrication. With the impending end of Moore's Law, researchers all over the world are looking for new devices with enhanced functionality. A plethora of promising emerging devices has been proposed in recent years. In order to leverage the full potential of such devices, circuit designers need fast, reliable models for SPICE simulation to explore different applications. Most of these new devices have complex underlying physical mechanism rendering the model development an extremely challenging task. For the models to be of practical use, they have to enable fast and accurate simulation that rules out the possibility of numerically solving a system of partial differential equations to arrive at a solution. In this chapter, we show how different modeling approaches can be used to simulate three emerging semiconductor devices namely, silicon- on-insulator four gate transistor(G^4FET), perimeter gated single photon avalanche diode (PG-SPAD) and insulator-metal transistor (IMT) device with volatile memristance. All the models have been verified against experimental /TCAD data and implemented in commercial circuit simulator.

Keywords: silicon-on-insulator (SOI), multiple-gate transistor, G^4FET, semiconductor device, spline interpolation, macromodel, silicon photomultiplier, single photon avalanche diode, circuit design, insulator metal transition, IMT, compact model, SPICE, neuron, Mott transition

1. Introduction

Circuit simulation is an indispensable part of modern IC design. The significant cost of fabrication has driven researchers to verify the chip functionality through simulation before submitting the design for final fabrication. With the impending end of Moore's Law, researchers all over the world are now looking for new devices with enhanced functionality and a plethora of promising emerging devices has been proposed in recent years. To leverage the full potential of such devices, circuit designers need fast, reliable models for SPICE simulation to explore different applications. Most of these new devices have complex underlying physical mechanism rendering the model development an extremely challenging task. To be of practical

use, the model has to enable fast and accurate simulation, which rules out the possibility of numerically solving differential equations underlying the physics of semiconductor devices to arrive at a solution. In this chapter, we show how different approaches can be adopted to model three emerging semiconductor devices, namely silicon-on-insulator four-gate transistor (G^4FET), single-photon avalanche diode (SPAD), and insulator-metal transistor (IMT) device with volatile memristance.

2. Background

The amazing technological advancements in the semiconductor industries during last 60 years have largely shaped the modern world we live in. However, bulk silicon devices are now faced with some fundamental physical limits and innovative researchers and scientists all over the world have been diligently exploring new devices and computing paradigms to continue the breathtaking pace of technology advancement. The widespread use of a technology in circuit design is heavily dependent upon good SPICE models for CAD (computer-aided design) tools that are now ubiquitous in circuit design. Sophisticated models for existing semiconductor devices integrated with CAD tools have enabled designers worldwide to design innovative and reliable circuits which are in a large part responsible for the technology boom of the last several decades. In this chapter, we will be discussing three relatively new devices highlighting the works and challenges involved in model development and SPICE simulation.

The first device is SOI (silicon-on-insulator) four-gate transistor known as G^4FET. Here, we outline its operating mechanism, different approaches towards modeling and highlight two particular approaches, namely multivariate cubic spine interpolation model and MOS-JFET macromodel. The second device is a single photon avalanche diode (SPAD). We review and discuss the most recent developments in SPAD modeling with particular emphasis on a new class of SPAD known as PGSPAD (perimeter gated SPAD). The third device is insulator metal transition (IMT) device. Here, we focus on a very recent IMT model to demonstrate how proper simplification of device physics can lead to a suitable SPICE model facilitating circuit design.

3. Silicon-on-insulator (SOI) four gate field effect transistor (G^4FET)

G^4FET was first reported in 2002 [1]. It has four independent gates, two of which provide vertical MOS (metal-oxide-semiconductor) field-effect action whereas the other two gates provide lateral junction field effect transistor (JFET) functionality. The unique G^4FET structure can be leveraged to design circuits for different analog, mixed-signal and digital applications with significantly reduced transistor counts. Some of these have already been experimentally demonstrated including LC oscillators and Schmitt trigger circuit with adjustable hysteresis using negative differential resistance [2], four quadrant analog multipliers [3], adjustable threshold inverters, real time reconfigurable logic gates and DRAM cell [4], and universal and programmable logic gate capable of highly efficient full adder design [5]. G^4FET inspired multiple state electrostatically formed nanowires have already been used for threshold logic functions [6] and high-sensitivity gas sensing [7]. Another potential application is to leverage the tunable tent map shape characteristics of the voltage controlled G^4NDR circuit [2] to build chaotic logic gates for hardware security applications [8, 9].

3.1 Device structure

One particular advantage of G^{4}FET is that standard SOI process without significant modification can be used to fabricate these devices. The carrier conduction through the channel is modulated using four independent gates. The conventional source and gates become junction gates (JG1 and JG2) to provide lateral JFET functionality and the top and bottom gates provide vertical MOS functionality. **Figure 1** shows the 3-D schematic structure of a *p*-channel G^{4}FET. It is evident that no specialized fabrication procedure is necessary for this device.

3.2 Conduction mechanism

By putting two highly doped body contacts on the opposite sides of the traditional channel, we can convert a conventional *n*-channel SOI MOSFET into a *p*-channel G^{4}FET. What used to be $n +$ doped source and drain now act as lateral JFET-like gates. These gates can modulate the width of the conduction channel according to applied bias. The functionality of the conventional MOS gate is achieved through the top oxide gate. The substrate along the buried oxide provides an additional bottom-gate functionality. A high positive voltage on top gate creates an inversion layer of electrons near the top surface. As we reduce the top gate voltage, the top surface gradually changes from inversion to depletion, and eventually, with high negative voltage, it will enter the accumulation region. Similar effect due to bottom-gate can be observed for the surface near the buried oxide interface. In order to ensure ohmic contact with the conducting channel, body contacts on the opposite side of the channel are highly doped. Through this process, an inversion-mode, *n*-channel MOSFET can be transformed into an accumulation/depletion-mode *p*-channel G^{4}FET. A similar mirror transformation will convert a classic SOI *p*-channel MOSFET into an *n*-channel G^{4}FET. The current from drain to source follows in a direction perpendicular to a traditional MOSFET. Similarly, the geometrical features are also swapped, i.e., the length and width of the classic MOSFET now become the width and length of the new G^{4}FET, respectively. As outlined here, there are three possible paths for current conduction, namely (1) top surface near gate oxide interface, mostly controlled by top gate bias, (2) bottom surface near
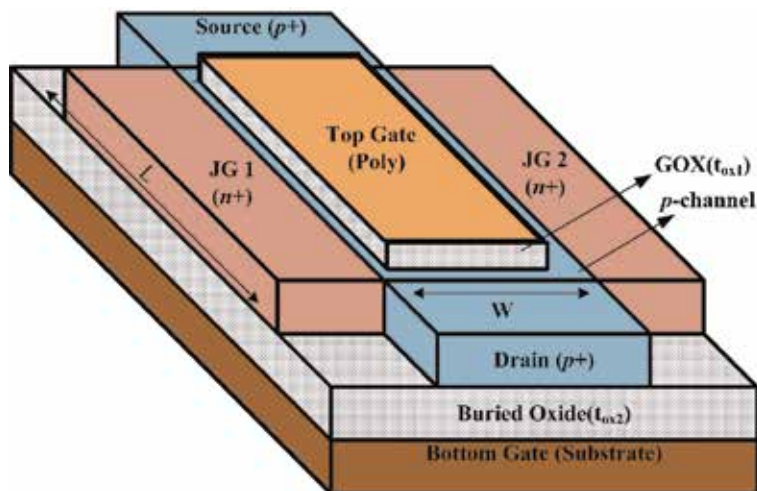

Figure 1.
Schematic device structure of a p-channel G^{4}FET.

buried oxide interface, mostly controlled by bottom gate bias, and (3) volume conduction away from vertical oxide interfaces, mostly controlled by lateral gates.

3.3 State-of-the-art G^{4}FET models

Different approaches have been adopted to understand and model the operation of G^{4}FET. Extraction methods for threshold voltage, mobility, and subthreshold swing in the linear region were demonstrated in [10]. The experimental results from a partially-depleted (PD)-SOI G^{4}FET showed the dependence of these parameters on different gate biases. The charge coupling between front, back, and lateral junction-gates was considered and a 2-D analytical relationship for the fully-depleted body potential was derived in [11]. Here, a closed form front-interface threshold voltage expression was derived as a function of the back and the lateral gate voltages for different back interface conditions such as accumulation, depletion and inversion.

A very interesting application of G^{4}FET is the formation of quantum wire. The quantum wire can be electrostatically formed when the conducting channel is surrounded by depletion regions induced by vertical MOS and lateral JFET gates [12]. In this unique conduction mechanism named depletion-all-around (DAA), majority carriers flow in the volume of the silicon film far from the silicon/oxide interfaces. The control of lateral gates on the conduction channel can be adjusted by changing biases on the vertical gates. There is a reduced sensitivity of the channel to the oxide and interface defects, low subthreshold swing, high g_m/I_D ratio, high mobility, low noise, and high immunity to ionizing radiation [13]. A low frequency noise model combining volume and surface noise sources was presented in [14] and effects of gate oxide and junction nonuniformity on the DC and low-frequency noise performance were investigated in [15].

A charge sheet model has been proposed to analyze the transistor characteristics of fully-depleted G^{4}FETs [16]. Here, surface accumulation behavior, drain current and gate capacitance of fully-depleted G^{4}FET are modeled analytically. In [17], a mathematical model is developed to determine the subthreshold swing of thin-film fully-depleted G^{4}FET. Based on the exact solution of the Poisson equation, a new two-dimensional model of potential and threshold voltage for the fully-depleted G^{4}FET was developed in [18]. Another mathematical model is developed in [19] to determine the 3-D potential distribution of a fully-depleted G^{4}FET.

Several numerical methods have also been used for modeling G^{4}FET. Multidimensional Lagrange and Bernstein polynomial approaches have been used in [20] for modeling and SPICE implementation. The authors in [21] have reported single multivariate regression polynomial approach for modeling the device operation across different operating regimes. We will focus on two new techniques in the next two sections. The first one is based on multivariate cubic spline interpolation method for DC modeling first reported in [22]. The second one is a MOS-JFET macromodel suitable for DC, AC and transient simulation [23].

3.4 Multivariate cubic spline interpolation model

Developing a interpolating polynomial $f(x)$ requires fitting a polynomial to a set of chosen data points such as (x_0, y_0), (x_1, y_1) ... (x_m, y_m). It can be written as,

$$y_i = f(x_i); i = 1, 2, ..., m \qquad (1)$$

Spline based interpolating polynomial is a piecewise low-degree polynomial which solves some of the problems associated with a single high degree interpolant.

If the dataset is regular and monotonic, this interpolation method can get rid of an important problem of single high degree interpolating polynomial known as Runge's phenomenon, i.e., oscillation between interpolation nodes, which can be catastrophic close to the boundary. With the suitable choice of spline, it is also possible to reduce error while maintain continuity of the function and its first and second order derivatives. For these reasons, multivariate cubic spline polynomials are used for the model development [24].

Given n data points, (x_k, y_k), $k = 1, 2,..., n$ with distinct x_k's, there is a unique polynomial in x of degree less than n whose graph passes through the points. If two successive points are (x_k, y_k) and (x_{k+1}, y_{k+1}) then the kth interval between these two points can be interpolated using splines. The interval index k is such that, $x_k \leq x < x_{k+1}$. The local variable, s is $s = x - x_k$. The first divided difference is $\delta_k = (y_{k+1} - y_k)/(x_{k+1} - x_k)$. Let h_k denote the length of kth subinterval, i.e., $h_k = x_{k+1} - x_k$; then, $\delta_k = (y_{k+1} - y_k)/h_k$. Let d_k denote the slope of the interpolant at x_k, i.e., $d_k = P'(x_k)$. The cubic spline polynomial will be the following function on the interval $x_k \leq x \leq x_{k+1}$, written in terms of local variables $s = x - x_k$ and $h = h_k$.

$$P(x) = \frac{3hs^2 - 2s^3}{h^3}y_{k+1} + \frac{h^3 - 3hs^2 + 2s^3}{h^3}y_k + \frac{s^2(s-h)}{h^2}d_{k+1} + \frac{s(s-h)^2}{h^2}d_k \quad (2)$$

The cubic polynomial in Eq. (2) satisfies four conditions for smooth interpolation; two on the function values and two on the derivative values so that,

$$P(x_k) = y_k, \ P(x_{k+1}) = y_{k+1}, \ P'(x_k) = d_k, \ P'(x_{k+1}) = d_{k+1}$$

In order to ensure continuous second derivative, we can add an extra constraint which gives rise to the following equation,

$$h_k d_{k-1} + 2(h_{k-1} + h_k)d_k + h_{k-1}d_{k+1} = 3(h_k \delta_{k-1} + h_{k-1}\delta_k) \quad (3)$$

If knots are equally spaced, Eq. (4) becomes

$$d_{k-1} + 4d_k + d_{k+1} = 3\delta_{k-1} + 3\delta_k \quad (4)$$

Following the above-mentioned procedure at every interior knot x_k ($k = 2,..., n - 1$), results in $n - 2$ equations with n unknown d_k's. At the interval boundary, "not-a-knot" method is used, i.e., a single cubic polynomial is used on first two subintervals, $x_1 \leq x \leq x_3$, and last two subintervals, $x_{n-2} \leq x \leq x_n$. Now, these two boundary conditions give two more equations resulting in n unknowns with n linear equations. Then d_k's are estimated by solving this system of linear algebraic equations.

For cases involving multiple independent variables, tensor product formulation can be used to extend the univariate analysis to multiple dimensions. In each respective dimension, value at a desired point is interpolated according to a cubic interpolation of the values at nearby knot points. In this section, we are using V_{DS} (drain-source voltage), V_{JG} (common junction-gate voltage), V_{TG} (top-gate voltage) and V_{BG} (bottom-gate voltage) as our independent variables for spline interpolation of drain current. Moreover, the geometric features such as W (width) and L (length) may be used as independent variables to include the effect of device geometry.

An n-channel partially-depleted SOI (PDSOI) G^{4}FET was developed in a device simulator (TCAD Sentaurus from Synopsys) and a cubic spline model was formulated based on the generated data. In **Figure 2**, drain current versus drain voltage is
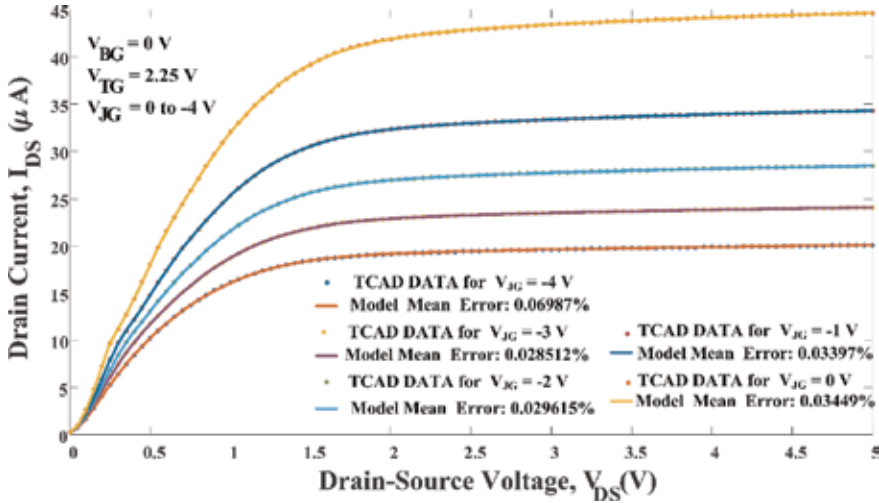
Figure 2.
Comparison between isolines of test data and cubic spline model for different junction-gate voltages ranging from −4 V to 0 V in 1 V increment arranged from bottom to top [22].

plotted for different values of junction-gate voltages ranging from 0 to −4 V. The bottom gate/substrate bias, V_{BG} is 0 V and top-gate bias, V_{TG} is 2.25 V, respectively. Both junction gates are tied together for simplicity. From the graph and the values of corresponding mean relative error, it is clear that the model fits reasonably well for all the isolines. More details on this method can be found in [22].

3.5 MOS-JFET macromodel

G^{4}FET has also been called MOSJFET [1] since it combines both metal-oxide-semiconductor field-effect transistor (MOSFET) and junction field-effect transistor (JFET) actions in a single silicon island. As mentioned earlier, the vertical gates provide MOS functionality and the lateral gates add JFET functionality. By applying different junction-gate biases, it is possible to modulate the threshold voltages of top- and bottom-gates. As a result, G^{4}FET can be thought of as a combination of two MOSFETs primarily responsible for top and bottom surface conduction and a dual-gate JFET that is primarily responsible for volume conduction. The top-gate threshold voltage is V_{TH} and the bottom-gate voltage causing the onset of accumulation and inversion at the bottom-gate are V_{BG}^{acc} and V_{BG}^{inv}, respectively. Some of the terms used in the model are introduced below:

Junction-gate, top gate and bottom gate capacitances are $C_{JG} = \varepsilon_{Si}/w$, $C_{ox1} = \varepsilon_{ox}/t_{ox1}$ and $C_{ox2} = \varepsilon_{ox}/t_{ox2}$, respectively. Three constants based on device geometry, α, β and γ are defined as, $\alpha = \frac{2\sqrt{2}}{\tanh\left(\frac{2\sqrt{2}t_{Si}}{W}\right)}$, $\beta = \frac{rC_{JG}/C_{ox1}}{1+\alpha C_{JG}/C_{ox2}}$, $\gamma = \frac{2\sqrt{2}}{\sinh\left(\frac{2\sqrt{2}t_{Si}}{W}\right)}$.

Other terms include $\varphi_F = -V_T \ln\left(\frac{N_d}{n_i}\right)$, $\varphi_b = \frac{E_g}{2} + V_T \ln\left(\frac{N_d}{n_i}\right)$, $V_P = \varphi_b - \frac{qN_d W^2}{8\varepsilon_{Si}}$.

Here, W = width of the transistor, t_{si} = silicon film thickness, t_{ox1} = top oxide thickness, t_{ox2} = buried oxide thickness, $V_T = kT/q$ is the thermal voltage, N_d = donor concentration in the body, n_i = intrinsic carrier concentration, ε_{si} = permittivity of silicon, and ε_{ox} = permittivity of silicon dioxide.

The onset voltage of accumulation and inversion for the bottom-gate, V_{BG}^{acc} and V_{BG}^{inv}, can be expressed [27] as,

$$V_{BG}^{acc} = V_{FB2} + (\gamma - \alpha)\frac{C_{JG}}{C_{ox2}}(V_{JG} - V_P) \tag{5}$$

$$V_{BG}^{inv} = V_{FB2} + \left(1 + \alpha\frac{C_{JG}}{C_{ox2}}\right)2\varphi_F - (\gamma - \alpha)\frac{C_{JG}}{C_{ox2}}(V_P) + (1 + \gamma C_{JG}/C_{ox2})V_{JG} \tag{6}$$

The back gate may be accumulated, depleted or inverted. When the bottom-gate is in inversion, i.e., $V_{BG} < V_{BG}^{inv}$,

$$V_{TH} = V_{FB1} - \gamma\left(\frac{C_{JG}}{C_{ox1}}\right)(2\varphi_F + V_P) - \alpha\left(\frac{C_{JG}}{C_{ox1}}\right)(V_{JG} - V_P) \tag{7}$$

When the bottom-gate is depleted, i.e., $V_{BG}^{inv} < V_{BG} < V_{BG}^{acc}$,

$$V_{TH} = V_{FB1} - \beta(V_{BG} - V_{FB2}) + (\gamma - \alpha)\left(\frac{C_{JG}}{C_{ox1}} + \beta\frac{C_{JG}}{C_{ox1}}\right)(V_{JG} - V_P) \tag{8}$$

When the bottom-gate is in accumulation, i.e., $V_{BG} > V_{BG}^{acc}$,

$$V_{TH} = V_{FB1} + (\gamma - \alpha)\left(\frac{C_{JG}}{C_{ox1}}\right)(V_{JG} - V_P) \tag{9}$$

Here, V_{FB1} and V_{FB2} are the flat band voltages of the top-gate and the bottom gates, respectively.

Based on the above relationships among different gates, a macromodel subcircuit is created combining conventional SPICE Level-1 MOSFET and the JFET models which follow from the quadratic FET model of Schichman and Hodges [25]. It should be noted that the model can be improved by using higher-level MOSFET models (Level-2/3) and BSIM/BSIMSOI models for devices with deep submicron geometry. Here, the goal of this work, with simple first order MOSFET and JFET models, is to show the feasibility of the macromodel and demonstrates how it can capture the essential physics underlying the complex interaction between multiple gates. Here, the top conduction is modeled using a MOSFET and the volume conduction is modeled using a JFET. However, instead of a constant threshold MOSFET, the subcircuit allows for threshold voltage modification based on multiple gate biases using the relationship described above. The transient simulation results for the first analog multiplier circuit configuration in [3] is shown in **Figure 3**. The simulation result using the macromodel shows good matching with the experimental result [3].
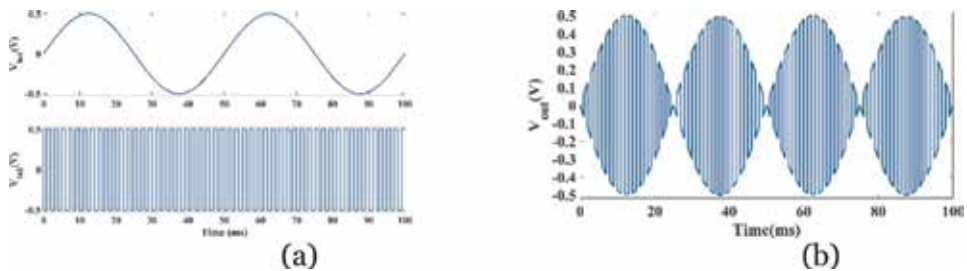

Figure 3.
Transient simulation results for product of a 20 Hz, 1 V_{p-p} sinusoidal-wave with 500 Hz, 1 V_{p-p} square-wave (W = 0.3 μm × 10, L = 2.4 μm, V_{DD} = 3.5 V, V_{SS} = −3.5 V, I_{bias} = 35 μA, V_{bias1} = 2 V, V_{bias2} = −2.5 V, R_L = 100 kΩ) using analog multiplier; (a) input, (b) output [3].

4. Single photon avalanche diode (SPAD)

Single photon avalanche diodes (SPADs) based optical detectors have gained interest for use in a wide range of applications such as biochemical analysis, imaging and light ranging applications [26–32]. The main causes of the increased popularity are the exceptional level of miniaturization and portability, overall high performance and low costs due to the integration of SPADs with mixed-signal readout circuits in standard complementary metal-oxide-semiconductor (CMOS) technology [26–32]. The capability to detect single photon and provide sub-nanosecond time resolution along with the low-power and high-speed CMOS read-out circuits have made SPADs superior to other optical detectors in high performance weak optical signal detection applications. In order to correctly simulate the behavior of the SPAD device and the performance of its readout circuit during the design phase, a suitable and comprehensive model of the SPAD is required. In this work, we review and discuss the most recent developments in SPAD modeling to predict the real behavior of the CMOS SPAD systems before fabrication reducing the design cycle.

4.1 SPAD theory and operation

A single photon avalanche diode (SPAD) is a *p-n* junction, which is biased above the breakdown voltage. The device operates in the so-called Geiger mode. With the increase of reverse bias voltage beyond a critical potential, the current increases rapidly. The rapid increase in current is due to the free carriers, which have gained enough energy to ionize the fixed lattice atoms and free other carriers through high-energy collisions. This rapid multiplication process results in a sudden large avalanche current. The reverse voltage above which this multiplication process occurs is called breakdown voltage [26–32]. In order to respond to an incident photon, impact ionization is necessary for a SPAD. A high electric field is required to break the covalent bonds and generate the free carriers, which take part in the avalanche process. The probability that carriers gain the threshold energy is a function of the local electric field and previous states of the carrier. This probability determines the ionization rates. **Figure 4** illustrates impact ionization causing an avalanche current in the presence of a high electric field. A number of free carriers is generated at each step, quickly multiplying and generating a large current [10].

Free carriers are also generated in absence of photon due to inherent noise processes such as thermal generation, minority carrier diffusion, and band-to-band
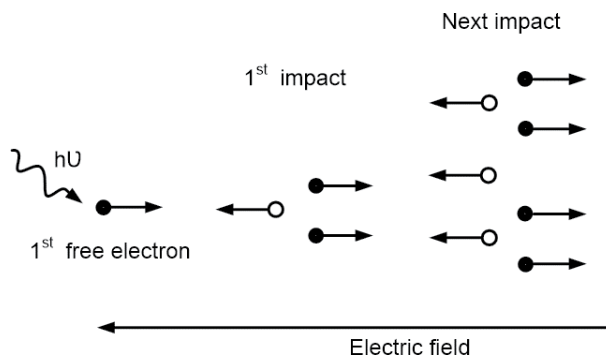

Figure 4.
Impact ionization causing avalanche current in existence of high electric field where a number of free carriers are multiplied in each step.

tunneling. Dark count rate is the effective noise for SPADs caused by these non-photon driven carrier generations. The large avalanche current must be quenched to protect the long-term use of the device. An external circuit, typically a passive ballast resistor or a transistor, is employed to quench the large avalanche current. As the current increases the voltage drop across the quenching resistor increases. As a result, the bias voltage across the SPAD reduces below the break-down voltage ending the avalanche process. The SPAD is then recharged and ready to detect photon event induced avalanche. The avalanche gain is large enough to be almost infinite in this Geiger mode of operation. The generation of an electron-hole pairs causes the device to be in an "ON" or "OFF" state. Since the generation of an avalanche gives a current or voltage spike, the device exhibits an inherently digital operation [26–32]. **Figure 5** shows the Geiger mode operation of SPAD and quenching of the avalanche current. Here, V_{br} represents the breakdown voltage and V_s is the applied voltage. During the current flow, some carriers may be trapped in the deep-levels and are released after a characteristics lifetime later. The released carrier may trigger a new avalanche process when the SPAD is ready to detect another photon. The new avalanche process associated with trapped carriers during the first avalanche pulse causes after-pulses and it reduces detector performance [26].

SPADs fabricated in CMOS provides the benefits of commercial CMOS process such as low cost, miniaturization, and improved performance [27–32]. However, due to the planar nature of the junction in standard CMOS process, electric field distributions exhibit maxima at the diodes' edge [27–32]. Since SPADs operate in a high reverse bias region, they are more vulnerable to breakdown at the edges. Therefore, full volumetric breakdown cannot be achieved as the diode periphery undergoes breakdown earlier compared to the other parts of the diode. As a result, the active area is decreased and the photon detection efficiency is significantly compromised. This premature breakdown is one of the major problems of SPADs implemented in standard CMOS process [27–32]. It has been previously proved that the perimeter gated SPAD (PGSPAD), a *p-n* junction incorporating a poly-silicon gate surrounding the periphery, suppresses the premature breakdown effectively [29, 31, 33–39]. The applied voltage at the gate terminal modulates the electric field making it uniform throughout the junction preventing the premature breakdown.

4.2 State-of-the-art SPAD models

Various SPAD models have been presented in literature to predict the actual behavior and choose suitable parameters during the design phase to ensure the
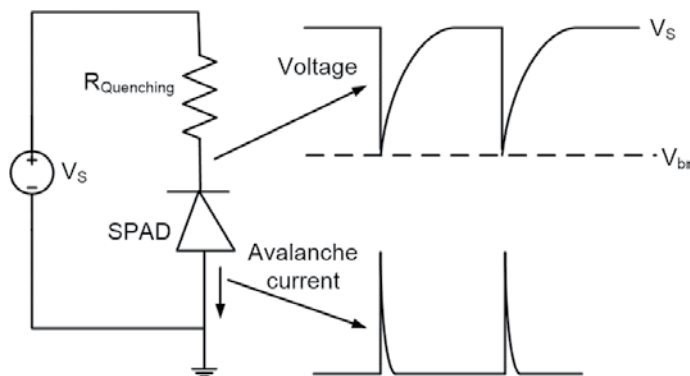

Figure 5.
Geiger mode operation of SPAD; the avalanche current is quenched using a quenching resistor.

optimal performance for CMOS SPAD systems in existing and new applications [29, 35–47]. State of the art SPAD modeling approaches can be grouped in three sub groups named as model based on device physics, circuit simulation model, and model based on information theory. The main features of the models of each group along with the limitations are discussed below.

4.2.1 Models based on device physics

The SPAD models in this group have been developed to simulate the SPADs at the semiconductor level based on purely quantum mechanical or semi-classical representation of the transport properties of semiconductor structure underlying the SPAD device [29, 35–37]. The key operational features such as breakdown voltage, avalanche gain, and noise have been generated through the model.

In [35], a new compact numerical model to simulate the forward and reverse dc diode characteristics has been presented. The model is based on the solution of 1D steady-state hole continuity equation in the depletion layer of a *p-n* junction. The developed dc model includes the physical mechanisms such as band-to-band tunneling, trap-assisted tunneling, Shockley-Read-Hall recombination, and avalanche breakdown.

The model presented in [36], focuses on breakdown state stability studying the SPAD transient behavior based on physical and numerical approach. At first, the spatial steady-state free charge carrier distribution during breakdown is computed. Then the temporal change of the distribution is considered. It explores the dependence of the probability for the avalanche process on the quenching resistance. It aids designers to accurately choose the optimal passive quenching resistance for minimizing the overall dead time value.

The reported model in [37] investigates the lateral spreading of the avalanche in Geiger mode reach-through avalanche photo diode, which is the main cause of avalanche dynamics and the time jitter. The model estimates the photon assisted effect based on the Poisson equation and the time-dependent semiconductor continuity equation to ensure the avalanche dynamics. A Monte Carlo simulation of the avalanche current rise has been developed in the model.

The effect of structural effect on the breakdown voltage and the localization of the avalanche region within p+/n-well junction was determined in model [29]. The reported 2-D numerical model is based on Poisson, hole and electron current continuity equation coupled with carrier generation rate equation due to impact ionization. The model highlights the regions most susceptible to breakdown through the determination of the spatial maxima of carrier generation rates and establishes that the generation rate reaches its peak at the perimeter and the surface of the junction causing perimeter breakdown. Finally, it demonstrates that full volumetric breakdown can be achieved using perimeter breakdown suppression techniques.

4.2.2 Circuit simulation model

Circuit simulation models aim to represent the equivalent circuit representation of the SPAD for circuit level designs and simulation. These models provide a first order estimation of performance at the circuit level and allow simulation of readout circuits based on the electrical characteristics of SPAD [31, 33, 38–41]. The readout delays, time constant for both quenching and reset can be calculated using the circuit simulation model.

Traditional SPAD basic model reported in [38] includes voltage sources, resistors and capacitors to represent the diode characteristics (**Figure 6**). In the model, the diode resistance, R_D, includes both space charge resistance and resistance of neutral
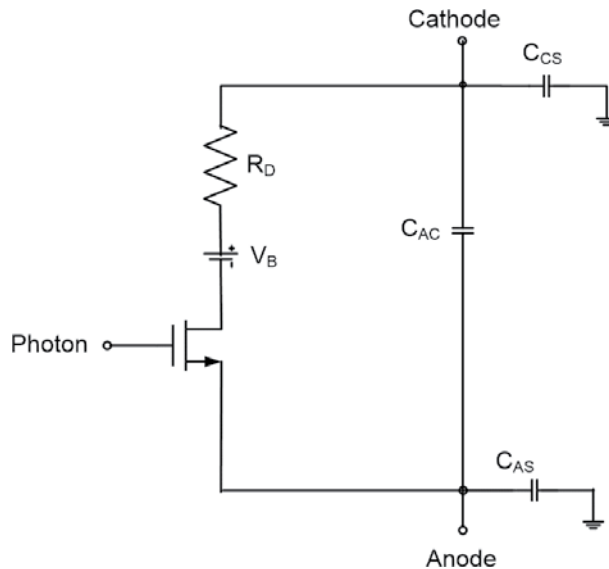
Figure 6.
Traditional SPAD basic model where closing the transistor switch imitates the avalanche triggering [38].

regions crossed by the avalanche current. C_{AC} represents the junction capacitance and C_{AS} and C_{CS} represents the stray capacitances from anode and cathode respectively. The closure of NMOS switch simulates the triggering of an avalanche due to photon absorption or other phenomenon including thermal generation or band-band-band tunneling.

Figure 7 shows the improved version, which includes the triggering, the self-sustaining process, and the self-quenching of the avalanche by incorporating of current-voltage controlled switches [39]. In order to represent the nonlinear I-V characteristics above breakdown, the model includes nonlinear voltage generator, V_{SPAD}, to generate piecewise linear curve with different slopes.

An accurate model for SPADs [40] exploits the behavioral description of the sensor with biasing circuits and aims to provide optimal biasing circuit design through SPAD simulation. In order to represent the SPAD above breakdown and with the avalanche triggering and self-quenching mechanisms, a complete SPICE circuit model for SPAD has been presented in [41]. The SPAD is implemented using a piecewise non-linear approximation and modeled through a non-linear series resistance above breakdown. The model also includes the forward region and the secondary breakdown due to edge-junction or punch- through effects (**Figure 8**).

SPAD stochastic phenomena affect the switching behavior of the device and define the transition from no-avalanche to avalanche (turn-on) and vice versa. In order to provide a more realistic simulation platform, more comprehensive models [34, 42–45] include stochastic nature of Geiger mode operation based on theoretical equations of dark count rate, breakdown probability, signal-to-noise ratio and after-pulsing probability.

The behavioral model presented in [42], simulates the noise model due to dark count rate and after pulsing based on fabricated component for the first time. The model improves the previous circuit model [41] by adding the noise sources of avalanche photodiode. The model has been developed using specter active and passive components to represent the unwanted after-pulse and dark count events. At first, the parasitic capacitors of the sensors (anode-cathode capacitor, anode-bulk and the cathode-bulk capacitors) are included to represent the dynamic
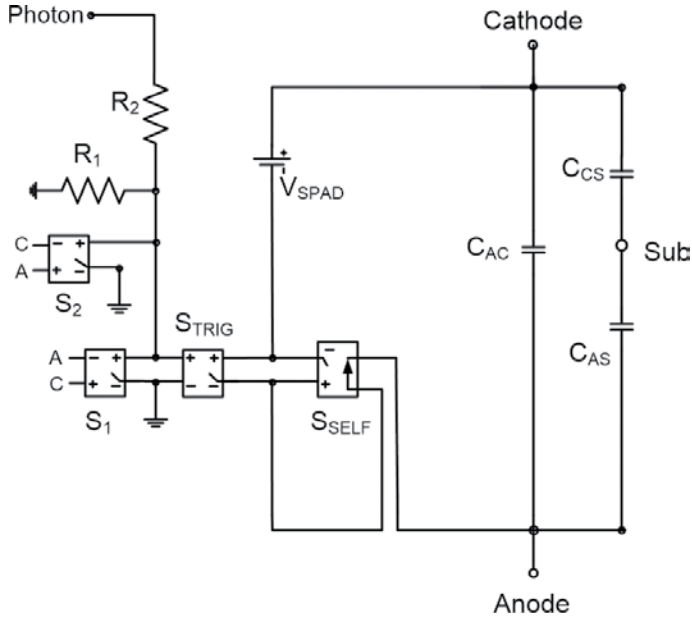
Figure 7.
Improved SPAD model [39]; switch S_{TRIG} is used to trigger the detector through "photon" input, S_{SELF} is used to include self-sustaining and self-quenching of the avalanche, and V_{SPAD} represents the nonlinear I-V curve.
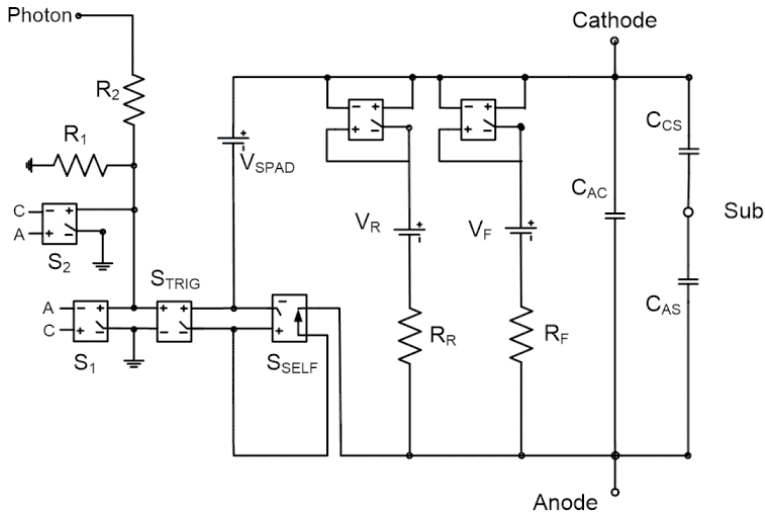
Figure 8.
Complete SPAD model [41] with switches S_{TRIG} and S_{SELF} representing avalanche triggering and self-sustaining; two additional branches are included to represent forward and reverse biasing.

behavior. Three different branches representing forward, reverse and effects of noise behavior are incorporated to simulate the I-V behavior. Each branch is controlled by an ideal voltage controlled switch. Finally, two noise sources, represented with two corresponding branches are added to simulate the noise effect (**Figure 9**).

An accurate behavioral model reported in [43] models the major statistical behaviors of SPADs including the turn-off probability, dark count rate and afterpulse phenomena. One the major focus of the model was to explore the dependence of the device capacitance on the reverse bias.

Figure 9.
SPAD behavioral model including I-V behavior and noise sources for dark counts and after-pulsing [42].

SPAD is unresponsive to any subsequent photons after detecting the first photon (during avalanche, quenching and resetting cycle) until it is reset back to undergo another avalanche. This time duration is known as dead time. In order to accurately interpret the SPAD measurements, dead time needs to be taken into account especially for large arrays of CMOS SPAD based detectors. In [44], a dead time model was reported for externally reset SPADs. Here, time distribution of incidents counts is assumed to follow Poisson distribution.

4.2.3 Model based on information theory

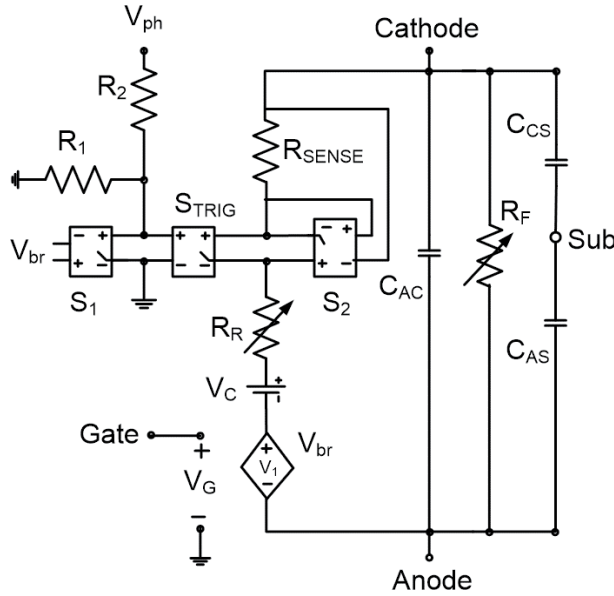In order to simulate the behavior of SPAD's array and predict the behavior at system level design, model based on information theory include a combination of the previously mentioned models [47, 48]. These system levels models are helpful to simulate the operation of multiple SPADs including both high-density and low-density arrays. Various operational aspects of SPAD arrays such as array breakdown voltage non-uniformity, pixel cross-talk can be investigated using these models. Some models are able to study the performance at single-pixel-level [48]. They consider the SPAD front-end as an information channel. Then the information capacity and mutual information can be calculated from the information channel as a function of excess bias voltage, dark count rate, and after pulsing probability. The information theoretic model reported in [47] includes a channel-capacity metric to evaluate the performance of SPADs as a detector in laser communication systems for optimizing its performance with respect to the device structure and operating voltage.

4.3 State-of-the-art PGSPAD models

A perimeter gated SPAD (PGSPAD) is a SPAD with an additional polysilicon gate terminal and its effects need to be properly modeled. PGSPAD models were reported in the literatures to predict the Geiger mode response to a photon; simulate the static and dynamic I-V characteristics considering the effect of applied voltage at additional gate terminal [31, 33, 34, 48]. The equivalent circuit models for PGSPAD [31, 33] simulate the static and dynamic behavior of PGSPADs with the additional gate terminal. These models are based on the improved SPAD equivalent model [41]. The PGSPAD model simulates the avalanche in similar way to SPAD model [41]. In addition, they include a dependent voltage source to represent the dependence of breakdown voltage (V_{br}) on gate voltage (V_G) and the reverse biased resistance as a variable resistance depending on gate bias voltage

Figure 10.
Equivalent circuit model of perimeter gated single photon avalanche diode (PGSPAD) where terminals A, C, S, and G represents the anode, cathode, substrate and gate terminals [31].

and reverse bias voltage (**Figure 10**). Two parallel branches are incorporated to simulate the forward and reverse bias operation. Model parameters and threshold voltage of the switches are extracted from the fabricated PGSPAD device. From the empirical data, it was found that the breakdown voltage depends on zero-bias breakdown voltage and the gate voltage. The empirical relation [31] of V_{br}, reverse branch resistance (R_R), forward branch resistance (R_F) with gate voltage (V_G) and anode-cathode biasing (V_{CA}) are,

$$V_{br} = \gamma V_G + V_{br0} \tag{10}$$

$$R_R = P \exp\left(Q(V_{CA} - V_{br0} + V_1)\right) \tag{11}$$

$$R_F = R \exp\left(SV_{AC}\right) \tag{12}$$

where γ is a fitting constant obtained from experimental perimeter gate voltage versus breakdown voltage, P, Q, R, and S are constants determined experimentally, V_{br0} is the zero bias breakdown voltage.

An improved PGSPAD SPICE model was reported in [34] to simulate the stochastic behavior of PGSPAD. The model correctly simulates the dark count rate with variation of gate voltage and excess bias voltage, the applied reverse biased voltage in excess of breakdown voltage. The model includes the dark current noise due to non-photon driven carrier generation mechanisms and the spectral response with the additional gate terminal. It uses Shockley-Hall-Read equation and tunneling current equation to calculate the thermal carrier generation rate and carrier generation rate due to band-to-band tunneling respectively. Finally, the model established that the band-to-band tunneling mechanism depends on the gate bias voltage through the electric field. The PGSPAD model presented in [48] evaluates the performance of PGSPAD using the information theory principles. The model estimates the optimization of the information rate of the PGSPAD by applying the asymmetric communication channel model to the device.

5. IMT

Insulator Metal Transition (IMT) devices are volatile memristors that have recently spurred significant interest in the research community [49]. In crossbar memory arrays, IMT devices are often leveraged as selector devices owing to their Back-End-Of-Line (BEOL) compatibility and high ON/OFF ratio [50, 51]. On the neuromorhpic front, the inherent switching dynamics of IMT devices have been shown to mimic the Integrate-And-Fire neurons which alleviates the need for complex CMOS circuitry, thus, enabling higher integration density [52, 53]. In addition, volatile memristors with short-term memory [54–56] can also be used as synapses for neuromorphic application.

5.1 Device operation

Several studies have shown that temperature is the main driver of phase transition [57, 58] while other works argue that the electric field is the main driver of resistive switching while the Joule heating plays a secondary role [59]. A more thorough study about IMT's switching mechanism is reported in [60, 61] which show that Joule heating is not sufficient to instigate switching and that an Electric field assisted phase transition is more likely. The work in [60] proposes that a certain threshold voltage is required to effect a phase transition which decreases as temperature increases.

5.2 Motivation behind compact model

In [52], an IMT device model that captures the positive feedback between the temperature and electric field was presented. Here, the relationship between the device resistance and the device temperature was implemented using a look up table. In [62], another device model was proposed based on band theory. The IMT device is modeled as a low bandgap semiconductor. Increasing the device temperature results in decreasing the bandgap, thus, increasing carrier concentration. This increase in carrier concentration ultimately results in decreasing the device's resistance. A model is also presented which captures the change in the thermal conductivity with temperature. The thermal conductivity model along with the band gap model are then solved in a self-consistent fashion to effect a temperature dependent phase transition. The model in [62] was implemented in Sentaurus TCAD simulator wherein the built-in electrothermal models and finite element drift-diffusion model where leveraged. This model, similar to the previous one, is best used in a TCAD simulation flow and not SPICE level simulators. The lack of a physics-based compact model, however, has hindered circuit designers from exploring the full potential of IMTs in circuit applications which is the motivation behind the development of the following simplified compact model.

5.3 Simplified compact model

This work focuses on an IMT compact model originally proposed in [63]. The model describes the IMT device as a memristor with the device's local temperature being the state variable. The proposed model is simulated using Specter from Cadence and exhibits a close match to experimental data and electro-thermal simulations based on the models in [52, 62].

As the current flows through the device, the device's temperature increases until it reaches a critical temperature at which point it transitions from a high resistance

state to a low resistance state. As the temperature decreases, the resistance relaxes back to its default high resistance state. The memristive dynamics of the IMT can be expressed as follows [64].

$$V = R(x)I \tag{13}$$

$$\frac{dx}{dt} = g(x, V) \tag{14}$$

where (13) and (14) represent the port and state equations, respectively, and x is the state variable. The proposed model consists of two governing equations: (a) the resistance change equation that corresponds to the port equation and (b) the temperature evolution equation which corresponds to the state equation, with the temperature being the state variable such that $x = T(t)$.

The behavior of the resistance change versus temperature is described by two thermistor states for the high resistance state and the low resistance state and a sigmoid function capturing the transition from a high resistance state to a low resistance state. Since the thermistance behavior depicts a linear relationship between the resistance and the temperature in the Log-Linear domain, one can readily model the two thermistors as exponential functions of the temperature such that $R_{LRS} = R_{LRS_F} e^{-B_{LRS}(T(t)-T_F)}$ and $R_{HRS} = R_{HRS_0} e^{-B_{HRS}(T(t)-T_0)}$. R_{LRS_F} is the low resistance state defined at temperature T_F (a reference temperaure) and R_{HRS_0} is the high resistance state defined at the ambient temperature T_0. B_{LRS} and B_{HRS} are the negative temperature coefficients of the thermistors which can be readily extracted from the slope of the thermistance versus temperature plot. This modeling framework, however, requires clipping of the R_{LRS} and R_{HRS} at some minimum and maximum values to avoid any unphysical behavior in circuit simulation. Clipping, however, often uses conditional statements, which hampers the "smoothness" of the model yielding potential convergence difficulties in circuit simulation. Hence, the model equations are reformulated such that R_{LRS} and R_{HRS} smoothly approach to R_{LRS_F} and R_{HRS_0} at high and low temperatures, respectively.

This relationship between the resistance and the temperature can be described as follows:

$$R_{LRS} = R_{LRS_F} \left(1 + K_{LRS}^A\right)^{1/A} \tag{15}$$

$$R_{HRS} = R_{HRS_0} \frac{K_{HRS}}{\left(1 + K_{HRS}^A\right)^{1/A}} \tag{16}$$

$$R_{IMT} = R_{LRS} + \frac{(R_{HRS} - R_{LRS})}{1 + e^{\frac{T(t)-T_c}{T_x}}} \tag{17}$$

where $K_{LRS} = e^{-B_{LRS}(T(t)-T_F)}$ and $K_{HRS} = e^{-B_{HRS}(T(t)-T_0)}$

The fitting parameter, T_x, captures the sharpness of the resistance transition. T_c is the critical temperature which is around 340 K in the case of VO$_2$ devices [53]. R_{LRS} and R_{HRS} are the low resistance state and high resistance state, respectively. A is a control parameter that governs how the two thermistors approach the asymptotes [65]. While the model might seem complicated at first glance, the principal equations are simple exponential functions. This formulation is employed to abide by compact modeling practices as suggested in [65, 66].

The temperature evolution dynamics are described by the compact thermal model in [67] as shown in (4):

$$C_{th} \frac{dT(t)}{dt} = V_{IMT} I_{IMT} - \frac{T(t) - T_0}{R_{th}} \tag{18}$$

where $V_{IMT} I_{IMT}$ is the Joule heating, C_{th} and R_{th} are the effective thermal capacitance and the effective thermal resistance, respectively, and T_0 is the ambient temperature. This model assumes that the device stays at an effective temperature $T(t)$ and exchanges heat with the ambient environment at an ambient temperature T_0.

The model predictions closely follow the experimental data as well as electro-thermal simulation [52] as shown in **Figures 11–15**. **Figures 11** and **12** capture the resistance transition around the critical temperature which is about 340 K in VO_2 devices fitted against experimental data from [52]. **Figure 13** depicts the hysteresis in the I-V domain (a characteristic of memristors) exhibited by the IMT device as shown in [52, 53] and fitted against the experimental data from [52]. **Figures 14** and **15** capture the time dependence of temperature and resistance evolution, respectively, fitted against electrothermal simulations from [52]. Three voltage levels, based on the values used in [52] were applied across the IMT device: 1.4 V (blue), 1.6 V (red) and 1.8 V (green). One can readily observe in **Figure 14** that the local temperature of the device saturates at a higher temperature value for higher
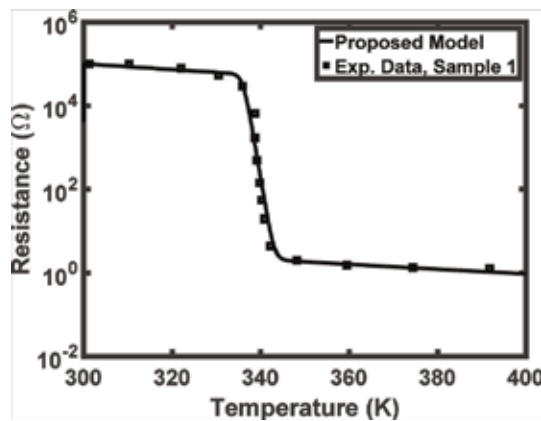

Figure 11.
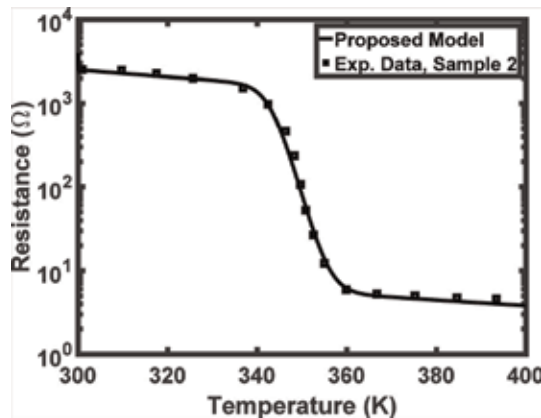*Model (solid line) fitting against experimental data (marker), sample 1.*

Figure 12.
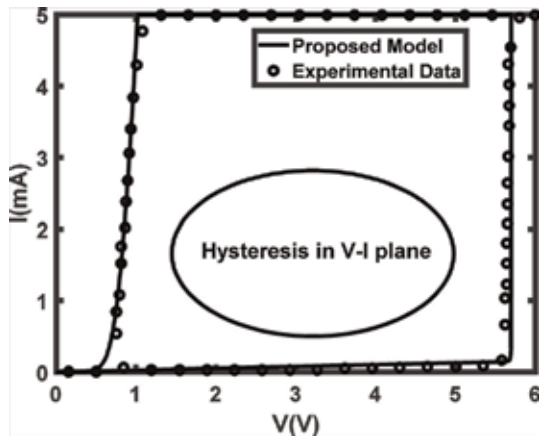*Model (solid line) fitting against experimental data (marker), sample 2.*

Figure 13.
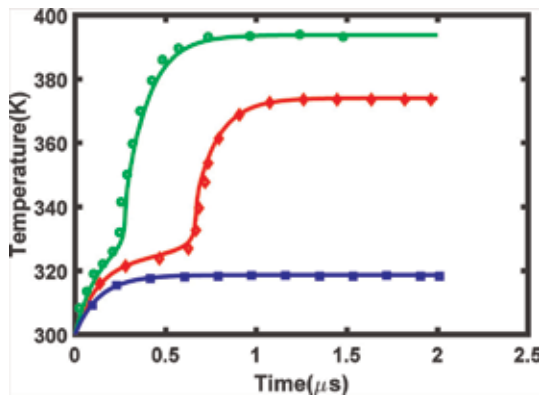*Model fitting showing pinched hysteresis.*

Figure 14.
Model (solid line) fitting against electro-thermal simulations (markers); plotting the device local temperature against time for three applied voltage values.
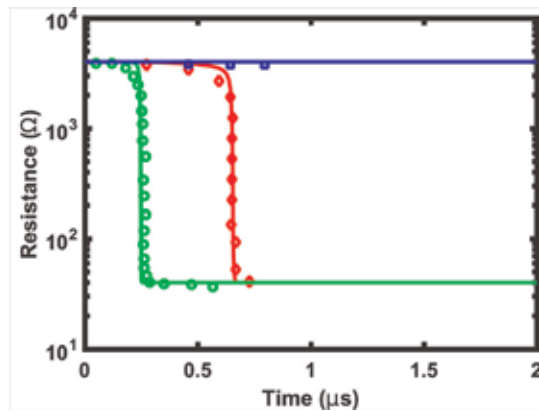

Figure 15.
Model (solid line) fitting against elector-thermal simulations (markers); plotting the device resistance against time for three applied voltage values.
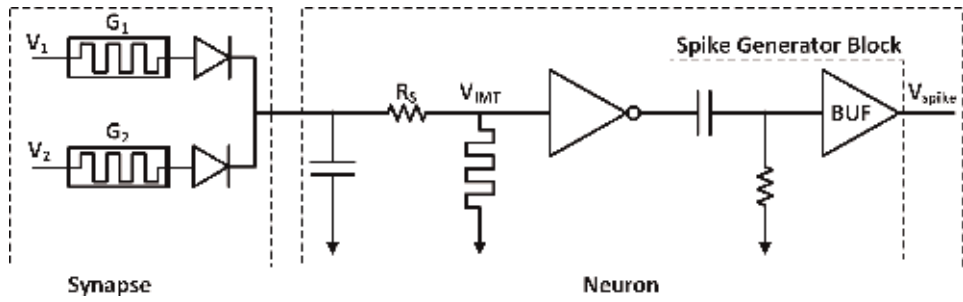
Figure 16.
Schematic of the proposed neuron circuit.

voltages due to increased Joule heating. In **Figure 15**, higher voltages result in a faster transition due to higher rate of joule heating.

5.4 Application in neuron design

Figure 16 depicts a simple neuron based on the proposed circuit in [52]. First, the input voltage spikes are fed through the synaptic network. The dot product multiplication is then executed between the input spikes and the synaptic weights via Ohm's law such that the accumulated sum follows $I_{sum} = \sum_i V_i G_i$. I_{sum} is then fed to the neuron which is represented by the parallel combination of the IMT device and the capacitor. The core of the neuron is the IMT device which switches from R_{HRS} to R_{LRS} when the device's temperature exceeds the critical temperature resulting in a current spike. The current spike is converted to a voltage pulse via a CMOS inverter. A spike generator is then added to generate an output voltage spike with a pulse width controlled by the RC time constant of the RC network preceding the output buffer. **Figure 17** depicts the simulation results of the neuron circuit.
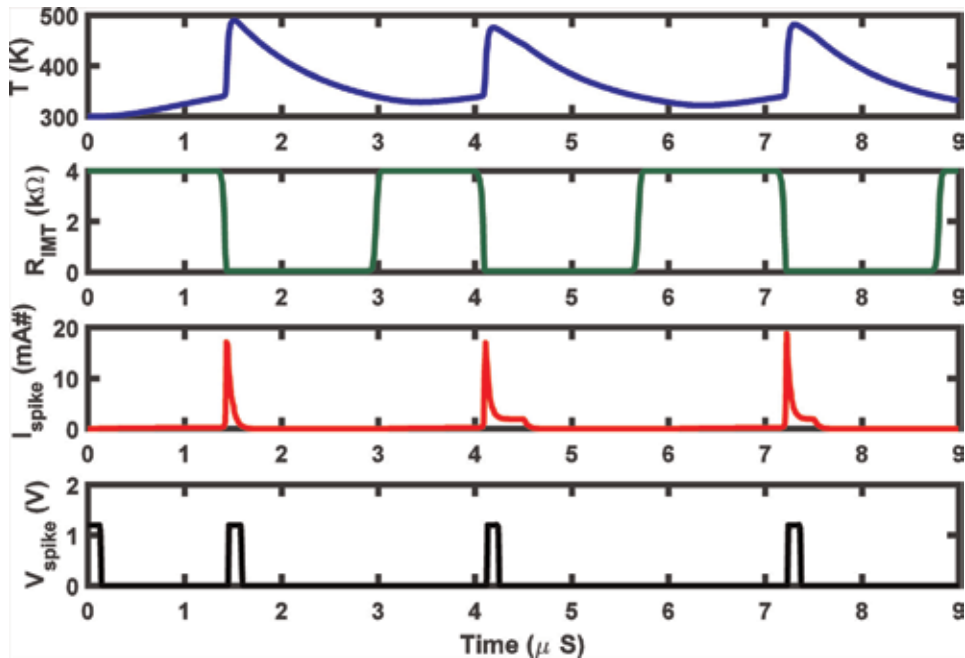

Figure 17.
Simulation of the proposed neuron.

The essence of neuron oscillation rests in the IMT device alternating between R_{HRS} and R_{LRS}. At R_{HRS}, the steady state temperature exceeds the critical temperature and, accordingly, the neuron fires. At R_{LRS}, the steady state temperature drops below the critical temperature, the neuron resets and the process is repeated for the next inputs.

At steady state ($\frac{dT}{dt} = 0$), the solution to the differential equation in (18) can be described as follows:

$$T_{ss} = T_0 + R_{th} I_{IMT}^2 R_{IMT}$$

where T_{ss} is the steady state temperature of the IMT device. Hence, according to the aforementioned explanation, the oscillation condition can be expressed as follows:

$$R_{th} I_{IMT}^2 R_{LRS} < T_c - T_0 < R_{th} I_{IMT}^2 R_{HRS}$$

Inequality (7) establishes the oscillation condition for the IMT-based neuron as a function of device parameters such as R_{th}, R_{LRS}, R_{HRS} and T_c and circuit variables such as I_{IMT} which is a function of the amplitude of the voltage spike and the series resistance with the IMT device including the synapse resistance, diode ON resistance and the IMT series resistance. The neuron typically operates in three phases: (I) accumulation wherein the inputs from the synapse networks are summed, (II) firing when the accumulated value reaches the neuron's threshold and (III) refractory period wherein the neuron is idle.

In CMOS neurons, two operational amplifiers are required for accumulation (integration) and firing (comparison). In addition, a feedback circuit is often employed to implement the refractory period. These operational amplifiers, besides entailing all the complexities of analog design, are also area consuming and power hungry. On the other hand, the IMT device can provide the accumulation function through the heating of the device, fire through device transition and a refractory period during device cooling should the device be placed in such configuration. A typical CMOS neuron, such as the work in [68], requires more than 20 transistors while the proposed IMT-based neuron only requires 7 transistors.

6. Conclusion

Computer aided design and simulation plays a major role in the advancement of semiconductor industry. A multitude of exciting new devices has emerged in recent years. There is a growing need in the industry and academia for fast and reliable compact models of these emerging devices to enable useful circuit design leveraging their unique capabilities. In this chapter, we show how different approaches can be adopted to model three emerging semiconductor devices namely, silicon- on- insulator four gate transistor (G[4]FET), single photon avalanche diode (SPAD) and insulator-metal transistor (IMT) device with volatile memristance. All the models have been verified against experimental/TCAD data and implemented in commercial circuit simulator. The ideas developed in this chapter can also be transferred to model other emerging devices.

Author details

Md Sakib Hasan[1*], Mst Shamim Ara Shawkat[1], Sherif Amer[1], Syed Kamrul Islam[2], Nicole McFarlane[1] and Garrett S. Rose[1]

1 Department of Electrical Engineering and Computer Science, University of Tennessee, Knoxville, TN, USA

2 Department of Electrical Engineering and Computer Science, University of Missouri, Columbia, MO, USA

*Address all correspondence to: mhasan4@vols.utk.edu

IntechOpen

References

[1] Blalock BJ, Cristoloveanu S, Dufrene BM, Allibert F, Mojarradi MM. International journal of high speed electronics and systems. The Multiple-Gate MOS-JFET Transistor. 2002;**12**(2): 511-520

[2] Akarvardar K, Chen S, Vandersand J, Blalock BJ, Schrimpf RD, Prothro B, et al. Four-gate transistor voltage-controlled negative differential resistance device and related circuit applications. In: Proc. IEEE International SOI Conference. 2006. pp. 71-72

[3] Akarvardar K, Chen S, Blalock B, Cristoloveanu S, Gentil P, Mojarradi M. A novel four-quadrant analog multiplier using SOI four-gate transistors (G4-FETs). In: Proceedings of ESSCIRC. 2005

[4] Akarvardar K, Blalock B, Chen S, Cristoloveanu S, Gentil P, Mojarradi MM. Digital circuits using SOI four-gate transistor. In: 8th International Conference on Solid-State and Integrated Circuit Technology Proceedings. 2006

[5] Fijany A, Vatan F, Mojarradi M, Toomarian B, Blalock B, Akarvardar K, et al. The G4-FET: A universal and programmable logic gate. In: Proceedings of the 15th ACM Great Lakes symposium on VLSI. 2005

[6] Friedman JS, Godkin A, Henning A, Vaknin Y, Rosenwaks Y, Sahakian AV. Threshold logic with electrostatically formed nanowires. IEEE Transactions on Electron Devices. 2016;**63**(3):1388-1391

[7] Henning A, Swaminathan N, Godkin N, Shalev G, Amit I, Rosewaks Y. Tunable diameter electrostatically formed nanowire for high sensitivity gas sensing. Nano Research. 2015;**8**(7):2206-2215

[8] Majumder MB, Hasan MS, Uddin M, Rose GS. Chaos computing for mitigating side channel attack. In: IEEE International Symposium on Hardware Oriented Security and Trust (HOST). 2018

[9] Shanta AS, Majumder MB, Hasan MS, Uddin M, Rose GS. Design of a Reconfigurable Chaos Gate with enhanced functionality space in 65nm CMOS. In: 2018 IEEE 61st International Midwest Symposium on Circuits and Systems (MWSCAS), Windsor. 2018

[10] Akarvardar KDBCS, Blalock BJ, Higashino T, Mojarradi MM, Kolawa E. Multi-bias dependence of threshold voltage, subthreshold swing, and mobility in G4-FETs. In: Proc. ESSDERC. 2003

[11] Akarvardar K, Cristoloveanu S, Gentil P. Analytical modeling of the two-dimensional potential distribution and threshold voltage of the SOI four-gate transistor. IEEE Transactions on Electron Devices. 2006;**53**(10):2569-2577

[12] Akarvardar K, Cristoloveanu S, Gentil P, Blalock BJ, Dufrene B, Mojarradi MM. Depletion-all-around in SOI G4-FETs: A conduction mechanism with high performance. In: Proceedings of the 30th European Solid-State Circuits Conference. 2004

[13] Akarvardar K, Cristoloveanu S, Gentil P, Schrimpf RD, Blalock BJ. Depletion-all-around operation of the SOI four-gate transistor. IEEE Transactions on Electron Devices. 2007; **54**(2):323-331

[14] Tejada JAJ, Rodríguez AL, Godoy A, Villanueva JAL, Gómez-Campos FM, Rodríguez-Bolívar S. A low-frequency noise model for four-gate Field-effect transistors. IEEE Transactions on Electron Devices. 2008;**55**(3):896-903

[15] Tejada JAJ, Rodríguez AL, Godoy A, Rodríguez-Bolívar S, Villanueva JAL, Marinov O, et al. Effects of gate oxide and junction nonuniformity on the DC and low-frequency noise performance of four-gate transistors. IEEE Transactions on Electron Devices. 2012;**59**(2):459-467

[16] Sayed S, Khan MZ. Analytical modeling of surface accumulation behavior of fully depleted SOI four gate transistors (G 4-FETs). Solid-State Electronics. 2013;**81**:105-112

[17] Sayed S, Hossain MI, Khan MZR. A subthreshold swing model for thin-film fully depleted SOI four-gate transistors. IEEE Transactions on Electron Devices. 2012;**59**(3):854-857

[18] Chiang TK. A new two-dimensional analytical model for the fully-depleted SOI four-gate transistor. In: 10th IEEE International Conference on Solid-State and Integrated Circuit Technology, Shanghai. 2010

[19] Sayed S, Hossain MI, Huq R, Khan MZR. Three dimensional modeling of SOI four gate transistors. In: IEEE Nanotechnology Materials and Devices Conference, Monterey. 2010

[20] Hasan MS, Rahman T, Islam SK, Blalock B. Numerical modeling and implementation in circuit simulator of SOI four-gate transistor (G4FET) using multidimensional Lagrange and Bernstein polynomial. Microelectronics Journal. 2017;**65**:84-93

[21] Hasan MS, Islam S. DC modeling of SOI four-gate transistor (G4FET) for implementation in circuit simulator using multivariate regression polynomial. IET Circuits, Devices & Systems;**2018**

[22] Hasan MS, Islam SK, Blalock BJ. Modeling of SOI four-gate transistor (G 4 FET) using multidimensional spline interpolation method. Microelectronics Journal. 2018;**76**:33-42

[23] Hasan MS, Mahbub I, Islam SK, Rose GS. A MOS-JFET macromodel of SOI four-gate transistors (G4FET) to aid innovative circuit design. In: IEEE 13th Dallas Circuits and Systems Conference (DCAS), Dallas. 2018

[24] Moler CB. Numerical Computing with MATLAB. 2004

[25] Shichman H, Hodges DA. Modeling and simulation of insulated-gate field-effect transistor switching circuits. IEEE Journal of Solid-State Circuits. 1968;**3**(3): 285-289

[26] Cova S, Ghioni M, Lotito A, Rech I, Zappa F. Evolution and prospects for single-photon avalanche diodes and quenching circuits. Journal of Modern Optics. 2004;**51**:1267-1288

[27] Niclass C, Rochas A, Besse P, Charbon E. Design and characterization of a CMOS 3-D image sensor based on single-photon avalanche diodes. IEEE Journal of Solid-State Circuits. 2005;**40**: 1847-1854

[28] Gersbach M, Maruyama Y, Niclass C, Sawada K, Charbon E. A room temperature CMOS single photon sensor for chemiluminescence detection. In: Miniaturized Systems for Chemistry and Life Sciences. 2006

[29] Dandin M, Akturk A, Nouri B, Goldsman N, Abshire P. Characterization of single-photon avalanche diodes in a 0.5μm standard CMOS process—Part 1: Peimeter breakdown suppression. IEEE Sensors Journal. 2010;**10**(11):1682-1690

[30] Stoppa D, Mosconi D, Pancheri L, Gonzo L. Single-photon avalanche diode CMOS sensor for timeresolved fluorescence measurements. IEEE Sensors Journal. 2009;**9**(9):1084-1090

[31] Dandin M, Habib MHU, Nouri B, Abshire P, McFarlane N. Characterization of single-photon

avalanche diodes in a 0.5 μm standard CMOS process—Part 2: Equivalent circuit model and Geiger mode readout. IEEE Sensors Journal. 2016;**16**(9):3075-3083

[32] Palubiak DP, Deen M. CMOS SPADs: Design issues and research challenges for detectors, circuits, and arrays. IEEE Journal of Selected Topics in Quantum Electronics. 2014;**20**(6): 409-426

[33] Habib MHU, Mamun KAA, McFarlane N. A SPICE model for perimeter-gated single photon avalanche diode. In: International Midwest Symposium on Circuits and Systems. 2014

[34] Shawkat MSA, Habib MHU, McFarlane N. An analog CMOS silicon photomultiplier using perimeter-gated single-photon avalanche diodes. IEEE Transactions on Circuits and Systems I. 2018;**65**(11):3830-3841

[35] Hurkx GAM, Graaff HCD, Kloosterman WJ, Knuvers MPG. A new analytical diode model including tunneling and avalanche breakdown. IEEE Transactions on Electron Devices. 1992;**39**(9):2090-2098

[36] Javitt M, Savuskan V, Merhav T, Nemirovsky Y. Revisiting single photon avalanche diode currentvoltage modeling and transient characteristics. Journal of Applied Physics. 2014;**115** (20)

[37] Lacaita A, Cova S, Spinelli A, Zappa F. Photon-assisted avalanche spreading in reach-through photodiodes. Applied Physics Letters. 1993;**62**(6):606-608

[38] Tisa S, Zappa F, Tosi A, Cova S. Electronics for single photon avalanche diode arrays. Sensors and Actuators A. 2007;**140**:113-122

[39] Mora AD, Tosi A, Tisa S, Zappa F. Single-photon avalanche diode model

for circuit simulations. IEEE Photonics Technology Letters. 2007;**19**(23):1922-1924

[40] Mita R, Palumbo G, Fallica P. Accurate model for single photon avalanche diodes. IET Circuits, Devices and Systems. 2008;**2**(2):207-212

[41] Zappa F, Tosi A, Mora AD, Tisa S. SPICE modeling of single photon avalanche diodes. Sensors Actuator A, Physics. 2008;**153**(2):207-212

[42] Arbat A, Dièguez A, Gascon D, Trenado J, Garrido L. Avalanche photodiodes for high energy particle tracking in 130 nm CMOS technology. In: 16th IEEE International Conference on Electronics, Circuits and Systems—(ICECS 2009). 2009

[43] Giustolisi G, Mita R, Palumbo G. Behavioral modeling of statistical phenomena of single-photon avalanche diodes. International Journal of Circuit Theory and Applications. 2012;**40**(7): 661-679

[44] Chick S, Coath R, Sellahewa R, Turchetta R, Leitner T, Fenigstein A. Dead time compensation in CMOS single photon avalanche diodes with active quenching and external reset. IEEE Transactions on Electron Devices. 2014;**61**(8):2725-2731

[45] Kolb KE. Signal-to-noise ratio of Geiger-mode avalanche photodiode single-photon counting detectors. Optical Engineering. 2014;**53**(8): 081804-1 -081804-9

[46] Field RM, Lary J, Cohn J, Paninski L, Shepard KL. A low noise, single-photon avalanche diode in standard 0.13 μm complementary metal-oxide-semiconductor process. Applied Physics Letters. 2010;**97**(21)

[47] Ramirez DA, Hayat MM, Torres SN, Saleh BEA, Teich MC. Information-theoretic criterion for the performance

of single-photon avalanche photodiodes. IEEE Photonics Technology Letters. 2005;**17**(10):2164-2166

[48] Gu J, Habib MHU, McFarlane N. Perimeter gated single photn avalanche diodes: An information theoretic assessment. IEEE Photonics Technology Letters. 2016;**28**(6):701-704

[49] Zhou Y, Ramanathan S. Mott memory and Neuromorphic devices. Proceedings of the IEEE. 2015;**103**(8): 1289-1310

[50] Son M, Lee J, Park J, Shin J, Choi G, Jung S, et al. Excellent selector characteristics of Nanoscale VO2 for high-density bipolar ReRAM applications. IEEE Electron Device Letters. 2011;**32**(11):1579-1581

[51] Gao L, Holbert KE, Yu S. Total ionizing dose effects of gamma ray radiation on NbO x-based selector devices for crossbar array memory. IEEE Transactions on Nuclear Science. 2017;**64**(6):1535-1539

[52] Lin J, Annadi A, Sonde S, Chen C, Stan L, Achari K, et al. Low-voltage artificial neuron using feedback engineered insulatorto-metal-transition devices. In: IEEE International Electron Devices Meeting (IEDM). 2016

[53] Chen P, Seo J, Cao Y, Yu S. Compact oscillation neuron exploiting metal-insulator-transition for neuromorphic computing. In: Proceedings of the ACM International Conference on Computer-Aided Design. 2016

[54] Najem JS, Taylor GJ, Weiss RJ, Hasan MS, Rose G, Schuman CD, et al. Memristive Ion Channel-Doped Biomembranes as Synaptic Mimics. ACS Nano. 2018

[55] Weiss R, Najem JS, Hasan MS, Schuman CD, Belianinov A, Collier P, et al. A soft-matter biomolecular memristor synapse for neuromorphic

systems. In: IEEE Biomedical Circuits and Systems Conference (BioCAS). 2018

[56] Hasan MS, Schuman CD, Najem JS, Weiss R, Skuda N, Belianinov A, et al. Biomimetic soft-material synapse for neuromorphic computing: From device to network. In: IEEE Dallas Circuits and Systems Conference, Dallas. 2018

[57] Ruzmetov D, Senanayake SD, Narayanamurti V, Ramanathan S. Correlation between metal-insulator transition characteristics and electronic structure changes in vanadium oxide thin films. Physical Review B. 2008;**77** (19)

[58] Freeman E, Kar A, Shukla N, Misra R, Engel-Herbert R, Schlom D, et al. Characterization and modeling of metal-insulator transition (mit) based tunnel junctions. In: IEEE 70th Annual Device Research Conference (DRC). 2012

[59] Ruzmetov D, Gopalakrishnan G, Deng J, Narayanamurti V, Ramanathan S. Electrical triggering of metal-insulator transition in nanoscale vanadium oxide junctions. Journal of Applied Physics. 2009;**106**(8)

[60] Yang Z, Hart S, Ko C, Yacoby A, Ramanathan S. Studies on electric triggering of the metal-insulator transition in vo2 thin films between 77 K and 300 K. Journal of Applied Physics. 2011;**110**(3)

[61] Gopalakrishnan G, Ruzmetov D, Ramanathan S. On the triggering mechanism for the metal–insulator transition in thin film vo2 devices: Electric field versus thermal effects. Journal of Materials Science. 2009; **44**(19):5345-5353

[62] Karda K, Mouli C, Ramanathan S, Alam MA. A self-consistent, semiclassical electrothermal modeling framework for Mott devices. IEEE

Transactions on Electron Devices. 2018;
65(5):1672-1678

[63] Amer S, Hasan MS, Adnan MM,
Rose GS. Spice modeling of insulator
metal transition: Model of the critical
temperature. IEEE Journal of the
Electron Devices Society. 2018

[64] Chua L. Everything you wish to
know about memristors but are afraid to
ask. Radioengineering. 2015;**24**(2)

[65] Tsividis Y, McAndrew C. Operation
and Modeling of the MOS Transistor.
Oxford Univ. Press; 2011

[66] McAndrew CC, Coram GJ,
Gullapalli KK, Jones JR, Nagel LW, Roy
AS, et al. Best practices for compact
modeling in verilog-a. IEEE Journal of
the Electron Devices Society. 2015;**3**(5):
383-396

[67] Chen P-Y, Yu S. Compact modeling
of RRAM devices and its applications in
1T1R and 1S1R Array design. IEEE
Transactions on Electron Devices. 2015;
62(12):4022-4028

[68] Chakma G, Adnan MM, Wyer AR,
Weiss R, Schuman CD, Rose GS.
Memristive mixed-signal neuromorphic
systems: Energy-efficient learning at the
circuit-level. IEEE Journal on Emerging
and Selected Topics in Circuits and
Systems. 2018;**8**(1)

Mathematical Modeling of Aerodynamic Heating and Pressure Distribution on a 5-Inch Hemispherical Concave Nose in Supersonic Flow

Dimitrios P. Spiridakos, Nicholas C. Markatos and Despoina Karadimou

Abstract

During the design of an aircraft, a significant parameter that is taken into consideration is aerodynamic heating. Aerodynamically induced heating affects both the structure of the aircraft and its vulnerability to heat-seeking missiles in modern warfare. As a result, the ability to calculate efficiently the heating produced as well as the pressure distribution in such flows is crucial. Therefore, in this present study, the PHOENICS CFD code as modified by DRA Farnborough in order to calculate heat transfer and pressure measurement on a 5-inch hemispherical concave nose at a Mach number of 2.0 is evaluated and customized in order to produce faster and more accurate results. Apart from numerical alterations, different turbulence models are being examined as well as different discretization schemes. Numerical solutions show improvement up to 6% in comparison with the original model, both in terms of convergence rate and in terms of agreement with the available experimental data. With the new modeling suggested in the present work, the significance of both the discretization scheme and the choice of the turbulence modeling is demonstrated for the flows under consideration. The use of a high-order discretization scheme is suggested for more acute areas of the body modeled in order to improve results further.

Keywords: aerodynamic heating, turbulence modeling, hypersonic flow, discretization scheme, PHOENICS

1. Introduction

Aerodynamic heating has been a major study issue for a long time now and many investigations have been conducted by researchers in order to achieve high-quality simulation results, both on the theoretical and the numerical level. Experimental studies of the above phenomenon are rare, as conducting such research is prohibitively expensive.

Aerodynamic heating is a phenomenon worth studying as its significance lies in two major scientific fields. At first, aerodynamic heating is the most significant parameter of the emitted infrared radiation from aircraft, a fact that is of direct interest in military studies. According to statistics, the majority of aerial vehicles downed in modern warfare was due to weapons based on detecting Infrared signature level of those vehicles. Their percentage is as high as 89% of total aircraft shot downs between 1967 and 1993, according to Thompson J. et al. [1]. Apart from the emitted infrared radiation, the phenomenon of aerodynamic heating has to be taken into consideration when designing aerospace vehicles that fly at speeds comparable to that of sound. Ultrasonic aircraft and aircraft that re-enter the atmosphere can develop temperatures high enough that have to be carefully considered when designing the aircraft, in order to avoid unpleasant situations.

Aerodynamic heating is a phenomenon that takes place mostly due to heat from the warm part of the boundary layer to the body's surface. However, when approaching the speed of sound, aerodynamic heating phenomena are enhanced by the radiation emitted from molecules that are being decomposed and ionized due to the temperature rising behind the shockwave. At speeds greater than 5000 m/sec, the emitted radiation becomes significant and plays a measurable role in the phenomenon. Finally, another way that aerodynamic heating takes place concerns aircraft that fly in the higher atmospheric layers, where the distance between the air molecules is comparable to the aerial vehicle dimensions. However, the present study is focused only on the convection phenomena that lead to aerodynamic heating, as the speeds examined do not exceed Mach numbers of 2.

As mentioned above, the significance of aerodynamic heating is a major issue in both the preliminary design of aerial vehicles and the calculation of the infrared radiation emitted from the vehicle in flight. Apart from experimental methods, which may offer reliable results but require enormous budgets, numerous simulations have been carried out via means of computational mechanics. Computational mechanics simulations approach the problem mainly through inviscid-viscous methods thus promising reduced computational time. AEROHEAT and INCHES are two of the simpler methods to approach the phenomenon of aerodynamic heating [2]. Both methods use the axisymmetric analog concept that allows axisymmetric boundary layer techniques to be applied to three-dimensional flows, provided that the surface streamlines are known. AEROHEAT calculates approximate surface streamlines based solely on the body geometry. INCHES uses an approximate expression for the scale factor in the windward and leeward planes, which describes the spreading of surface streamlines. An empirical relation then generates circumferential heating rates.

DRA Farnborough developed the SAPPHIRE software that is capable of calculating the surface temperatures and the characteristics of the flow field for a given geometry and defined flight characteristics. The above software is a series of codes that use PHOENICS [3] as the main CFD solver. The main advantage of CFD techniques is that aerodynamic heating can be related to other phenomena, as well, such as conjugating heat transfer and providing more detailed results. In order for SAPPHIRE to provide reliable results on the thermal trace, aerodynamic heating of the body has to be calculated with an error that does not exceed 5% [4]. For this purpose, a PHOENICS-based code was developed that has the possibility to validate results with available experimental data. The purpose of the present work is to make the model more time efficient and more accurate, producing results closer to the available experimental data.

According to finite volume or codes with FEM, attempts have been made, with acceptable results, by means of conjugating CFD and FEM. Murakami et al. [5] used CFD coding for the Navier-Stokes equations to calculate the outer flow, while the finite element method was used to perform the thermal analysis via equations describing unsteady heat conduction for a 3D field. The results were impressive, as

they were very close to the experimental data measured in a wind tunnel experiment. Lu Jianwei and Wang Qiang [6] in order to calculate the emitted IR radiation suggested a division of the computational grid into two regions: the fluid and the solid. The fluid region is modeled by the Navier-Stokes equations, while turbulence is modeled by the RNG k-ε model. In the solid region, the energy transfer equation is used. In a similar study for calculating the emitted IR radiation, Marlene Johansson and Mats Dalenbring [7] developed the SIGGE software. SIGGE uses inputs of temperature, pressure, and species distribution that have been roughly estimated beforehand, together with the grid of the geometry being studied. The Navier-Stokes equations are solved by the VOLSOL solver, while turbulence is described by the k-ε model.

Apart from CFD methods, attempts have been made to simulate phenomena that involve aerodynamic heating via other methods as well. Rodrigo C. Palharini and Wilson F. N. Santos [8] used the Direct Simulation Monte Carlo (DSMC) method to simulate a two-dimensional steady supersonic flow in an orthogonal cavity. Main interests of this study were the characteristics of the aerodynamic surface, such as heat transfer coefficients, etc. Another method introduced by Georgia Tech Research Institute [9] named GTSIG (Georgia Tech Signature Inviscid Model) involves the calculation of temperature distribution by creating thermal meshes and partial differential equations. Finally, Christopher J. Riley et al., in their study [2], developed a 3D technique without viscous calculations that has the ability to calculate the degree of surface heating. Surface streamlines are calculated from the inviscid solution and the axisymmetric analog. Then, they are used in combination with an equation for convective heat transfer, to calculate the total surface heat transfer. The results of this method are satisfying as they are close to experimental data and the results of both the Navier-Stokes and the VSL equation solutions.

2. Mathematical modeling

2.1 Governing equations

In order to describe the phenomena under investigation, use is made of the conservation equations describing a three-dimensional, single phase, turbulent, steady state flow. The above equations are formulated in such a manner as to incorporate the physical modeling of the case study under the following assumptions:

- One phase, steady-state flow

- Compressible fluid

- Newtonian fluid

- Absence of chemical reaction

It is also clear that because of the general geometries considered, the equations must be modified in a way to be suitable for use in a body-fitted coordinate (BFC) system.

2.1.1 Modification of conservation equations from Cartesian coordinate system to BFC

Assuming that $\vec{X} = (X_1, X_2, X_3)$ the Cartesian coordinate system, where X_j are the Cartesian Coordinates and $\vec{i_j}$ the direction unit vectors, the velocity $\vec{V}$ can be expressed as:

$$\vec{V} = \sum_{j=1}^{3} u_j \vec{i_j} = u_1 \vec{i} + u_2 \vec{j} + u_3 \vec{k}.$$

Furthermore,

$$\vec{\nabla} = \sum_{i=1}^{3} \vec{i_j} \frac{\partial}{\partial x_j} \tag{1}$$

Assume a non-orthogonal coordinate system, defined as $\xi_\eta = \xi_\eta(X_1, X_2, X_3)$, $\eta = 1,2,3$, where ξ_η are the curvilinear coordinates at any point and X_1, X_2, X_3 its Cartesian coordinates. Assume $\vec{g_\eta}$ to be the non-orthogonal unit vectors along the directions of the curvilinear coordinates; then the components of the velocity vector tangent to the unit vectors $\vec{g_\eta}$ can be defined as:

$$V_\eta = \vec{g_\eta}\vec{V} = \sum_{j=1}^{3} g_{\eta j} U_j, \eta = 1, 2, 3 \tag{2}$$

where U_j are the Cartesian components and the unit tangent vectors alongside the three directions are:

$$\vec{g_\eta} = \vec{X}_{,\xi\eta} \Big/ \left| \vec{X}_{\xi\eta} \right| = \sum_{j=1}^{3} \vec{g}_{\eta j} \vec{i_j}, \eta = 1, 2, 3 \tag{3}$$

where $\vec{X}$ is the position vector of a point and the index ξ_η denotes the partial derivative to the curvilinear coordinate ξ_η.

2.1.2 Conservation of momentum

In order to obtain the resolute [10] of the momentum equation in each of the coordinate directions, we form the dot product of tangent unit vectors with the momentum equation (Eq. (1)). The momentum equation, considering the assumptions and the physics of this simulation, is derived as follows:

$$\rho \left[\left(\vec{\nabla}\vec{V} \right) \vec{V} \right] - \vec{\nabla} \cdot \tilde{\tau} = -\vec{\nabla}p + \vec{F}, \tag{4}$$

where

$$\vec{\nabla} \cdot \tilde{\tau} = \left(\vec{\nabla}\mu\vec{\nabla} \right)\vec{V} + \sum_{\lambda=1}^{3} \left[\sum_{j=1}^{3} \frac{\partial}{\partial x_j} \left(\mu \frac{\partial u_j}{\partial x_\lambda} \right) \right] \vec{i_\lambda} \tag{5}$$

In order to obtain the resolute of the momentum equation in each of the coordinate directions, the dot product of the tangent unit vector and the above momentum equation is formed:

$$\vec{g_n}\rho \left[\left(\vec{\nabla}\vec{V} \right)\vec{V} \right] - \vec{g_n}\vec{\nabla} \cdot \tilde{\tau} = -\vec{g_n}\vec{\nabla}p \leftrightarrow \vec{g_n}\left(\rho\vec{V} \cdot \vec{\nabla} \right)\vec{V} - \vec{g_n} \cdot \left(\vec{\nabla} \cdot \mu\vec{\nabla} \right)\vec{V} - \vec{g}_n \cdot S_\mu$$
$$= -\vec{g_n}\vec{\nabla}p \tag{6}$$

where $S_\mu = \sum_{\lambda=1}^{3} \left[\sum_{j=1}^{3} \frac{\partial}{\partial x_j} \left(\mu \frac{\partial u_j}{\partial x_\lambda} \right) \right] \vec{i_\lambda}$

From vector calculus, using the identity $A\text{x}(B\text{x}C) = B(A \cdot C) - C(A \cdot B)$, we have:

$$\vec{\nabla}\left(\vec{g}_n \cdot \rho\vec{V}\right) = \left(\rho\vec{V} \cdot \vec{\nabla}\right)\vec{g}_n + \left(\vec{g}_n \cdot \vec{\nabla}\right)\rho\vec{V} + \rho\vec{V}\text{x}\left(\vec{\nabla}\text{x}\vec{g}_n\right) + \vec{g}_n\text{x}\left(\vec{\nabla} \text{ x } \rho\vec{V}\right) \quad (7)$$

Also,

$$\vec{V} \cdot \vec{g}_n\text{x}\left(\vec{\nabla}\text{x}\vec{V}\right) = -\vec{g}_n \cdot \left(\vec{V}\text{x}\left(\vec{\nabla}\text{x}\vec{V}\right)\right)\vec{V} \quad (8)$$

$$\left(\vec{V} \cdot \vec{\nabla}\right)\vec{V} = \vec{\nabla}\left(\frac{|V_n|^2}{2}\right) - \vec{V}\text{x}\left(\vec{\nabla}\text{x}\vec{V}\right) \quad (9)$$

$$\vec{V} \cdot \vec{V}\text{x}\left(\vec{\nabla}\text{x}\vec{g}_n\right) = \left(\vec{V}\text{x}\vec{V}\right) \cdot \left(\vec{\nabla}\text{x}\vec{g}_n\right) = 0, \, since \, \vec{V}\text{x}\vec{V} = 0 \quad (10)$$

Thus,

$$\vec{g}_n \cdot \vec{\nabla}\left(\frac{|V_n|^2}{2}\right) = \vec{V} \cdot \left(\vec{g}_n \cdot \vec{\nabla}\right) \cdot \vec{V}$$

Forming the dot product of the above equation and (Eq. (7)), we have:

$$\left(\rho\vec{V} \cdot \vec{\nabla}\right)\vec{V}_n = \vec{V} \cdot \left(\rho\vec{V} \cdot \vec{\nabla}\right)\vec{g}_n + \vec{g}_n \cdot \left(\rho\vec{V} \cdot \vec{\nabla}\right)\vec{V} \quad (11)$$

Also, for a scalar variable φ_n:

$$\vec{\nabla} \cdot \left(\rho\vec{V}\varphi_n\right) = \rho\vec{V} \cdot \vec{\nabla}\varphi_n \quad (12)$$

and

$$\left(\vec{\nabla} \cdot \mu\vec{\nabla}\right)\vec{V} \cdot \vec{g}_n = \vec{g}_n \cdot \left(\vec{\nabla} \cdot \mu\vec{\nabla}\right)\vec{V} + \vec{V} \cdot \left(\vec{\nabla} \cdot \mu\vec{\nabla}\right)\vec{g}_n \quad (13)$$

Using Eqs. (11)–(13), we can write (Eq. (6)), as follows:

$$\vec{\nabla} \cdot \left(\rho\vec{V}V_n\right) - \left(\vec{\nabla} \cdot \mu\vec{\nabla}\right)V_n - \vec{g}_n \cdot \vec{S}_\mu = -g_n\vec{\nabla}p + \vec{V}\left(\rho\vec{V} \cdot \vec{\nabla}\right)\vec{g}_n - \vec{V}\left(\vec{\nabla} \cdot \mu\vec{\nabla}\right)\vec{g}_n \quad (14)$$

and

$$\left(\vec{V} \cdot \vec{\nabla}\right)V_n = \vec{V}\left(\vec{V} \cdot \vec{\nabla}\right)\vec{g}_n + \vec{g}_n\left(\vec{V} \cdot \vec{\nabla}\right)\vec{V}$$

From Eqs. (1) and (3), the partial derivative in the direction ξ_n is:

$$\frac{\partial}{\partial\xi_n} = \vec{g}_n \cdot \vec{\nabla} = \sum_{j=1}^{3} g_{nj}\frac{\partial}{\partial x_j} \quad (15)$$

With inverse

$$\frac{\partial}{\partial x_n} = \sum_{j=1}^{3} G_{nj}\frac{\partial}{\partial\xi_j} \quad (16)$$

where $G_{n,j}$ the elements of the inverse matrix of the elements $g_{n,j}$.

2.1.3 Conservation of mass

Since the case study is for steady flow, the conservation of mass equation is hence simplified in the following form for the Cartesian coordinate system:

$$div(\rho V) = \frac{\partial\left(\rho \vec{V}\right)}{\partial x} + \frac{\partial\left(\rho \vec{V}\right)}{\partial y} + \frac{\partial\left(\rho \vec{V}\right)}{\partial z} = 0$$

Using body-fitted coordinates, the continuity equation must be solved in terms of the velocity components along the coordinate directions. These components, u_n, would be $V = \sum_{n=1}^{3}\vec{g}_n u_n$ and are calculated from the velocity resolutes by solving the simultaneous equations

$$V_n = \sum_{j=1}^{3}\vec{g}_n \cdot \left(\vec{g}_j u_j\right), n = 1, 2, 3. \tag{17}$$

Velocity components in terms of the resolutes are

$$u_n = \sum_{j=1}^{3}G_{n,j}V_j, \text{n} = 1, 2, 3 \tag{18}$$

where

$$G_{n,j}/_\sigma = \begin{bmatrix} (1-c^2) & (bc-a) & (ac-b) \\ (bc-a) & (1-b^2) & (ab-c) \\ (ac-b) & (ab-c) & (1-a^2) \end{bmatrix} \tag{19}$$

where

$$a = g_1 \cdot g_2, \text{b} = g_1 \cdot g_3, \text{c} = g_2 \cdot g_3 \tag{20}$$

and

$$\sigma = \left[1 - \left(a^2 + b^2 + c^2 - 2abc\right)\right] \tag{21}$$

Using Eqs. (1) and (18), the following expression for the velocity is derived:

$$\vec{V} = \sum_{n=1}^{3}\vec{i}_n \sum_{j=1}^{3}G_{n,j}V_j = \sum_{j=1}^{3}\vec{Q_j}\vec{V}_j \tag{22}$$

where

$$\vec{Q_j} = \sum_{j=1}^{3}G_{n,j}\vec{i}_n \tag{23}$$

the vector used to obtain the resolutes (projections) of the velocity vector $\vec{V}$. From Eqs. (1), (16), and (20):

$$\vec{\nabla} = \sum_{j=1}^{3} \vec{Q}_j \frac{\partial}{\partial \xi_j} \tag{24}$$

Finally, the continuity equation can be written as $\vec{\nabla}\left(\rho\vec{V}\right) = 0$ where

$$\vec{V} = \sum_{n=1}^{3} \vec{g}_n u_n \tag{25}$$

2.2 Turbulence modeling

In order to evaluate the use of different turbulence models in the cases under consideration, a parametric study was accomplished by trying three "popular" turbulence models: (i) standard k-ε model, (ii) RNG k-ε model, and (iii) k-ω model. The k-ε model simulation was chosen in order to reproduce the original simulation accomplished by Steve Rooks [4]. In order to take it one step further and include the effect of the swirling of the flow, another simulation was performed using the RNG k-ω model. Last but not least, the k-ω turbulence model was used as well, as preliminary studies proved its suitability for wall-bounded flows.

2.2.1 The general φ-equation

By generalizing Eq. (14), the appropriate equation for any scalar variable can be provided [11]:

$$\vec{\nabla} \cdot \vec{Q} = S\varphi_n \tag{26}$$

where

$$\vec{Q} = \rho\vec{V}\varphi_n - \overrightarrow{\Gamma_{\varphi_n}}\vec{\nabla}\varphi_n \tag{27}$$

and φ a general scalar variable like H (enthalpy), k, ε, etc. Regarding k (turbulence kinetic energy) and ε (turbulence dissipation rate):

$$S_k = G - \rho\varepsilon \tag{28}$$

$$S_\varepsilon = {C_1\varepsilon}/{_{kG}} - {C_2\rho\varepsilon^2}/{_\kappa} \tag{29}$$

$$G = \mu\left({\partial u_j}/{_{\partial x_i}} + {\partial u_i}/{_{\partial x_j}}\right){\partial u_j}/{_{\partial x_j}}, in \ Cartesian - tensor \ form \tag{30}$$

where u_i, u_j the velocity components in the direction of the Cartesian coordinates x_i, x_j with i = 1,2,3 and j = 1,2,3 [10]. It must also be noted that the effective exchange coefficients for k, ε are as follows:

$$\mu_l + \mu_t = \mu \tag{31}$$

$$\mu_t = \rho C_\mu \frac{k^2}{\varepsilon} \tag{32}$$

$$\Gamma_k = {(\mu_l+\mu_t)}/{_{\sigma_{k,t}}} \tag{33}$$

$$\Gamma_\varepsilon = {(\mu_l+\mu_t)}/{_{\sigma_{\varepsilon,t}}} \tag{34}$$

where μ_l is the laminar viscosity; C_1, C_2, and C_μ are turbulence model constants; and $\sigma_{k,t}$ and $\sigma_{\varepsilon,t}$ are the turbulence Prandtl numbers for k, ε [10].

In total seven differential equations are solved, namely, the continuity equation, the three momentum equations, the enthalpy equation, and the two equations for the turbulence variables.

2.2.2 The near-wall region

Special attention was given to the treatment of the near-wall region, as it is of high importance for the type of flows studied and the 2-equation models used to simulate turbulence do not, in general, produce results of high accuracy in near-wall regions. The near-wall region was treated via a log-law wall function that also played a major role in deciding the computational grid as well as ensuring computational economy since there is no need to solve throughout the viscous sub-layer. The use of this method was introduced by Launder and Spalding [12], and the formula used is:

$$\frac{ln\,(EY^+)}{k} = \frac{U}{U_\tau} \tag{35}$$

where
U: the absolute velocity parallel to the wall in the first node of the grid
U_τ: the friction velocity
k: the Von Karman constant
E: the surface's roughness parameter
Y^+: the dimensionless distance from the wall
The above function is applied to nodes whose dimensionless distance from the wall is between 30 and 130. In this region of the boundary layer, the effects of turbulence and viscosity are equally important.

2.3 Boundary conditions

Because of the selection of body-fitted coordinates to design the grid of the problem, the velocity must be broken down to its components and transferred from the Cartesian coordinate system to the BFC used in the present study.

At entrance, a uniform flow is applied of Mach 2 speed. The rate of flow is consistently calculated for each control volume. The kinetic energy of turbulence and its rate of dissipation are considered constant with values of 21.78 m^2/s^2 (10% of the mean velocity squared) and 2.765*10^5 m^2/s^3 (assuming turbulence viscosity 1000 times the laminar value), respectively (**Figure 1**).

The outlet boundary conditions describe the fact that there is no alteration in the rate of mass flow, as there is neither mass creation nor destruction. As for the turbulence kinetic energy, turbulence dissipation rate, and the enthalpy, Neumann conditions prevail, suggesting there is no alteration of values regarding these

Figure 1.
The plane of inlet boundary conditions specification.

Figure 2.
The plane of outlet boundary conditions specification.

properties along the boundary (**Figure 2**). Since the boundary conditions must be transported in the BFC system, the Jacobian of the transformation used is:

$$J = \frac{\partial x}{\partial g_1}\frac{\partial y}{\partial g_2} - \frac{\partial x}{\partial g_2}\frac{\partial y}{\partial g_1}$$

and the general form of the functions:

$$\frac{\partial f}{\partial x} = \frac{1}{J}\left(\frac{\partial f}{\partial g_1}\frac{\partial y}{\partial g_2} - \frac{\partial f}{\partial g_2}\frac{\partial y}{\partial g_1}\right)$$

$$\frac{\partial f}{\partial y} = \frac{1}{J}\left(\frac{\partial f}{\partial g_2}\frac{\partial x}{\partial g_1} - \frac{\partial f}{\partial g_1}\frac{\partial x}{\partial g_2}\right)$$

Finally, the boundary condition at the northern boundary is prescribed external pressure. Like the boundary conditions at the outlet, the kinetic energy of turbulence, its dissipation rate, and the enthalpy are described by Neumann boundary conditions, implying absence of factors capable of altering their values along the northern boundary.

2.4 Computational grid and method used

2.4.1 Computational grid generation

The study for grid independence came down to the same results as the one proposed by Steve Rooks [4]. The computational grid used is one with dimensions 48*45*1 and has been proved to lead to grid-independent results [4]. Briefly, the grid divides the computational field in three regions along the x-axis and three along the y-axis, as one can see in the following figure (**Figure 3**).

Along the y-axis the three sub-regions correspond to the area below the lip, the area of the lip, and finally the area above the lip. A most important role in the dimensions of the grid played the fact that a denser or a sparser grid would result in improper use of the wall functions, as it would affect the dimensionless distance Y+.

2.4.2 Computational methods used

In order to solve the equations, the finite-volume method is employed. As for regular grids, the finite-volume equations can be derived by integrating over a control volume in a system with body-fitted coordinates. The use is made of the Gauss theorem that transforms a volume integral to a surface one:

$$\int_{\Delta V} \vec{\nabla} \cdot \vec{Q}\, dV = \int_S \vec{n} \cdot \vec{Q}\, dS = \int_S \vec{n} \cdot \left(\rho\vec{V}\varphi_\eta\right)dS - \int_S \vec{n} \cdot \left(\overrightarrow{\Gamma_{\varphi_\eta}}\vec{\nabla}\varphi_\eta\right)dS \qquad (36)$$
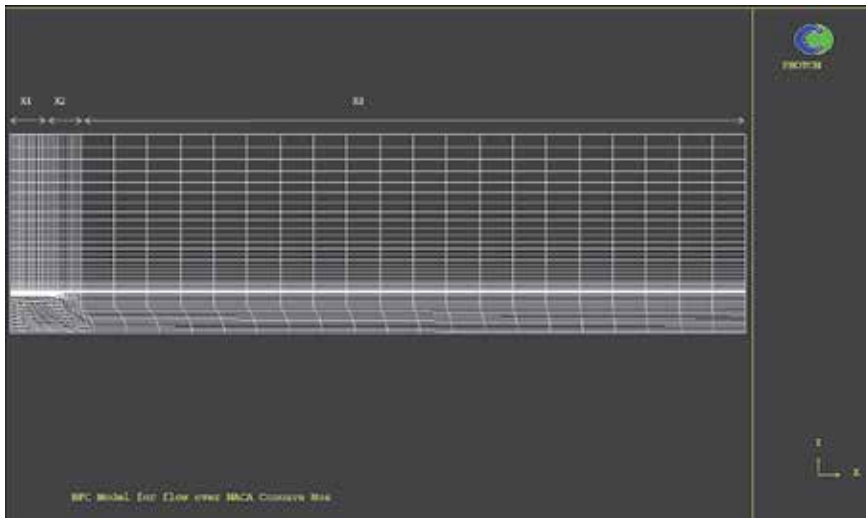
Figure 3.
The computational grid.

where $\vec{n}$ is the outward vector drawn normal to any of the six surfaces defining ΔV and S denotes the enclosing the volume surface area [10]. The first term represents convection, where properties are regarded as uniform over the cell faces, except in respect of the velocities for which the face-center values are stored. The values prevailing at the cell face are determined by using upwind interpolation. As for the second term, the one representing diffusion the property gradients and the transport properties that they multiply are uniform over cell faces. In order to calculate the gradients, it is supposed that properties vary linearly and also the transport properties are arithmetic averages of those on either side of the cell faces. In source terms, the nodal values are supposed to prevail over the whole of the cell volume.

Any dependent variable's partial differential equation is represented by a coupled set of algebraic equations of the following form:

$$A_P\varphi_P = \sum_i A_i\varphi_i + S_\varphi \qquad (37)$$

where the A_i's represent the influence of convection and diffusion, S_φ is the source term, and P refers to the control volume under consideration. Σ_i indicates the summation over the neighboring nodes. All the above equations are derived through work that cannot be presented here due to limited space [10].

2.4.3 Numerical simulation

The numerical simulations in this work are realized by the fluid dynamics package PHOENICS. The SIMPLEST algorithm is used in the iterative procedure, whereas the equations are solved via the finite-volume method. The momentum equations are solved using the initial estimate of the pressure field, using velocities that do satisfy momentum but not in the general continuity. For each cell, the equation of (inlet-outlet) is formed, and an equation of pressure correction is solved where the coefficients are A (d(vel))/dp and the sources are the errors in continuity. Afterwards, the pressure field is corrected alongside with the velocity field.

The iterative procedure continues until the errors in the equations of momentum and continuity are acceptable.

2.5 Relaxation methods used

In order to improve convergence and eliminate great fluctuations in values of variables in consecutive iterations that could lead to the divergence of the solution, relaxation techniques are used. In the present study, two techniques are used: the linear relaxation and the false time-step relaxation. Linear relaxation is used for the variables of pressure, enthalpy, turbulence kinetic energy, and turbulence dissipation rate as it is more suitable for scalar variables in the following form: $\varphi^{new} = \varphi^{old} + \alpha(\varphi^{new} - \varphi^{old})$. In the case of the vector variables of U1 and V1, false time-step relaxation is used as it is more suitable for the velocity variables in the following form $\rho V_P / \delta t (\Phi^* - \Phi_\rho) = \beta(\Phi^* - \Phi_\rho)$ where V_P is the cell volume, Φ^* the previous iteration value of variable Φ, Φ_ρ the value of φ in the last iteration, and δt_{false} the false time step, generally of the order of the cell residence time.

2.6 Discretization schemes used

In the original coding, the Hybrid discretization scheme was used. However, in order to investigate further the most efficient way to simulate the phenomenon, runs were also carried out using the upwind discretization scheme that, according to literature, is more efficient when describing directional flows but introduces more "false-diffusion" errors.

2.7 Modifications in the original coding

In order to improve the simulation results both in terms of convergence speed and agreement with the experimental data, numerous modifications were made to the original coding. These modifications include the calculation of the diffusion coefficient by means of the harmonic mean and not the numerical mean, and the calculation of reference kinematic viscosity for laminar flow was accomplished via Sutherland's law. Moreover, the initial values of the variables for enthalpy and velocity were not chosen randomly, as in the original coding but were calculated based on the simulation's data so as to help the convergence procedure with more "realistic" initial variable values. At the northern boundary, a boundary condition that suggests constant mass flow was used so as to ignore the effects of diffusion. Finally, in opposition to the initial coding, where false time-step relaxation was used for the variables of enthalpy, turbulence kinetic energy, and turbulence dissipation rate, in the modified version, for these variables, linear under-relaxation was used.

2.8 Different case studies

In terms of this present research, many simulations were carried out, and results of the most relevant eight of them were brought into comparison in order to decide which method is more efficient in simulating the phenomenon studied by Markley et al. [13]. The first simulation carried out in terms of this research was the reproduction of the simulation carried out by Steve Rooks [4] in an up-to-date version of the PHOENICS. The other seven include the modified original version, described in the above paragraph, although no alteration in either the turbulence model or the discretization scheme was made. The other six were the combinations of the three turbulence models (k-ε, RNG k-ε, and k-ω) with the two discretization schemes (Hybrid and Upwind) studied in this research paper.

3. Results

In order to examine the validity of the results of the simulation, a comparison had to be made with the available experimental data. The available experimental data are for temperature, as that was the main point of interest at the experiment conducted by NACA [13], measured behind the lip, and high enough so as the flow would be unaffected by boundary layer phenomena. As a result, measurements were taken along the line Y = 18 and behind the region dictated by cell X = 20.

The first simulation carried out in terms of this research was the reproduction of the simulation carried out in [4] using our modified version of the PHOENICS code, so as comparison can be carried out. The modifications made to the original coding that led to improved results, both in terms of agreement with the experimental data and in terms of decreased convergence time, include the calculation of the diffusion coefficient by means of the harmonic mean rather than the numerical mean and the calculation of reference kinematic viscosity for laminar flow that was accomplished via Sutherland's law. Moreover, the initial values of the variables for enthalpy and velocity were not chosen randomly, as in the original coding, but were calculated based on the simulation's data so as to help the convergence procedure with more "realistic" initial variable values. At the northern boundary, a boundary condition that suggests constant mass flow was used so as to ignore the effects of diffusion. Finally, different to the initial coding, where false time-step relaxation was used for the variables of enthalpy, turbulence kinetic energy, and turbulence dissipation rate, in the modified version, for these variables, linear relaxation was used.

For this initial modified version, no alterations were made as far as the turbulence modeling and the discretization scheme are concerned. The initial modeling with k-ε turbulence modeling and the Hybrid discretization scheme were used. As a result of the above changes, the convergence of the coding was faster by 48.33% as convergence was reached at 5427 iterations instead of 10,503 for the same level of errors remaining, and there were even slight improvements in the agreement with the experimental results as well.

The following diagram depicts the distribution of temperature along the x-axis above the airfoil at the height of the line Y = 18, as mentioned above (**Figure 4**).

As seen in the above diagram, the two simulations differ only slightly, and it can be noted that the modified version offers a marginal 0.04% better accuracy along with the faster convergence. More precisely, at the point where the temperature drop is noticed, which is the lip region, the accuracy is improved by 0.015%,
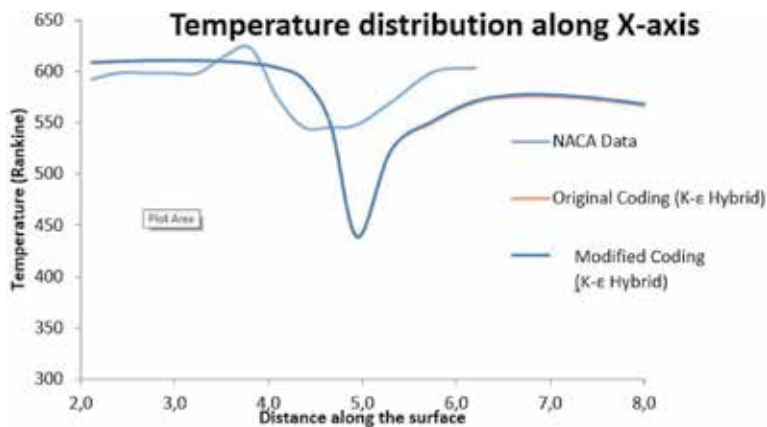

Figure 4.
Comparison diagram for temperature distribution along the x-axis.

whereas after the threshold of 5.3 cm, which is behind the lip region, the accuracy is improved by 0.27%.

Likewise, the diagrams depicting the main velocity and density distribution along the x-axis slightly differ from the diagrams of the initial simulation since the mean fault is 0.5847 and 0.9%, respectively (**Figures 5** and **6**).

Regarding the distributions of temperature, velocity and density along the Y-axis, defined by the line X = 20 (**Figures 7–9**), no major difference is noticeable in
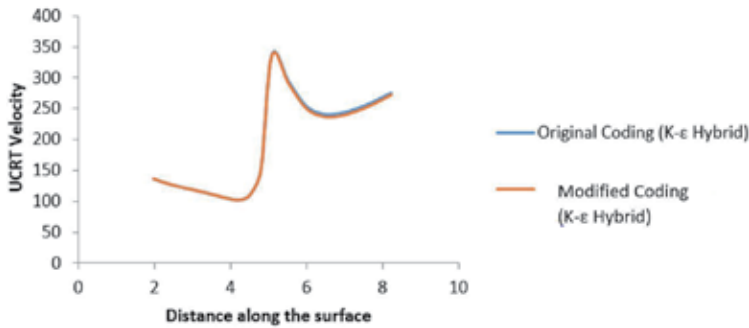
Figure 5.
Comparison diagram for velocity distribution along the x-axis.
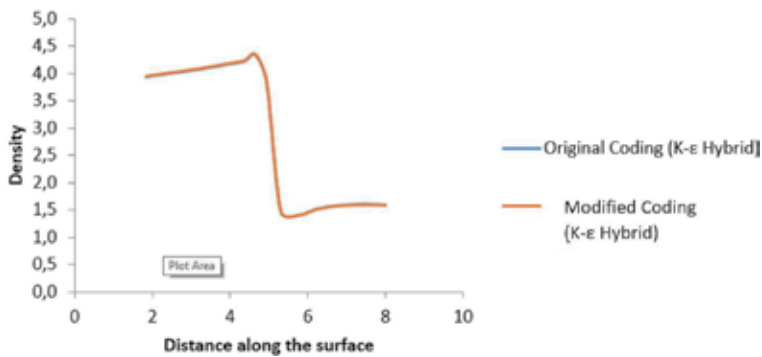
Figure 6.
Comparison diagram for density distribution along the x-axis.
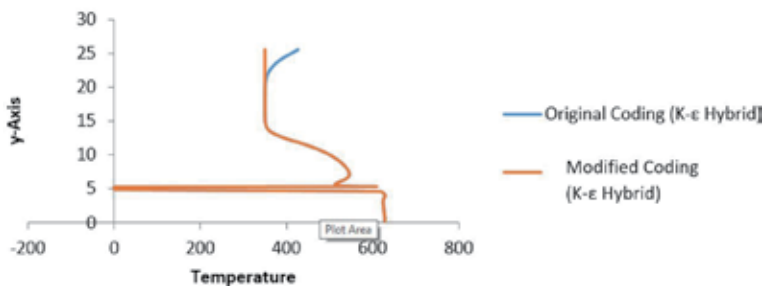
Figure 7.
Comparison diagram for temperature distribution along the y-axis.
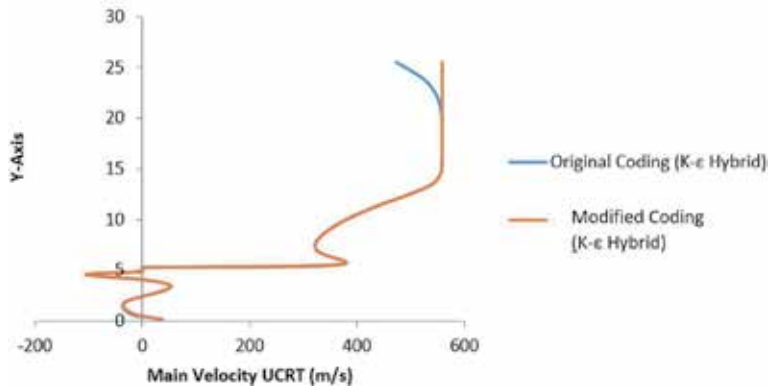
Figure 8.
Velocity distribution along Y-axis.
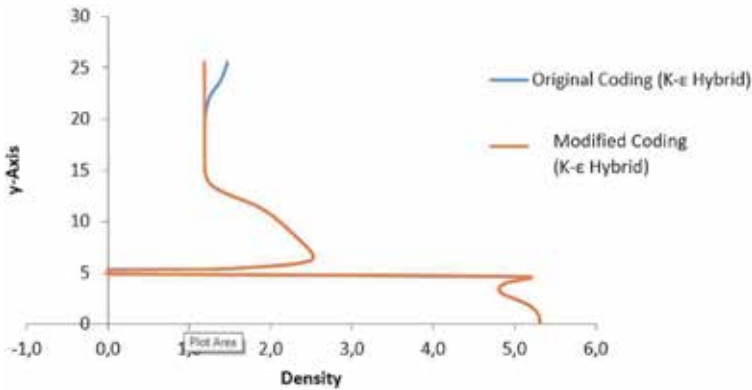
Figure 9.
Density distribution along Y-axis.

their main part, as one can notice from **Figures** 7–**9**. The mean errors are 0.7, 3.06, and 0.9%, respectively. Yet, reaching the northern boundary, the results from the modified simulation differ from the initial one, as they do not alter the value they have settled in following the exit of the boundary layer. In the initial simulation, an increase can be spotted for the variables of temperature and density and a decrease in the value of velocity. The increase in the temperature value along with the decrease in velocity can be explained from the fact that enthalpy is assumed constant. However, in the modified simulation, the steady mass flow boundary condition neglects diffusion phenomena, and therefore there is stability in this variable. This approaches the nature of the original experiment, as no factors able to alter the values of these variables exist near the northern boundary.

   Figures 10–13 present the contour plots for temperature, density, and velocity distributions as well as the vector diagram of the velocity vectors.

   In order to investigate further the problem and any possible aspects that may improve the quality of the results produced, a parametric study was conducted. The parameters studied were both the turbulence model and the discretization scheme. Simulations were conducted using all three different turbulence models: k-ε, RNG k-ε, and k-ω. Each of the above turbulence models was used in combination with either the Hybrid discretization scheme or the Upwind.
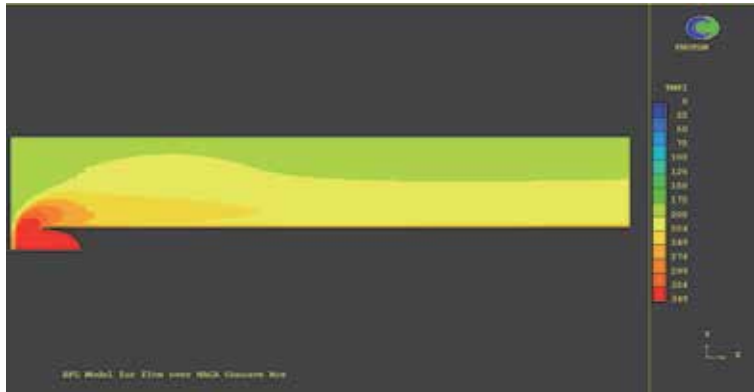
Figure 10.
Contour plot of the temperature distribution on the computational field for the modified simulation (k-ε hybrid).

Figure 11.
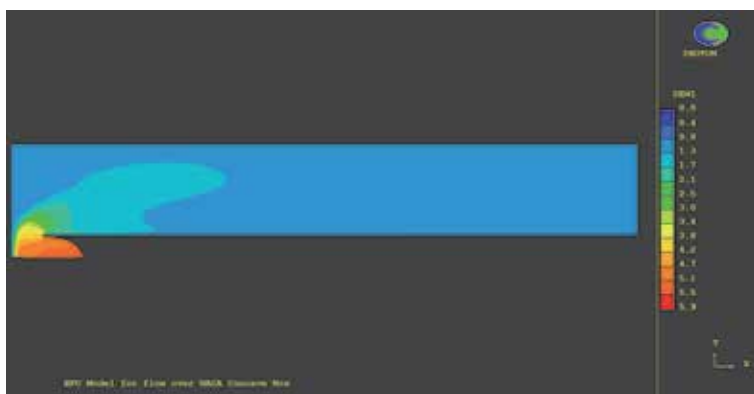*Contour plot of the velocity distribution on the computational field for the modified simulation (k-ε hybrid).*

Figure 12.
Contour plot with the density distribution on the computational field for the modified simulation (k-ε hybrid).

In total, six different simulations were performed. The results were compared to the available experimental data in order to evaluate their accuracy. The schematic of the comparison can be seen in the diagram that follows (**Figure 14**).
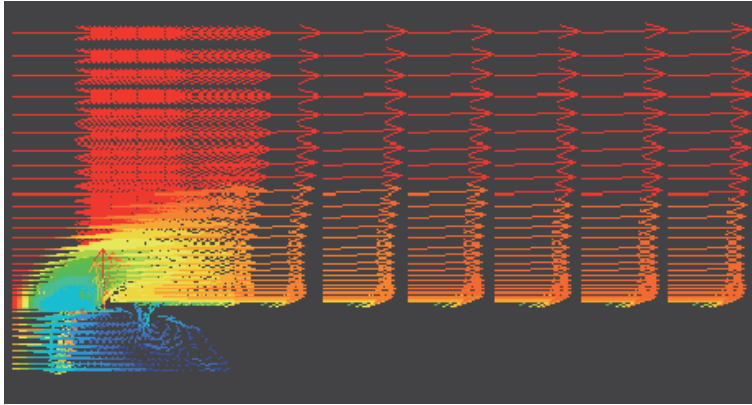
Figure 13.
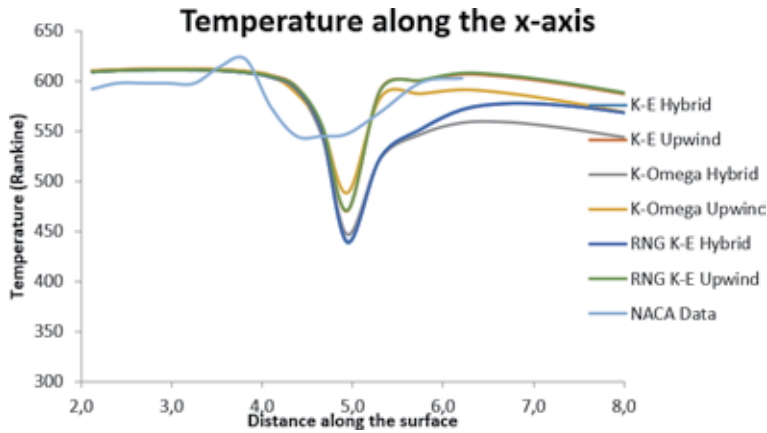*Velocity vectors zoomed in the area of interest depicting the recirculations.*

Figure 14.
Comparison diagram of parametric simulations and experimental data.

The simulation results can also be seen in numbers in the following table, where the mean error is calculated (**Table 1**).

As one can see, the most successful simulation in terms of the overall mean error is the one engaging the k-ω turbulence model in combination with the Upwind discretization scheme. If we take a closer look, it is obvious that it is the only simulation that seems to approach the steep temperature descent in the 4–5 cm region. In that region, all simulations fail to keep the mean error below 5%; however, as one can see in the following table, the k-ω Upwind simulation achieves a mean error of 5.6274% (**Table 2**).

The difficulty in simulating realistically the behind the lip region is possibly due to heat conduction phenomena. In the simulations performed, no solution is run for conjugate heat transfer, and given that the airfoil geometry is very thin, heat

	k-ε Hybrid	k-ε Upwind	RNG k-ε Hybrid	RNG k-ε Upwind	k-ω Hybrid	k-ω Upwind
Overall mean error (%)	4.9529	3.5055	4.9729	3.5741	5.034	3.3418

Table 1.
Overall mean error calculation.

	k-ε Hybrid	k-ε Upwind	RNG k-ε Hybrid	RNG k-ε Upwind	k-ω Hybrid	k-ω Upwind
Mean error in region 4–5 cm (%)	8.42	6.763	8.4331	6.8564	8.0097	5.6274

Table 2.
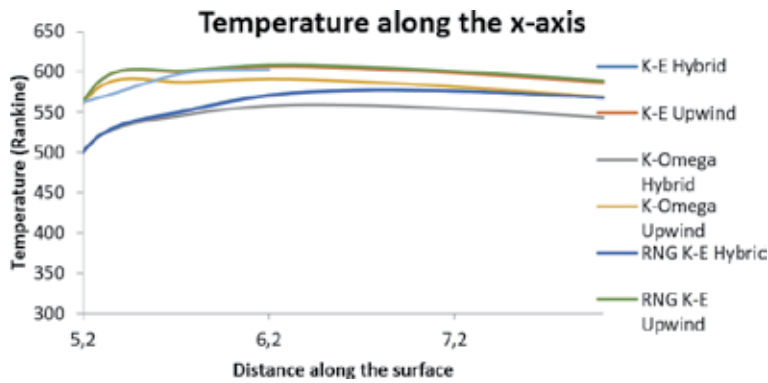*Mean error calculation in the 4–5 cm region.*

Figure 15.
Comparison diagram between simulation performed and experimental data in the behind the lip region.

	k-ε Hybrid	k-ε Upwind	RNG k-ε Hybrid	RNG k-ε Upwind	k-ω Hybrid	k-ω Upwind
Mean error in behind the lip region (%)	6.5465	0.3348	6.6621	0.6050	8.0915	1.9930

Table 3.
Mean error calculation in behind the lip region.

conduction taking place on the edge of the lip is speculated to be one among the causes that lead to higher calculated temperatures than the experimental data.

When examining the region behind the lip, where the flow presents a more stabilized form than the one when encountering the lip, the turbulence model that achieves better accuracy is the RNG k-ε model with the Upwind discretization scheme. This can be seen in both the diagram and the table that follow (**Figure 15** and **Table 3**).

It must be noted that in all simulations performed, the discretization scheme that produced the best results was the Upwind scheme. That would be justified by the fact that the flow is basically unidirectional and is characterized by high velocity. As a result, the diffusion phenomena are of very low intensity, with the convective phenomena being the main terms in the discretization equation. In both k-ω and k-ε simulations ran, the benefits from altering the initial code were still valid.

4. Recommendations

The calculation of aerodynamic heating phenomena includes many aspects that can interfere with both the speed of convergence but the accuracy of the results as well. Apart from the choice of proper initial value and other numeric factors, attention has to be paid to the flow field characteristics in order to decide the suitability of the turbulence model and the discretization scheme that will be

used in order to achieve better results. Despite the fact that improvements for the 4–5 cm region were also suggested here, future research could focus on simulating the lip region, as this study's main interest lied in the behind the lip region. In order to achieve that, high-order discretization schemes could be used, like the Van Leer scheme as well as high-order turbulence models, like the large eddy simulation (LES) and the direct numerical simulation (DNS) or any combinations.

5. Conclusion

Heat transfer and pressure measurement on a 5-inch hemispherical concave nose at a Mach number of 2.0 is investigated via the use of PHOENICS to evaluate aerodynamic heating phenomena. In continuation of [4], the code is modified in order to achieve better results both in terms of faster convergence but also in terms of more accurate results as well. Finite-volume method is used, while turbulence models and discretization schemes are studied as parameters in order to optimize results. Before altering the above mentioned parameters, attempts were made to improve the speed of convergence. Altering the values of input variables in order to be closer to the problem considered as well as choosing relaxation methods suitable for each variable type, scalar or vector, along with a few other changes described above, managed to improve the convergence speed by up 48.33%. Moreover, an improvement in boundary conditions of the northern boundary so as to ignore dissipation phenomena corrected the results of all variables at the northern region of the computational field, as their values were stabilized, as expected. In the parametric study, the main observation was that the discretization scheme plays a major role in the quality of the results, as the flow is unidirectional and is characterized by high speed of 2.0 Mach. As a result, dissipation phenomena are not comparable to convection, which plays the major role. The choice of the Upwind discretization scheme seems to be more accurate, as it considers the fact that the flow is unidirectional and provides results improved by more than 1.5% for given turbulence model on the whole computational field. That improvement can go up to 6% when discussing regions behind the lip, where the flow has been stabilized.

The parametric study regarding the turbulence model produced interesting results, as well. In order to evaluate solely the impact of the turbulence model, the discretization scheme used was the Hybrid, as in the original. As it appears, there is not only one fitting turbulence model for this simulation, as their suitability changes with regions. When studying the flow field in the lip region (4–5 cm), the k-ω turbulence model gave the best results, improved by 0.5% when compared to the original simulation performed with k-ε turbulence model. The improvement introduced by the use of the k-ω model in that area is due to the fact that this model can calculate better the effect of the created vortices. When both k-ω turbulence model and Upwind discretization scheme were implied, the total improvement in that area of interest went up to almost 3% (5.6274% discrepancy from the experimental data, compared to 8.42%). However, the study showed that behind the lip (x > 5.2), where flow has been stabilized, the use of the RNG k-ε turbulence model combined with the Upwind discretization scheme improved the mean error by more than 6% (0.3348% compared to 6.5465).

Acknowledgments

Author details

Dimitrios P. Spiridakos[1*], Nicholas C. Markatos[1,2] and Despoina Karadimou[1]

1 National Technical University of Athens, Athens, Greece

2 Texas A&M University at Qatar, Qatar

*Address all correspondence to: jamesspir92@gmail.com

IntechOpen

References

[1] Thompson J, Birk AM, Cunningham M. Design of infrared signature suppressor for the bell 205 (UH-1H) helicopters, part 1: Aerothermal design. In: Seventh CASI Propulsion Symposium. 1999

[2] Riley CJ, DeJarnette FR. An Engineering Aerodynamic Heating Method for Hypersonic Flow. American Institute of Aeronautics and Astronautics; 1992

[3] PHOENICS. VR Reference Guide: Documentation for Phoenics (TR 326), Version 2010. London, UK: CHAM; 2010

[4] Rooks S. Preliminary Investigations into the Use of PHOENICS for Evaluation of Aerodynamic Heating Phenomena. DRA Farnborough; 1996

[5] Murakami K, Yamamoto Y, Rouzand O. CFD Analysis of Aerodynamic Heating for HYFLEX High Enthalpy Flow Tests and Flight Conditions. 24th International Congress of the Aeronautical Sciences; 2004

[6] Jianwei L, Qiang W. Aircraft-skin infrared radiation characteristics modeling and analysis. Chinese Journal of Aeronautics; 2009

[7] Johansson M, Dalenbring M. Calculation of IR Signatures from Airborne Vehicles. FOI, Swedish Defence Research Agency; 2006

[8] Palharini RC, Santos WFN. Surface Temperature Effects on the Aerodynamic Surface Quantities of Hypersonic Cavity Flow, Combustion and Propulsion Laboratory (LCP). National Institute for Space Research (INPE); 2010

[9] Johnson KR, Rodriguez LJ. Technical Reference Guide for GTSIG/TCM2. Atlanta, GA: Georgia Tech Research Institute; 1990

[10] Galea ER, Markatos NC. The mathematical modeling and computer simulation of fire development in aircraft. International Journal of Heat and Mass Transfer. 1990;**34**:181-197

[11] Swanson BW, Solutions of the Three-Dimensional Navier-Stokes Equations in Non-orthogonal Coordinates to Calculate the Flow in a Long Spiral Impeller, ASME Paper 82-GT-268. 1982

[12] Launder BE, Spalding DB: The Numerical Computation of Turbulent Flows. 1973

[13] Thomas Markley J. Heat Transfer and Pressure Measurement on a 5-Inch Hemispherical Concave Nose at a Mach Number of 2.0. National Advisory Committee for Aeronautics; 1958

Edited by Konstantin Volkov

The accurate prediction of multi-physical and multi-scale physical/chemical/mechanical processes in engineering remains a challenging problem despite considerable work in this area and the acceptance of finite element analysis and computational fluid dynamics as design tools. This book intends to provide the reader with an overview of the latest developments in computational techniques used in various engineering disciplines. The book includes leading-edge scientific contributions of computational and applied mathematics, computer science and engineering focusing on the modelling and simulation of complex engineering systems and multi-physical/multi-scale engineering problems. The following topics are covered: numerical analysis and algorithms, software development, coupled analysis, multi-criteria optimization as they applied to all kinds of applied and emerging problems in energy systems, additive manufacturing, propulsion systems, and thermal engineering.

IntechOpen